Technische Universität München

TUM School of Natural Sciences

Beyond gyrokinetic theory-

Excitation of high-frequency turbulence in 6D Vlasov simulations of magnetized plasmas with steep temperature and density gradients

Mario Räth

Vollständiger Abdruck der von der TUM School of Natural Sciences der Technischen Universität München zur Erlangung des akademischen Grades eines

Doktors der Naturwissenschaften

genehmigten Dissertation.

Vorsitz: Prof. Dr. Lothar Oberauer

Prüfer der Dissertation:

1. Priv.-Doz. Dr. Klaus Hallatschek
2. Prof. Dr. Ulrich Stroth

Die Dissertation wurde am 31.03.2023 bei der Technischen Universität München eingereicht und durch die TUM School of Natural Sciences am 28.09.2023 angenommen.

Technische Universität München

Max Planck Institute for Plasma Physics

PhD Thesis

Beyond gyrokinetic theory

Excitation of high-frequency turbulence in 6D Vlasov simulations of magnetized plasmas with steep temperature and density gradients

Author
Mario Räth

Supervisors
PD Klaus Hallatschek
Prof. Katharina Kormann

November 17, 2023

Abstract

The Vlasov-Fokker-Planck-Maxwell system can describe physical phenomena in a tokamak plasma on all scales starting at large dynamics of the size of the device down to micro-scales of the order of the Larmor radius. However, up until recent years full 6D simulations were beyond the available computational capabilities. As an approximation, gyrokinetic transport simulations are in good agreement with experiments in the tokamak core regime, where only small perturbation amplitudes and gradients are present. Nonetheless, in regimes of high gradients and large turbulence fluctuation amplitudes, such as the plasma edge of a tokamak, the gyrokinetic approximation is debatable and at least those models based on a δf approximation break down completely.
On the other hand, experimental results from the PLT (Princeton Large Torus) tokamak at the Princeton Plasma Physics Laboratory (PPPL) have shown the suppression of fluctuations through the injection of high intensity ion Bernstein waves (IBWs) [Ono et al., 1988]. These studies focused on the empirical effect of externally excited IBWs, but do not explain the mechanisms. IBWs break the gyrokinetic approximation and therefore neither their intrinsic stability nor their influence on energy and particle transport can be studied by current gyrokinetic turbulence and stability codes. The capability to simulate the excitation of IBWs would be an important stepping stone toward a more comprehensive understanding of the high-frequency regime in the plasma edge.
We developed an optimized and scalable semi-Lagrangian solver for the 6D kinetic Vlasov system based on a highly efficient scheme to treat the $\boldsymbol{v} \times \boldsymbol{B}$ acceleration from the strong background magnetic field. This allows us to simulate the excitation of plasma waves and turbulence with frequencies beyond the cyclotron frequency without a limitation by the gradient strength or fluctuation level. [Raeth et al., 2023].
The code is well tested in the gyrokinetic regime. It shows excellent agreement with analytical dispersion relations for the ITG instability with deviations of $\sim 0.1\%$ for the growth rate and frequencies. For a further comparison, a comprehensive description for the composition of the energy fluxes in the 6D kinetic model is derived. The resulting contributions to the energy flux are reproduced correctly in the simulations. The turbulent transport in nonlinear ITG simulations is compared to turbulence simulations with the gyrokinetic code CGYRO [Candy et al., 2016].
The stability of IBWs is studied in a wide range of configurations. Several velocity space distributions, including the ring distributions in velocity space and the gyrokinetic distribution function caused by ITG simulations with local gradients are

shown to exhibit cyclotron instabilities. Furthermore, we developed a comprehensive understanding of the stability properties of the ion Bernstein waves and have been able to show their destabilization for steep temperature and density gradients. The growth rates can thereby exceed those of the ITG instability, especially when a density gradient is present. It is shown that the unstable IBWs produce a significant amount of transport in the linear as well as the nonlinear phase. The predicted instability is accurately reproduced by our simulation in a local gradient set-up as well as using a fully non-linear treatment of the gradients.

Zusammenfassung

Das Vlasov-Fokker-Planck-Maxwell-System ist in der Lage physikalische Phänomene in einem Tokamakplasma auf sämtliche größen Skalen zu beschreiben. Noch vor wenigen Jahren waren vollständige Simulationen des 6D kinteischen Models jenseits der verfügbaren Rechenkapazitäten. Als Näherung wurden gyrokintische Modelle verwendet, die nachweislich in der Lage sind, Transportprozesse im Plasmakern korrekt zu beschreiben. Notwendig für die Beschreibung ist die Annahme dass die Fluktuationsamplituden und die Gradieten in den simulierten Gebieten klein sind. In Regionen mit hohen Gradienten und großen Turbulenzschwankungsamplituden, wie z. B. am Plasmarand eines Tokamaks, ist die gyrokinetische Näherung fragwürdig und die auf einer δf-Näherung basieren brechen vollständig zusammen.
Ergebnisse aus dem dem Plasmaexperiment PLT (Princeton Large Torus) am Princeton Plasma Physics Laboratory (PPPL) zeigten, dass die durch die Injektion von hochintensiven Ionen Bernstein-Wellen (IBWs) die Fluktuationen im Plasmarand unterdrückt werden können [Ono et al., 1988]. Diese Studien konzentrierten sich auf den empirische Einfluss von extern angeregten IBWs, erklären aber nicht die intrinsischen Mechanismen. IBWs sind hochfrequente Welle, welche die gyrokinetische Näherung brechen und daher weder ihre intrinsische Stabilität noch ihr Einfluss auf den Energie- und Partikeltransport korrekt mit den derzeitigen gyrokinetischen Turbulenz- und Stabilitätscodes untersucht werden kann. Die Fähigkeit, die Anregung von IBWs zu simulieren, wäre ein wichtiger Schritt Schritt hin zu einem umfassenderen Verständnis der Relevanz von hochfrequenten Wellen im Plasmarand.
Wir haben einen optimierten und skalierbaren Semi-Lagrangeschen Löser für das 6D kinetisches Vlasov-System entwickelt. Die Besonderheit ist, dass der Code einen hocheffizienten Algorithmus verwendet um die Beschleunigung durch das starke Hintergrundmagnetfeld zu beschreiben. Dies ermöglicht es, Plasmawellen und Turbulenzen mit Frequenzen jenseits der Zyklotronfrequenz zu simulieren, ohne dass eine Begrenzung durch die Gradientenstärke oder das Fluktuationsniveau vorliegt. [Raeth et al., 2023].
Der Code ist im gyrokinetischen Regime gut getestet. Er zeigt eine ausgezeichnete Übereinstimmung mit der analytischen Dispersionsrelation für die ITG-Instabilität. Die Abweichungen liegen im Bereich von $\sim 0,1\%$ für die Wachstumsraten und die Frequenzen. Für einen weiteren Vergleich wird eine umfassende Beschreibung für die Zusammensetzung der Energieströme im 6D-kinetischen Modell abgeleitet. Die resultierenden Beiträge zum Energiestrom werden von dem Simulationscode korrekt reproduziert. Um den Transport in nichtlinearen ITG-Simulationen zu verifizieren,

wurde eine Vergleichsstudie mit den gyrokinetische Code CGYRO durchgeführt, wodurch das korrekte Verhalten des Codes bestätigt werden konnte.
Die zentralen Untersuchungen dieser Arbeit beschäftigen sich mit der Stabilität von IBWs in einem breiten Spektrum von Konfigurationen. Für diverse Geschwindigkeitsraumverteilungen, einschließlich einer Ringverteilungen im Geschwindigkeitsraum und die gyrokinetischen Verteilungsfunktion, welche durch ITG-Simulationen mit lokalen Gradienten verursacht wird, wird gezeigt, dass sie Ursprung der Zyklotroninstabiliytät sein können. Darüber hinaus haben wir ein umfassendes Verständnis für die Stabilitätseigenschaften der Ionen-Bernstein-Wellen geschaffen und konnten ihre Destabilisierung für steile Temperatur- und Dichtegradienten zeigen. Die Wachstumsraten der Zyklotroninstabilität können dabei die der ITG-Instabilität weit übersteigen, insbesondere wenn ein Dichtegradient vorhanden ist. Die analytisch abgeleitete Instabilität kann mit in unseren Simulationen sowohl mit lokalen Gradienten, als auch mit einer vollständig nichtlinearen Behandlung der Gradienten reproduziert werden.

Contents

List of Contributions

1. Mario Raeth, Klaus Hallatschek, and Katharina Kormann. Full-6d kinetic simulations of magnetically confined plasmas. *DPG Spring Meeting*, Poster, 2021

2. Mario Raeth, Klaus Hallatschek, Katharina Kormann, and Nils Schild. Excitation of high frequency waves in full-6d kinetic simulations of magnetically confined plasmas. *DPG Spring Meeting*, Presentation, 2022

3. Mario Raeth and Klaus Hallatschek. Surprisingly tight courant-friedrichs-lewy condition in explicit high-order arakawa schemes. *Journal of Scientific Computing*, [Submitted]

4. M. Raeth, K. Hallatschek, and K. Kormann. Slab itg simulated with 6d fully kinetic semi-lagrangian code. *Physics of Plasmas*, [Manuscript in preparation], 2023

5. Mario Raeth and Klaus Hallatschek. High frequency non-gyrokinetic turbulence at tokamak edge parameters. *Phys. Rev. Lett.*, [submitted, arXiv:2310.15981], 2023

6. Nils Schild, Mario Räth, Sebastian Eibl, Klaus Hallatschek, and Katharina Kormann. A performance portable implementation of the semi-lagrangian algorithm in six dimensions. *Computer Physics Communications*, 295:108973, 2024

7. Mario Raeth, Klaus Hallatschek, and Katharina Kormann. Excitation of high frequency waves in nonlinear fully kinetic vlasov simulation. *EPS 2023 - Bordeaux*, [Abstract submitted]

List of Figures

Glossary

$\boldsymbol{r}$	-	configuration space coordinate
$\boldsymbol{k}$	-	wave vector
$\boldsymbol{v}$	-	velocity space coordinate
$\hat{\boldsymbol{x}}, \hat{\boldsymbol{y}}, \hat{\boldsymbol{z}}$	-	unit vectors in configuration space
$\hat{\boldsymbol{v}}_x, \hat{\boldsymbol{v}}_y, \hat{\boldsymbol{v}}_z$	-	unit vectors in velocity space
$f(\boldsymbol{r}, \boldsymbol{v})$	-	distribution function
n	-	particle density
ρ	-	charge density
$\boldsymbol{u}$	-	particle flux density
$\boldsymbol{Q}$	-	energy flux density
$\boldsymbol{\Pi}$	-	stress tensor density
$n_k,\ f_k,\ \epsilon_k$	-	Fourier mode of respective quantity
$\delta n,\ \delta f,\ \delta\epsilon$	-	perturbation of respective quantity
T	-	temperature
t	-	time
ω	-	frequency
ω_c	-	cyclotron frequency
ϕ	-	electrostatic potential
$\boldsymbol{E}$	-	electric field
$\boldsymbol{B}$	-	magnetic field
$\boldsymbol{B}_0$	-	strong background magnetic field
$\boldsymbol{\rho}$	-	Larmor radius vector
$\boldsymbol{R} = \boldsymbol{r} - \boldsymbol{\rho}$	-	gyro-center coordinate
$v_\perp$	-	perpendicular velocity coordinate
v_z	-	parallel velocity coordinate
α	-	velocity angle coordinate
$g(\boldsymbol{R}, \boldsymbol{v})$	-	distribution function in gyro-center coordinates
$g_m(\boldsymbol{R}, v_\perp, v_z)$	-	Fourier component of distribution function in α
$J_p(x)$	-	Bessel function of first kind
$I_p(x)$	-	modified Bessel function of first kind

Chapter 1

Introduction

1.1 Nuclear fusion

Nuclear fusion is the process of combining nuclei of lighter atoms to form a heavier nucleus. It is the opposite process of fission, where a heavy nucleus is split into lighter parts. A nucleus consists of individual protons and neutrons, however, the weight of the nucleus is less than the sum of the individual neutrons and protons. The energy equivalent of this mass ($E = mc^2$) is contained in the fields that keep the nucleus together and is called the binding energy. When two light cores are combined and the resulting product is than the sum of its parts and the energy is released in form of the kinetic energy of the products. For light nuclei, it is usually the case that the binding energy of the fused product is lower than the combined binding energy of the starting pieces and energy can be gained from the fusion process. This is the basis of nuclear fusion. For heavier nuclei, the binding energy per nucleon increases when the nucleus is split, which is the reason, why we can gain energy through nuclear fusion and fission. We displayed the binding energy per nucleon in MeV as a function of the number of nucleons in the nucleus in figure 1.1. If the products of our reaction, fission or fusion, lie higher on this graph than the educts, energy can be gained from the process. For example, in typical fission reactors U^{235} is split. The reaction considered for most nuclear fusion devices is the fusion of Deuterium H^2 and a Tritium H^3 nucleus to form helium He^4 [Wesson and Campbell, 2011]

$$\mathrm{H}_1^2 \ + \ \mathrm{H}_1^3 \ \rightarrow \ \mathrm{He}_2^4 \, (3.5\mathrm{MeV}) \ + \ n_0^1 \, (14.1\mathrm{MeV}), \tag{1.1.1}$$

which releases a total of 17.6MeV of fusion energy. This reaction is usually favored over other reactions such as Deuterium - Deuterium (D-D) or Deuterium - Helium (D-He) fusion because its cross-section is significantly larger and the maximum of the cross-section lies at lower temperatures.
Overcoming the Coulomb barrier of the repelling charges of the nuclei is still not an easy task and extreme conditions are necessary to achieve the ignition of the plasma, which means that the heating of the plasma is dominated by the fusion reaction and

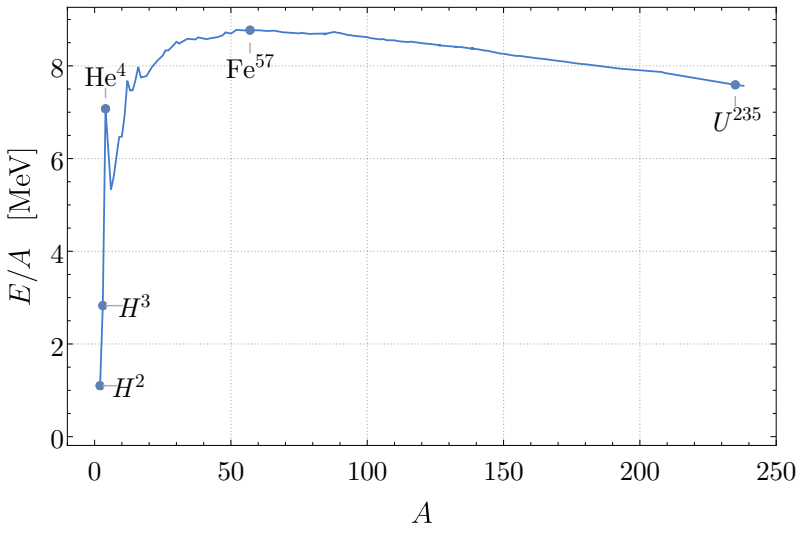

Figure 1.1: Binding energy per nucleon as a function of the number of nucleons [Ghahramany et al., 2011]

not external heating sources. The conditions necessary for ignition are commonly summarized in the Lawson criterion [Lawson, 1957]

$$n\tau_E T > 5 \times 10^{21} \frac{\mathrm{s\,keV}}{\mathrm{m}^3}, \tag{1.1.2}$$

which states that the triple product out of the density n, the temperature T and the time the energy is confined in the system τ_E has to surpass a certain threshold. Most devices considered for fusion energy production fall into one of two categories, magnetic confinement fusion or inertial fusion. While inertial fusion uses very high pressures (often by the application of lasers) to achieve high densities, magnetic confinement fusion tries to achieve extremely high temperatures. The most common device type for magnetically confined fusion is the tokamak.

1.2 Tokamak & edge physics

In its simplified form, a tokamak consists of a torus-shaped magnetic field, that is used to confine the plasma. In the most trivial configuration, a toroidal magnetic field B_ϑ (compare figure 1.2) induced by poloidal coils confines the plasma. However, this configuration is not stable, as the particles can drift up and down out of the confinement. To prevent this from occurring, a secondary poloidal magnetic field B_φ is used. To generate the poloidal magnetic field, a current is induced by induction from a transformer coil residing in the center of the torus. An important quantity in describing the magnetic field of a tokamak is the ratio between the poloidal and toroidal magnetic field, called the safety factor $q = \frac{rB_\vartheta}{RB_\varphi}$, where r and R are the minor and major radius of the torus respectively. In figure 1.3, two example

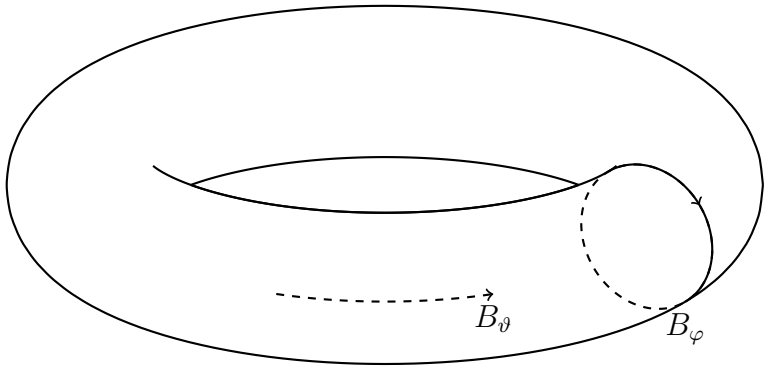

Figure 1.2: Illustration of the toroidal B_ϑ and poloidal B_φ magnetic field components in a torus configuration

configurations for a magnetic field are displayed. In figure (a), the case of a purely toroidal magnetic field ($q = \infty$) is shown. The second illustration shows an example of a magnetic field configuration with a finite safety factor ($q = 2$).

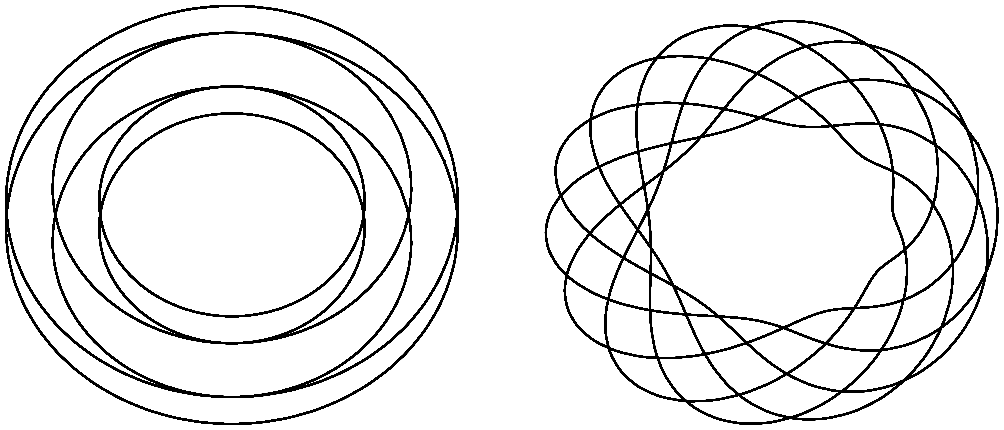

(a) $q = \infty$ (b) $q = 2$

Figure 1.3: Illustration of two magnetic field configurations of a idealized tokamak for two different safety factors $q = \infty$(a) and $q = 2$(b)

The various combinations of magnetic field configurations, combined with different heating methods generate a vast space of parameters in which a fusion experiment can be performed. Finding an optimal operational mode which maximized the triple product in a stable plasma is one of the main challenges in nuclear fusion and reactor research. In 1982, a new operational mode was found in the tokamak ASDEX [Wagner et al., 1982]. The H(high confinement)-mode achieves, compared to the L(low confinement)-mode, significantly better energy confinement which is mainly attributed to a lower electron heat diffusivity and particle diffusion coefficient [Wagner et al., 1982]. In the transition from the L-mode, a transport barrier is formed at the edge of the plasma. The transport barrier causes a steepening of the

gradients, resulting in the typical temperature and density profile of the H-mode, which has a high pedestal and steep gradients.
The steep gradient region of the H-mode has been the subject of research for the past 30 years, starting with fluid transport simulations in the 1990s [Zeiler et al., 1998]. Later it was realized that the consideration of gyroorbit effects was necessary, thus, gyrofluid [Scott, 2006] and gyrokinetic models [Told et al., 2008] were used. However, it has not been possible to develop a comprehensive understanding of the formation of the transport barrier in the transition from L to H-mode. Microturbulence is considered to be the major driver for anomalous transport in the plasma edge. Many known instabilities such as ion temperature gradient (ITG) modes, trapped electron modes (TEM), and kink ballooning modes (KBMs) are known to drive microturbulence in fusion plasma. Until today, gyrokinetic simulations are the best approach to simulate these instabilities. However, the question has to be raised, whether these models are suitable for the task. Some fundamental assumptions underlying the derivation of gyrokinetic theory, such as low gradients and small fluctuation levels, are not met in the plasma edge. A more complete overview of the models used is given in section 1.3.
In the search for an explanation for the higher confinement in the H-mode, it was found that the transition between the modes is linked to an increase in radial electric fields in the edge causing shear flows (due to $\boldsymbol{E} \times \boldsymbol{B}$-drift). Shear flows are known to reduce fluctuation levels [Burrell et al., 1995]. Experimental results from the PLT (Princeton Large Torus) tokamak at the Princeton Plasma Physics Laboratory (PPPL) showing the suppression of fluctuation levels through the injection of high energy ion Bernstein waves (IBWs) [Ono et al., 1988]. Following these results, theoretical studies were conducted, showing the increase in shear flow when IBWs are externally excited in the plasma edge [Craddock et al., 1994]. While these studies focus on the effect of externally excited IBWs, the effect of internally excited waves on the plasma behavior is not well known. A simulation code that is capable of simulating the excitation of IBWs and their influence on energy and particle transport is an important tool in understanding the role of high-frequency waves in the L/H-mode transition. This work should be the stepping stone toward a comprehensive understanding of the high-frequency regime in the plasma edge.

1.3 Plasma modeling

All issues mentioned in section 1.2 can be approached experimentally and theoretically. While on the experiment side, complicated machines are built and tested in different configurations, the theory focuses on understanding the plasma dynamic with various models. Already from the small overview in section 1.2 shows that issues arise on a large range of different temporal or spacial scales. The models to describe a plasma vary greatly in complexity and computational costs. While some analytical models exist, especially in linear stability analysis, most systems are too complex to be analyzed analytically. Often an analytical model is used to verify the

results of numerical computations. The most trivial, but also the most complete model to describe a plasma involves modeling the trajectory of each particle individually. This would not only include solving an equation of motion of each particle but also computing the field interaction of all combinations of particles. Considering that a fusion plasma contains $\sim 10^{19}$ particles [Mlynek et al., 2011] per cubic meter which makes simulations on any relevant scale unfeasible even on the biggest supercomputers. To obtain a computationally more manageable description of the plasma, a whole range models have been derived over the years, that can describe a plasma on a vast range of scales. The models used in magnetically confined fusion research usually fall into one of two categories. They either belong to the group of fluid models or kinetic models.

Fluid models, such as magnetohydrodynamics [Biskamp, 1997] (ideal or resistive), two-fluid models, or the Braginski transport model [Braginskii, 1965], can describe a plasma at the scale of a fusion device, which is beautifully illustrated in the simulation of edge localized modes [Cathey et al., 2021] and plasma disruption events [Bandaru et al., 2019]. In a fluid model, it is assumed that the plasma is always in thermal equilibrium, which means that the velocity distribution resembles a Maxwell-Boltzmann distribution. This assumption makes calculations computationally less demanding, as it is not necessary to resolve the velocity space. However, a lot of physical effects are not present in these models (e.g. Landau damping [Landau, 1936]).

For a more comprehensive description of plasma, kinetic models are used. In kinetic models, the plasma is described by a phase space density f, and the dynamic is given by the kinetic equation (Vlasov or Fokker-Planck equation). The particles generate and interact with electromagnetic fields, which depend on the distribution function in a self-consistent manner (Maxwell's equations). Solving the full kinetic equation of motion requires solving a six-dimensional partial differential equation which is linked to a significant computational cost. To contain the computational cost while still having some benefits of kinetic simulations, several reduced models such as drift kinetics [Littlejohn, 1981] and gyrokinetics [Sugama and Horton, 1998] were derived. These theories use certain assumptions, such as an infinitely high Larmor frequency or small gradients to reduce the equations effectively to a four-dimensional phase space. Especially the frequency assumption reduces the computational cost immensely as the whole theory assumes a low-frequency limit $\omega \ll \omega_{\mathrm{ci}}$ and high frequencies like the Larmor frequency ω_c do not need to be resolved. This allows the use of significantly larger time steps. While these reduced kinetic descriptions are well established for simulations in the core of fusion devices (with codes like GS2 [Kotschenreuther et al., 1995] and GENE [Jenko, 2000]), problems arise when going to the edge of the plasma in a fusion device. In the plasma edge, the gradients can get so steep and the fluctuation level so high that fundamental assumptions that go into the derivation of these theories are broken. Efforts are made to implement gyrokinetic models to simulate the plasma edge [Michels et al., 2022]. However, their validity still has to be shown, especially in conditions of very steep gradients. In the H-mode, the typical gradient lengths can become as short as a single ion

Larmor radius ρ_L and a reduced treatment of the gyroorbit of the particles is no longer possible, and a more general model for the description of the plasma might be needed.
In recent years, some efforts have been made in developing simulations tools that go beyond the complexity of the currently established kinetic models, like the cyclo-kinetic model [Deng et al., 2016] and fully kinetic ion models [Sturdevant et al., 2016]. However, most of the models are still based on some assumption. The goal of this work is the development of a fully kinetic six dimensional Vlasov code that can be used to simulate a plasma in regimes far outside the region of applicability of gyrokinetic theory. Such a tool can provide important insights in physical mechanisms in the plasma edge as it is not limited to small gradients or low fluctuation levels.

1.4 Outline

This work is structured in the following. Chapter 2 provides a brief introduction into the main theoretical background necessary for the understanding of the results presented in this work and an overview of the numerical methods used in the implementation of our fully-kinetic Vlasov code. The major results are structured in three chapters. In chapter 3, a verification of our code in the gyrokinetic regime is shown by comparing simulation results to analytical considerations and non-linear gyrokinetic simulations. Furthermore, a description of the perpendicular energy fluxes is presented, which is more extensive than the understanding form gyrokinetic theory. In the second result chapter (chapter 4), the stability of ion Bernstein waves is explored. It has been possible to showcase various driving conditions for the cyclotron instability, such as velocity distributions and spatial gradients. The instabilities are investigated analytically and numerically with our kinetic code BSL6D. For a more realistic scenario, the code is extended to an nonlinear treatment of the temperature and density gradient. The numerical results for the ITG and the cyclotron instability are shown in chapter 5.

Note: All quantities in this work past section 2.2 are normalized according to appendix A, if not stated otherwise.

Chapter 2

Theoretical background

2.1 Plasma properties

2.1.1 What is a plasma?

A plasma is commonly described as the 4th state of matter after solid, liquid and gas and resides at the high temperature end of this series. When a gas is heated further, the temperature becomes large enough that the thermal energy is larger than the ionization energy of the atoms. However, the ionization is not a sudden process. With increasing temperature more and more atoms get ionized. A certain amount of particle is always ionized in every gas, even at room temperature. In the example of a hydrogen gas, with an ionization energy of 13.6eV, the ionization occurs on a range between 10000K and 20000K [Saha, 1921]. However, not every ionized gas can be called a plasma. A widely used definition is:
"A plasma is a quasi-neutral gas of charged and neutral particles which exhibits collective behavior" [Chen, 1984]
The two defining properties here are quasi-neutrality and collective behavior, which are defined as follows:

Quasi-neutrality A key property of a plasma is the ability to effectively shield electric charges. Imagine, an electric charge is introduced into a plasma. The charge would attract the surrounding particles of the opposite charge and repel particles of the same charge creating a new equilibrium in the plasma which induces an electric field directly canceling the induced field. As the particles in the plasma have a finite non-zero thermal energy the electric field is not shielded perfectly, however, a layer around the charge is created in which the electric field is suppressed. It can be shown that the electric field decays exponentially with the distance from the induced charge

$$\phi = \phi_0 e^{-\frac{-|\boldsymbol{r}|}{\lambda_D}}, \tag{2.1.1}$$

where the Debye length $\lambda_D = \sqrt{\frac{\epsilon_0 T}{ne^2}}$ is the characteristic length [Debye and Hückel, 1923]. The shielding characteristics of the plasma depends on its temperature T and its density n. The higher the temperature, the higher is the mobility of the particles and their motion is less influenced by the induced charge leading to a worse shielding. In contrast, a higher density increases the shielding properties as more particles can shield the electric field more effectively. Quasi-neutrality is defined, system size L must be much larger than the Debye length.

Collective behavior The collective behavior is best understood when comparing a plasma to a neutral gas. In a gas, the particles are neutral and thus do not experience any net electromagnetic forces except very sort range Van der Waals interactions. A particle in a gas moves freely until it collides with another particle, in a pair wise interaction. The collision interaction determines the motion of the particle (i.e. Brownian motion [Einstein et al., 1915]). Furthermore, external forces that act on a gas, such as the vibrations induced by the human vocal organs or the recoil of a jet engine are transmitted through the medium by individual collisions of particles. In a plasma, the charged particle generate local concentrations of positive and negative charges. The resulting electric fields influence the motion of other particles in a region much larger than the local concentration. Relative motion between positively and negatively charged particles can lead to currents, which induce a magnetic field. Magnetic field also penetrate far into the medium and influence particles at large distances. The ratio between the influence of concessional interaction between particles and the effect of the self-constant electromagnetic fields can be seen as a comparison of time scales. The particle wave interaction leads to plasma oscillations with a frequency ω. Comparing this frequency to the mean time between to collisions τ gives an estimate for the importance of collisions. The limit $\omega\tau \to \infty$ is called a collision-less plasma. Most plasma studies in fusion devices, as well as all considerations in this work, are within the limit of a collisionless plasma. In a more general model, when the mean time between collisions is considered to be finite (e.g. in concessional gyrokinetics [Candy et al., 2016]), models for the interaction between charged particles has to be found (e.g. Landau collision operator [Landau, 1936] or Sugama collision operator [Sugama and Horton, 1998] for kinetic plasma models).

In summary, for a medium to be considered a plasma three main conditions need to be met. Firstly, the system size L needs to be larger than the Debye length λ_D

$$\lambda_D \gg L. \tag{2.1.2}$$

The number of particles within the Debye sphere $N_D = \frac{4}{3} n\pi\lambda_D^3$ needs to be large

$$N_D \gg 1, \tag{2.1.3}$$

and the collision frequency ν_C (the inverse mean time between collisions) has to be

smaller than the typical frequency of plasma oscillations ω in the system

$$\nu_{\mathrm{C}} \ll \omega. \tag{2.1.4}$$

2.1.2 Guiding center motion

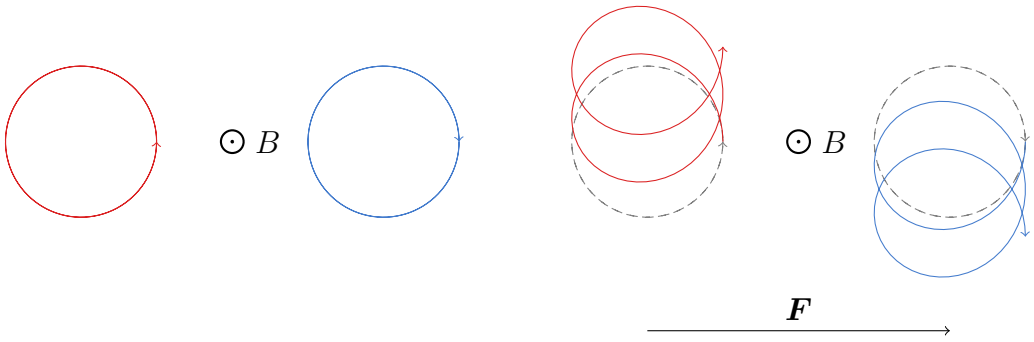

(a) (b)

Figure 2.1: Visualization of gyromotion of charged particles in a magnetic field (a) and the drift induced by a perpendicular force (b)

Guiding center drifts If a magnetic field $\boldsymbol{B}$ is present, charged particles cannot move freely perpendicular to the magnetic field, but are forced on a circular orbit around the magnetic field lines, due to the Lorentz force $\boldsymbol{F}_L = q\boldsymbol{v} \times \boldsymbol{B}$. The radius of the gyromotion is the Larmor radius $\varrho = \frac{m}{qB^2}|\boldsymbol{B} \times \boldsymbol{v}|$ and depends on the velocity of the particle perpendicular to the magnetic field $v_\perp$. If a force acts on the particle perpendicular to the magnetic field (w.l.o.g. $\boldsymbol{B} = B\hat{\boldsymbol{z}}, \boldsymbol{F} = F\hat{\boldsymbol{x}}$) the equations of motion look as followed

$$\dot{v}_x = \frac{qB}{m} v_y + \frac{F}{m}, \tag{2.1.5}$$

$$\dot{v}_y = \frac{qB}{m} v_x. \tag{2.1.6}$$

The solution to the system of differential equations is solved for the velocities, reveals that the particle has an additional velocity in y-direction, $v_y = -v_\perp \sin\frac{qB}{m}t + \frac{F}{qB}$. By averaging over the gyromotion and generalizing it for an arbitrary force $\boldsymbol{F}$ the expression for the drift velocity is reached

$$\boldsymbol{v}_D = \frac{\boldsymbol{F} \times \boldsymbol{B}}{qB^2}. \tag{2.1.7}$$

When the particle moves parallel to the acting force, it is accelerated and the radius of gyration increases and when it is moving in the opposite direction of the acting

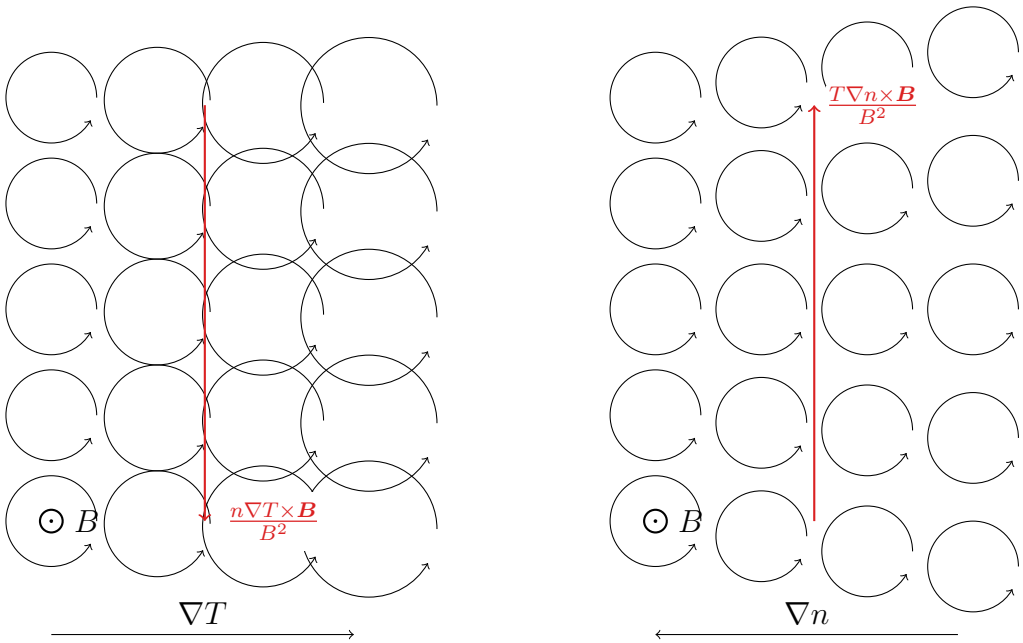

(a) (b)

Figure 2.2: Visualization of the adiabatic drift. A temperature gradient (a) and density gradient (b) leads to a perpendicular net flow

force, it is decelerated, and the radius becomes smaller. The alternating change in radius leads to a drifting motion of the particle perpendicular to the force (compare figure 2.1(b)).

Diamagnetic drifts If instead of the single particle motion, an equilibrium distribution of particles with a stationary velocity field $\boldsymbol{u}$ in a magnetic field with a pressure gradient is considered

$$qn(\boldsymbol{E} + \boldsymbol{u} \times \boldsymbol{B}) - \nabla p = 0, \tag{2.1.8}$$

the flow component $\boldsymbol{u}_\perp$ perpendicular to the magnetic field $\boldsymbol{B}$ can be calculated by computing the vector product in equation (2.1.8) with $\boldsymbol{B}$. After the vector identity $(\boldsymbol{u} \times \boldsymbol{B}) \times \boldsymbol{B} = -B^2\boldsymbol{u} + (\boldsymbol{B} \cdot \boldsymbol{u})\boldsymbol{B} = -B^2\boldsymbol{u}_\perp$ is applied, we obtain [Stroth, 2011]

$$\boldsymbol{u}_\perp = \frac{\boldsymbol{E} \times \boldsymbol{B}}{B^2} - \frac{\nabla p \times \boldsymbol{B}}{nqB^2}. \tag{2.1.9}$$

The first term describes the guiding center drift induced by an electric field $\boldsymbol{E}$. It can be noted that the $\boldsymbol{E}\times\boldsymbol{B}$-Drift is in the same direction for all species, because the electric force $\boldsymbol{F} = q\boldsymbol{E}$ acts in opposite directions for electrons and ions. The second term is the *diamagnetic drift*. If the pressure is given by the ideal gas law [Krönig, 1856], the pressure gradient can be written as $\nabla p = n\nabla T + T\nabla n$. If we assume

(w.o.l.g) a pressure gradient in x-direction a particle flow in y-direction is induced. This particle flux can not be attributed to the movement of individual particles. It is a collective behavior that arises, when the particle motion is integrated over a certain volume. In the example of a density gradient (compare figure 2.2(b)), at any point in space, more particles have a velocity up. In case of the temperature gradient (compare figure 2.2(a)) the particles with direction in the downward direction have a higher velocity. Both cases lead to a net flow $\boldsymbol{u}^{\text{dia}}$ perpendicular to the magnetic field and the pressure gradient
Furthermore it can be shown, that a temperature gradient also induces a perpendicular heat flux. When a small volume element in figure 2.2 is considered, the particles that flow upwards are on average hotter than the particles flowing downwards which leads to a *diamagnetic heat flux* [Chen, 1984]

$$\boldsymbol{q}^{\text{dia}} = \frac{5}{2}\frac{nT}{qB^2}(\nabla T) \times B. \tag{2.1.10}$$

2.1.3 Drift waves

Inhomogeneities can induce various dynamics in the plasma, e.g. wave propagation and induction of instabilities. This will be illustrated with the example of how a density gradient enables a wave to propagate perpendicular to the magnetic field. Let us assume the situation displayed in figure 2.3(a). It shows a potential perturbation $\tilde{\phi}$ in the presence of a magnetic field $\boldsymbol{B}$ (pointing out of the drawing plane) and a density gradient ∇n(pointing up). Furthermore, adiabatic electrons are assumed, such that the potential is perfectly in phase with the density perturbation.
The electric potential and the resulting electric field $\boldsymbol{E}$ induce a drift motion $u^{\boldsymbol{E}\times\boldsymbol{B}}$ in the particles. As demonstrated in by the vectors, the particles drift opposite to the direction of the gradient for an electric field pointing in a positive direction (left) and in the direction of the gradient for the opposite case (right). The density gradient ∇n illustrated by the vector on the left shows that the density increases from the bottom to the top. The difference in density leads to an increase in density at the position of the "downward" flow and a decrease in density in the "upward" direction. The change in density causes the electric potential to change analogously inducing a propagation of the perturbation to the right. The propagation direction is parallel to the diamagnetic drift direction $\boldsymbol{u}_{\text{dia}} = -\frac{\nabla p \times \boldsymbol{B}}{nqB^2}$.
If the wave vector of the perturbation is not perpendicular to the magnetic field, the wave additionally propagates in the direction of the magnetic field. This is illustrated in figure 2.3(b). The plot shows the same wave whereas here, the magnetic field $\boldsymbol{B}$ points upwards, and the density gradient ∇n points into the drawing plane. In the lower half, the wave vector is illustrated with its parallel and perpendicular components. Usually in magnetized plasma, the parallel component is much smaller compared to the perpendicular component $k_z \ll k_\perp$. The wave has a perpendicular phase space component $u^z_{\text{drift}} = \omega/k_z$. If a particle, illustrated by the blue dot, has the velocity $v_z = \omega/k_z$, it travels in sync with the wave in the direction of the magnetic field and can interact resonantly with the wave, which can lead to a desta-

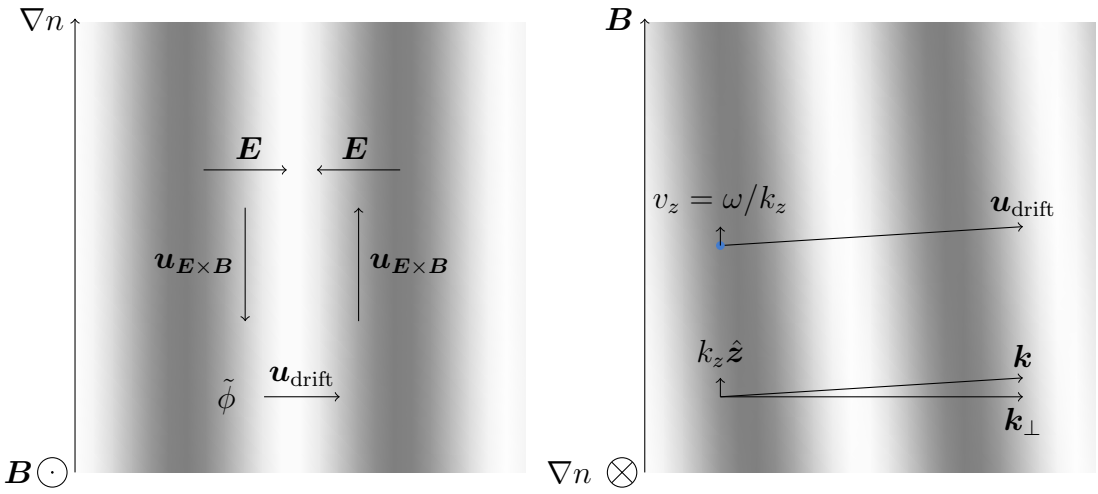

Figure 2.3: Illustration of propagation mechanism for drift wave appendix

bilization of the plasma wave. The particle population with the parallel velocity $v_z = \omega/k_z$ experiences a constant $\boldsymbol{E} \times \boldsymbol{B}$-drift from the electric field caused by the perturbation which can lead to a reinforcement of the perturbation, which in turn feeds back to the resonant particles, and thus, leading to an exponentially growing perturbation.

2.2 Kinetic description of a plasma

From here on, if not stated otherwise, all quantities are normalized according to A.

In kinetic theory, the plasma is described by the distribution function $f(t, \boldsymbol{r}, \boldsymbol{v})$ which is a function of the position $\boldsymbol{r}$ and the velocity $\boldsymbol{v}$. In case of a non-steady state system, the distribution function also depends on the time t. When $\mathrm{d}^3r\mathrm{d}^3v$ is an infinitesimal volume element of the phase space, then $f\mathrm{d}^3r\mathrm{d}^3v$ gives the number of particles at a given time t, at position $\boldsymbol{r}$ and with velocity $\boldsymbol{v}$. From the distribution function $f(t, \boldsymbol{r}, \boldsymbol{v})$, all relevant macroscopic quantities necessary for the description as of a plasma can be derived. The macroscopic velocity field is given by the 0th moment of the distribution function

$$n(t, \boldsymbol{r}) = \int f(t, \boldsymbol{r}, \boldsymbol{v})\mathrm{d}^3v. \tag{2.2.1}$$

The total number of particles contained in a volume V are thus $N = \int_V \int f\mathrm{d}^3v\mathrm{d}^3r$. The particle flux density $\boldsymbol{u}(\boldsymbol{r}, t)$ can be computed by the first moment

$$n(\boldsymbol{r}, t)\boldsymbol{u}(t, \boldsymbol{r}) = \int \boldsymbol{v} f(t, \boldsymbol{r}, \boldsymbol{v})\mathrm{d}^3v, \tag{2.2.2}$$

and the kinetic energy density $\epsilon(t, \boldsymbol{r})$ is given by

$$\epsilon(t, \boldsymbol{r}) = \int \frac{v^2}{2} f(t, \boldsymbol{r}, \boldsymbol{v}) \mathrm{d}^3 v. \tag{2.2.3}$$

Further macroscopic quantities, such as the heat flux and the Cauchy stress tensor can be computed from higher moments.

Kinetic equation In case the individual interaction between particles is negligible, the distribution function has to obey Liouville's theorem, which states that the distribution function is constant along trajectories in phase space [Landau and Lifshitz, 1980], according to which

$$\frac{\mathrm{d}f}{\mathrm{d}t} = 0, \tag{2.2.4}$$

where $\frac{\mathrm{d}}{\mathrm{d}t}$ is the total derivative along the phase space trajectory of a particle, given by its equation of motion. Under the presence of a force $\boldsymbol{F}$, the trajectory of a particle is described by

$$\frac{\partial \boldsymbol{r}}{\partial t} = \boldsymbol{v}, \qquad \frac{\partial \boldsymbol{v}}{\partial t} = \frac{\boldsymbol{F}}{m}. \tag{2.2.5}$$

Thus, the time evolution of the distribution function is given by the kinetic equation

$$\frac{\mathrm{d}f}{\mathrm{d}t} = \frac{\partial f}{\partial t} + \boldsymbol{v} \cdot \nabla f + \boldsymbol{F} \cdot \nabla_{\boldsymbol{v}} = 0, \tag{2.2.6}$$

where $\nabla = (\partial_x, \partial_y, \partial_z)$ and $\nabla_{\boldsymbol{v}} = (\partial_{v_x}, \partial_{v_y}, \partial_{v_z})$ are the gradient operators on the configuration and velocity space. In case of collisions, the distribution function is not constant anymore along particle trajectories, and instead of eq. (2.2.4) reads

$$\frac{\mathrm{d}f}{\mathrm{d}t} = C(f), \tag{2.2.7}$$

where $C(f)$ is called the collision operator and describes the rate of change of the distribution function along a trajectory.

Collisionless plasma Coulomb forces decrease slowly ($F_C \propto \frac{1}{r^2}$), compared to gasses, where interaction between individual particles are usually very short ranged. While collision in a gas of neutral particles can mostly be neglected and the gas is considered ideal, the condition in a plasma is stricter. A plasma with charge q and a mean distance between particle $\bar{r}t$ weakly interacting, if the energy in the coulomb interactions $q\phi = \frac{q^2}{4\pi\epsilon_0 \bar{r}}$ is much smaller than the kinetic energy of the particles ϵ. Furthermore, the collision can be completely neglected, when the collision time τ (mean time between collisions) is larger that the time scales of interest. In the

context of fusion physics, these conditions are usually assumed in the hot cores of fusion devices, where temperature of the order of $T \sim T^{-\frac{3}{2}}$ are possible [NRL, 2018]. In regions closer to the edge of a fusion plasma, the temperature drops and these criteria is not necessarily met anymore.

Properties of the Vlasov equation The Vlasov equation describes the special case of the transport equation in equation 2.2.6, in which the accelerating force acting on the particles is a result of the Lorentz force generated by plasma in a self-consistent manner. Thus, the Vlasov equation for a collision-less plasma is

$$\frac{\partial f}{\partial t} + \boldsymbol{v} \cdot \nabla f + \frac{q}{m}(\boldsymbol{E}(\boldsymbol{r}) + \boldsymbol{v} \times \boldsymbol{B}) \cdot \nabla_{\boldsymbol{v}} f = 0. \tag{2.2.8}$$

The electric field $\boldsymbol{E}$ and $\boldsymbol{B}$ and their connection to the macroscopic quantities of the plasma are given in the most general case by Maxwell's equations. q and m describe the charge and the mass of the particles respectively. If multi species models are described, often a index s is introduce ($m_s,\ q_s,\ f_s$).
The formal connection between the Vlasov equation and Liouville's theorem gives some very potent properties. The distribution function f is constant along the trajectories of a individual particles. These trajectories, or so-called characteristics, are determined by the set or ordinary differential equations from eq. (2.2.5), when introducing again the Lorenz force, the characteristic are often denoted with capital letters for easier distinguishing from the phase space coordinates

$$\frac{\partial \boldsymbol{R}}{\partial t} = \boldsymbol{V}, \qquad \frac{\partial \boldsymbol{V}}{\partial t} = \frac{q}{m}\left(\boldsymbol{E} + \boldsymbol{V} \times \boldsymbol{B}\right). \tag{2.2.9}$$

The distribution function is constant along the solution ($\boldsymbol{R}(t, \boldsymbol{r}, \boldsymbol{v})$, $\boldsymbol{V}(t, \boldsymbol{r}, \boldsymbol{v})$) of the set of equations in 2.2.9, with $\boldsymbol{R}(0, \boldsymbol{r}, \boldsymbol{v}) = \boldsymbol{r}$ and $\boldsymbol{V}(t, \boldsymbol{r}, \boldsymbol{v}) = \boldsymbol{v}$, the time evolution of the distribution function is given by

$$f(\boldsymbol{r}, \boldsymbol{v}, t) = f(\boldsymbol{R}(t, \boldsymbol{r}, \boldsymbol{v}), \boldsymbol{V}(t, \boldsymbol{r}, \boldsymbol{v}), 0). \tag{2.2.10}$$

The numerical scheme to solve the Vlasov equation, which is decried in section 2.6 is based on the characteristics.

2.3 Analytical description of wave particle interactions

2.3.1 Waves in a unmagnetized plasma

When the Vlasov equation is combined with Maxwell's equations, it can describe all interactions of the particles within the plasma and electromagnetic fields. The description in this section follows the book "The Framework of Plasma Physics" [Hazeltine and Waelbroeck, 2018].

To get a first understanding, the system is reduced to a purely electrostatic plasma with no magnetic field in a 1D1V setup. Section 2.3.3 extents the system to the full 3D3V phase space. Furthermore, the plasma consists of a homogeneous background $f_0(v)$ and a plane wave perturbation

$$f(x,v) = f_0(v) + f_k(v,t)e^{ikx}, \tag{2.3.1}$$

where $f(v,t)$ is the time dependent amplitude of our plane wave. The linearized Vlasov equation can the be written in Fourier transformed form (writing the electric field in terms of the electrostatic potential $E_k = -ik\phi_k$)

$$\frac{\partial f_k(v,t)}{\partial t} + ikvf_k(v,t) = -ik\phi_k(t)\frac{\partial f_0(v)}{\partial v}. \tag{2.3.2}$$

For a self-consistent description of the system, the equation of motion is combined with an equation for the electric potential. For the purpose of demonstration, the Poisson equation $\Delta\phi = 1 - \int f \mathrm{d}v$ ($\epsilon_0 = 1$) is used, which also can be written in Fourier form

$$-k^2\phi_k = \int f_k(v,t)\mathrm{d}v. \tag{2.3.3}$$

In order to obtain the time evolution of the distribution function, the Laplace transformation (using the definition from [Hazeltine and Waelbroeck, 2018]) is applied to the Vlasov equation (2.3.2)

$$F_k(v,\omega) = \int_0^\infty e^{i\omega t} f_k(v,t)\mathrm{d}t, \tag{2.3.4}$$

where $\omega \in \mathbb{C}$ is the complex frequency. The transformation is applied to every term in the Vlasov equation 2.3.2 and the following system of equations is obtained

$$(\omega - kv)F_k(v,\omega) = if_k(u,0) - ik\phi_k(\omega)\frac{\partial f_0(v)}{\partial v}, \tag{2.3.5}$$

$$-k^2\phi_k(\omega) = \int F_k(v,\omega)\mathrm{d}v. \tag{2.3.6}$$

An expression for the potential is derived by solving eq. (2.3.5) for the the distribution function and inserting it to the Poisson equation (2.3.6), resulting in the expression

$$\begin{aligned}\phi_k(\omega) &= -\frac{1}{k^2}\int\left[\frac{if_k(u,0)}{\omega - kv} - \frac{ik\phi_k}{\omega - kv}\frac{\partial f_0(v)}{\partial v}\right]\mathrm{d}v \\ &= -\frac{1}{k^2}\int\frac{if_k(u,0)}{\omega - kv}\mathrm{d}v - \phi_k(\omega)\int\frac{ik}{\omega - kv}\frac{\partial f_0(v)}{\partial v}\mathrm{d}v,\end{aligned} \tag{2.3.7}$$

Equation (2.3.7) is solved for the electrostatic potential

$$\phi_k = \frac{1}{\epsilon_r} \int \frac{f_k(u,0)}{\omega - kv} \mathrm{d}v. \tag{2.3.8}$$

where $\epsilon_r = 1 + \frac{1}{k} \int \frac{1}{\omega - kv} \frac{\partial f_0(v)}{\partial v} \mathrm{d}v$, which can be interpreted as relative permittivity of the plasma. The permittivity describes the ability of an electric field to react to a given perturbation. For later discussions, the electric susceptibility

$$\chi = \epsilon_r - 1 = \frac{1}{k} \int \frac{1}{\omega - kv} \frac{\partial f_0(v)}{\partial v} \mathrm{d}v \tag{2.3.9}$$

is introduced. For waves with a complex frequency Im $\omega \neq 0$, meaning the waves are either growing or damped, $\chi(\omega)$ is an analytical function.

2.3.2 Cauchy argument principle

Two important properties have been shown in this chapter. First, the electric permittivity $\epsilon_r(\omega)$ is an analytic function away from the real axis, meaning no poles sit above or below the real axis. Second, all eigenvalues of the system are determined by $\epsilon_r(\omega) = 0$, which is equivalent to

$$\chi = -\frac{1}{k^2} \int \frac{1}{v - \frac{\omega}{k}} \frac{\partial f_0(v)}{\partial v} \mathrm{d}v = 1. \tag{2.3.10}$$

In complex analysis the Cauchy argument principle states that, given a complex function $f(z)$ defined on a domain Ω and with no poles or roots on the boundary $\partial\Omega$, the closed integral

$$\frac{1}{2\pi i} \oint_{\partial\Omega} \frac{f'(z)}{f(z)} \mathrm{d}z = N - P, \tag{2.3.11}$$

gives the difference between the number of roots N and the number of poles P inside the domain Ω. As stated in section 2.3.1, the susceptibility only has poles on the real axis, thus, when choosing an integration path slightly above the real axis and closing it above, it can be ensured that only root are counted. The computation of the line integral is not straight forward, but the reformulated version of the principle can be used which states that the path integral $\oint_{\partial\Omega} \frac{f'(z)}{f(z)} \mathrm{d}z$ can be interpreted as $2\pi i$ times the winding number of the path $f(\partial\Omega)$ around the origin.
As an example, one can imagine a function $f(z)$ with three roots and one pole as displaced in the left plot of fig. 2.4(a). A closed integration path can be determined that encloses all roots and poles. In this example, I have chosen a semi-circle sitting just above the real axis. When plotting the function $f(z)$ along this path (shown in figure 2.4(b)), the image produces a closed loop, which winds around the origin and the number $N - P$ can be counted.

The argument principle can be applied to the dispersion function 2.3.10 to find

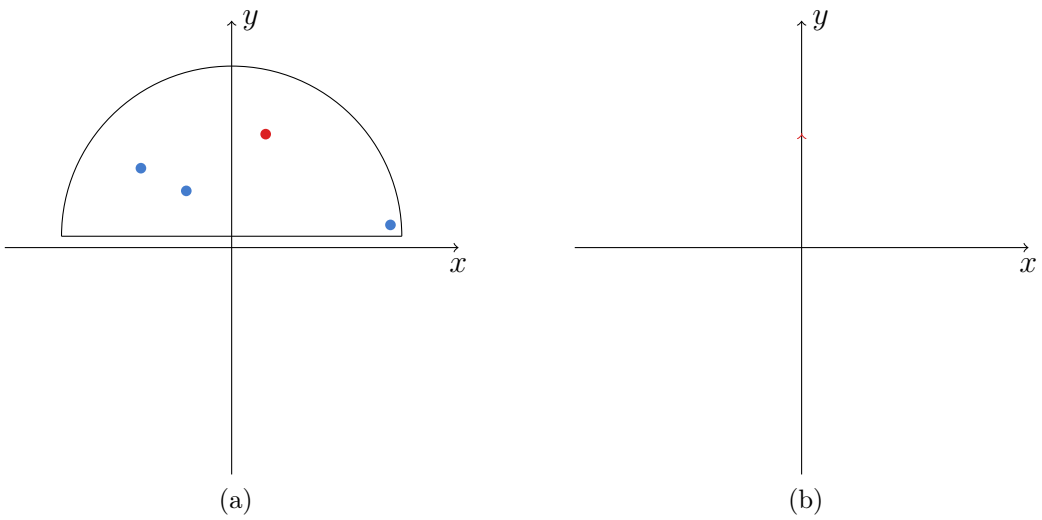

Figure 2.4: Example for the application of the Cauchy principle argument. Given a function $f(z)$, with poles (red) and roots (blue) indicated in the right figure, the image of the contour (closed semi-circle) is displayed in the right figure

unstable modes. A similar integration path as in the example shown in figure 2.4. It consists of a line sitting just above the real axis (to avoid all singularities on the real axis) and closes with in a half circle $\omega = re^{i\theta}$ (with $\theta \in [0, 2\pi]$) in the first and second quadrant. The semicircle is inserted in the susceptibility from equation 2.3.10 $\chi(re^{i\theta})$ and enlarge the radius to infinity $r \to \infty$. The limit shows that $\chi \to 0$ and the contribution to the path integral vanishes which is expected as χ describes the ability of the plasma to react to electrostatic waves which is not possible for waves with infinitely high frequencies.
For a better understanding of the image of the susceptibility on the path along the real axis $\omega = \hat{\omega} + i\epsilon$ ($\hat{\omega}, \epsilon \in \mathbb{R}$ and $\epsilon << \omega$), the real and imaginary part are separated

$$\chi = -\frac{1}{k}\int \frac{(kv-\hat{\omega})}{(kv-\hat{\omega})^2+\epsilon^2}\frac{\partial f_0(v)}{\partial v}\mathrm{d}v - i\frac{1}{k}\int \underbrace{\frac{\epsilon}{(kv-\hat{\omega})^2+\epsilon^2}}_{\delta(v-\frac{\hat{\omega}}{k}),\ \text{for}\ \epsilon\to 0}\frac{\partial f_0(v)}{\partial v}\mathrm{d}v. \qquad (2.3.12)$$

The imaginary part is very small $\propto \epsilon$ expect close to the resonance $\hat{\omega} = kv$. For small $\epsilon \to 0$, imaginary part is $\propto \frac{\partial f}{\partial v}$. Given that imaginary part needs to cross the real axis to complete a winding, the derivative $\left.\frac{\partial f(v)}{\partial v}\right|_{v=\frac{\hat{\omega}}{k_z}}$ has to be zero, and thus $f(\frac{\hat{\omega}}{k_z})$ has a maximum or minimum at the point $\hat{\omega}$ where the image crosses the real axis. Winding numbers are positive, when the image winds around the origin in counterclockwise direction. Hence, to achieve a positive winding number, the imaginary part has to to change its sign form $'+'$ to $'-'$ while the real part is positive which corresponds to a minimum in the distribution function, although the additional requirement that Re $\epsilon_r < 0$ exists. This requirement is also known as the

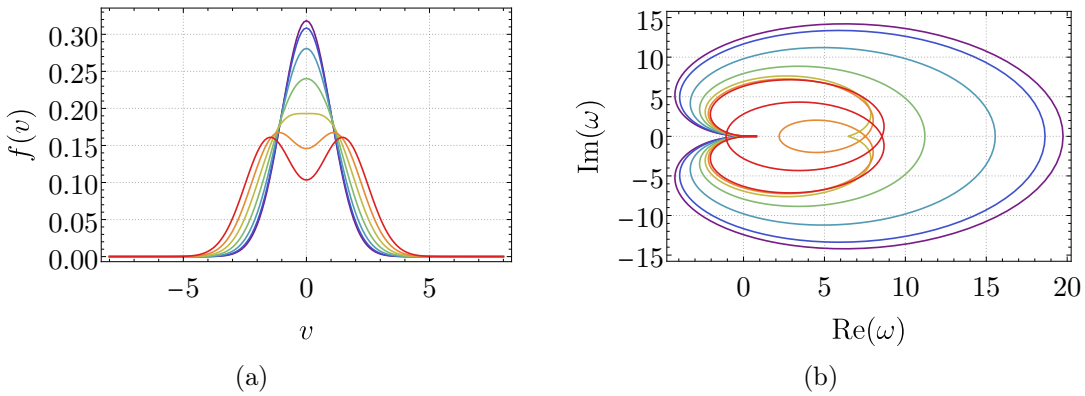

Figure 2.5: Demonstration of Penrose criterion on the example of a two stream instability with various distribution functions (left) and the image of $\epsilon_r(\omega)$ along the real axis (right)

Penrose criterion.
The method of determining the stability is illustrated with the example of a two stream instability, where the distribution function consists of the sum of two Maxwellian distributions with opposing mean velocities. Figure 2.5(a) shows examples distributions for different relative speeds, starting form a relative speed $v_{\text{rel}} = 0$ (purple) to $v_{\text{rel}} = 1.5$ (red), and the image $\epsilon_r(\omega)$ along the real axis on the right. This example demonstrates, that a minimum in the distribution function is not sufficient to cause a growing eigenmode in the system as the two peaks are clearly resolved in the case of the distribution function, but the image can never cross the real axis at Re $\epsilon_r < 1$.

2.3.3 Waves in a magnetized plasma

When introducing a strong, in our consideration immutable, background magnetic field, the behavior of the plasma changes drastically. Most notably, the particles are bound to spiral trajectories around the magnetic field lines which influences how a plasma responds to an electrostatic wave. For the derivation of the distribution function, the frequency of the wave is assume to have a finite and positive imaginary part Im $\omega > 0$, meaning that the wave has a positive growth rate. Thus, we can assume the distribution is unperturbed at $t = -\infty$. Furthermore, it is assumed that the background distribution $f_0(\epsilon)$ is isotropic and only depends on the kinetic energy $\epsilon = v^2/2$. To calculate the linear response of the plasma, the distribution function is split into a background $f_0$and a perturbation δf part $f = f_0 + \delta f$, and it is assumed that $\frac{\delta f}{f_0} \ll 1$ which allows us to neglect the nonlinear term in the Vlasov equation. Inserting this assumptions into 2.2.8 results in

$$\partial_t \delta f + \boldsymbol{v} \cdot \nabla \delta f + (\boldsymbol{v} \times \hat{\boldsymbol{z}}) \cdot \nabla_{\boldsymbol{v}} \delta f = -\boldsymbol{v} \cdot \nabla f_0 - (-\nabla \phi + \boldsymbol{v} \times \hat{\boldsymbol{z}}) \cdot \nabla_{\boldsymbol{v}} f_0. \quad (2.3.13)$$

It can also be useful for the derivation to separate the adiabatic response from our perturbation. The adiabatic response f_{adia} is the distribution function that solves the stationary Vlasov equation for a given electrostatic potential

$$\boldsymbol{v} \cdot \nabla f_{\text{adia}} + (-\nabla\phi + \boldsymbol{v} \times \hat{\boldsymbol{z}}) \cdot \nabla_{\boldsymbol{v}} f_{\text{adia}} = 0. \tag{2.3.14}$$

A solution reads $f_{\text{adia}} = \alpha e^{-\phi} e^{-\epsilon} \approx f_0 - \phi f_0$, where $f_0 = \alpha e^{-\epsilon}$. The background has to form of a thermal distribution, where $\alpha \in \mathbb{R}$ is the normalization factor. Splitting the perturbation $\delta f = h - \phi f_0$ simplifies the linearized Vlasov equation to

$$\begin{aligned} \partial_t h + \boldsymbol{v} \cdot \nabla h + (\boldsymbol{v} \times \hat{\boldsymbol{z}}) \cdot \nabla_{\boldsymbol{v}} h - \partial_t \phi f_0 - \boldsymbol{v} \cdot (\nabla\phi) f_0 - \phi\, (\boldsymbol{v} \times \hat{\boldsymbol{z}}) \cdot \nabla_{\boldsymbol{v}} f_0 \\ = -\, (-\nabla\phi + \boldsymbol{v} \times \hat{\boldsymbol{z}}) \cdot \nabla_{\boldsymbol{v}} f_0. \end{aligned} \tag{2.3.15}$$

The background distribution depends of the absolute value of the velocity, which means that $\nabla_{\boldsymbol{v}} f_0 \perp \boldsymbol{v} \times \hat{\boldsymbol{z}}$. Furthermore, the velocity derivative of the background reads $\nabla_{\boldsymbol{v}} f_0 = -\boldsymbol{v} f_0$. Introducing the these two properties of the distribution function cancels multiple terms and the result reads

$$\partial_t h + \boldsymbol{v} \cdot \nabla h + (\boldsymbol{v} \times \hat{\boldsymbol{z}}) \cdot \nabla_{\boldsymbol{v}} h = \partial_t \phi f_0. \tag{2.3.16}$$

In order to compute the perturbation at the time t, equation (2.3.16) is integrated

$$h(t, \boldsymbol{r}, \boldsymbol{v}) = \int_{-\infty}^{t} \frac{\mathrm{d}h}{\mathrm{d}t'} \mathrm{d}t = f_0 \int \partial_{t'} \phi(\boldsymbol{r}(t'), \boldsymbol{v}(t')) \mathrm{d}t'. \tag{2.3.17}$$

We use a plane wave ansatz for the electrostatic potential $\phi = \phi_k e^{i(\boldsymbol{k}\cdot\boldsymbol{r} - \omega t)}$. In the integral, the phase space position in the integration follows the trajectory of a particle. Assume, a particle at the time t which has the phase space position $(\boldsymbol{r}, \boldsymbol{v})$, its position $(\boldsymbol{r}', \boldsymbol{v}')$ at the time $t' < t$ is given by

$$\begin{aligned} \boldsymbol{r}' &= \boldsymbol{r} - \boldsymbol{\rho} + \boldsymbol{\rho}' + (t' - t) v_z \hat{\boldsymbol{z}}, \\ \boldsymbol{v}' &= v_z \hat{\boldsymbol{z}} + \boldsymbol{v}'_\perp(t). \end{aligned} \tag{2.3.18}$$

The Larmor radius vector $\boldsymbol{\rho} = -v_\perp \times \hat{\boldsymbol{z}}$ points from the gyration center to the particle position. Part of the linearization of the system is that the particles follow unperturbed trajectories. When introducing the plane wave ansatz with the time dependent position vector, an expression for $h(t, \boldsymbol{r}, \boldsymbol{v})$ is obtained

$$h(t, \boldsymbol{r}, \boldsymbol{v}) = -i\omega\phi_k f_0 \int_{-\infty}^{t} e^{i\boldsymbol{k}\cdot(\boldsymbol{r} - \boldsymbol{\rho} + \boldsymbol{\rho}' + (t'-t) v_z \hat{\boldsymbol{z}}) - \omega t'} \mathrm{d}t'. \tag{2.3.19}$$

The amplitude of a Fourier mode $h_k(t, \boldsymbol{v})$ of the distribution function is given by $(h(t, \boldsymbol{v}, \boldsymbol{r}) \to h_k e^{i(\boldsymbol{k}\cdot\boldsymbol{r}-\omega t)}$)

$$h_k = -i\omega\phi_k f_0 \int_{-\infty}^{t} e^{i(k_z v_z-\omega)(t'-t)+i\boldsymbol{k}_\perp\cdot(\boldsymbol{\rho}'-\boldsymbol{\rho})}\mathrm{d}t'. \tag{2.3.20}$$

Before the integral is evaluated, the scalar product $\boldsymbol{k}_\perp \cdot (\boldsymbol{\rho}' - \boldsymbol{\rho})$ is further simplified. We recall, that $\boldsymbol{\rho}$ is the Larmor radius vector at time t and $\boldsymbol{\rho}'$ at time t'. If at time t $\boldsymbol{k}_\perp \cdot \boldsymbol{\rho} = k_\perp v_\perp \sin\alpha$ (the angle α is defined such that $\alpha = 0$ for $\boldsymbol{k}_\perp \parallel \boldsymbol{\rho}$), we get for time $t'$the scalar product $\boldsymbol{k}_\perp \cdot \rho' = k_\perp v_\perp \sin(\alpha + (t' - t))$. The expression $e^{i\boldsymbol{k}_\perp\cdot(\boldsymbol{\rho}'-\boldsymbol{\rho})} = e^{ik_\perp v_\perp[\sin(\alpha+(t'-t))-\sin\alpha]}$ can be rewriting by using the series expansion in Bessel functions

$$\exp(ix\sin\alpha) = \sum_{p\in\mathbb{Z}} J_p(x)\, e^{ip\alpha}. \tag{2.3.21}$$

The exponential function results in

$$\begin{aligned} e^{ik_\perp v_\perp[\sin(\alpha+(t'-t))-\sin\alpha]} &= \left[\sum_{p\in\mathbb{Z}} J_p(k_\perp v_\perp)\, e^{ip(\alpha+(t'-t))}\right]\left[\sum_{m\in\mathbb{Z}} J_m(k_\perp v_\perp)\, e^{-im\alpha}\right] \\ &= \sum_{m,p\in\mathbb{Z}} J_m(k_\perp v_\perp) J_p(k_\perp v_\perp) e^{i(p-m)\alpha+ip(t'-t)}. \end{aligned} \tag{2.3.22}$$

With the modification from equation 2.3.22, the computation of the integral become straight forward

$$\begin{aligned} h_k &= -i\omega f_0\phi_k \sum_{m,p\in\mathbb{Z}} J_m(k_\perp v_\perp) J_p(k_\perp v_\perp) e^{i(p-m)\alpha} \int_{-\infty}^{t} e^{i(k_z v_z-\omega)(t'-t)+ip(t'-t)}\mathrm{d}t' \\ &= \omega f_0\phi_k \sum_{m,p\in\mathbb{Z}} \frac{J_m(k_\perp v_\perp) J_p(k_\perp v_\perp) e^{i(p-m)\alpha}}{\omega - k_z v_z - p}. \end{aligned} \tag{2.3.23}$$

The result describes the general solution of the distribution function in a homogeneous plasma a strong background magnetic field. In case of $\omega \in \mathbb{R}$ it consists of a series of poles on the real axis modified with Bessel functions. These resonance are all located at close (assuming $k_z v_z \ll 1$) to the harmonics of the Larmor frequency.

Particle wave interaction for inhomogeneous background distribution As already stated, the solution in equation 2.3.23 solves the Vlasov equation for an unperturbed background distribution. That the background distribution is not only dependent on the kinetic energy ϵ but is an arbitrary function $S(\boldsymbol{r}, \boldsymbol{v})$. Thus, the distribution function consists of three parts

$$f(\boldsymbol{r}, \boldsymbol{v}) = h(\boldsymbol{r}, \boldsymbol{v}) - \phi(\boldsymbol{r}) f_M(v) + S(\boldsymbol{r}, \boldsymbol{v}), \tag{2.3.24}$$

with the non-adiabatic perturbation $h(\boldsymbol{r}, \boldsymbol{v})$, the adiabatic response to the electrostatic potential $-\phi(\boldsymbol{r}) f_M(v)$ (where the Maxwellian distribution f_M for the background f_0 is introduced w.o.l.g) and additional source distribution $S(\boldsymbol{r}, \boldsymbol{v})$. The last part can contain the non-homogeneous parts of the a thermal distribution, such as temperature and density gradients, but also non-Maxwellian distribution functions. A constraint is imposed on the inhomogeneous background such that it is stationary with the presence of the magnetic field and thus fulfills the equation

$$\boldsymbol{v} \cdot \nabla S + \boldsymbol{v} \times \hat{\boldsymbol{z}} \cdot \nabla_{\boldsymbol{v}} S = 0. \tag{2.3.25}$$

The distribution function can be considered stationary if the distribution function only depends on the position of the gyration center $\boldsymbol{R} = \boldsymbol{r} - \rho$ and the absolute values of the parallel and perpendicular velocities $S(\boldsymbol{r}, \boldsymbol{v}) = S^{\circ}(\boldsymbol{R}, v_{\perp}, v_z)$. The superscript with $\circ$ denotes that source is expressed in gyrocenter coordinates. Having introduced the inhomogeneous background adds another contributions to the linearized Vlasov equation (2.3.16)

$$\partial_t h + \boldsymbol{v} \cdot \nabla h + (\boldsymbol{v} \times \hat{\boldsymbol{z}}) \cdot \nabla_{\boldsymbol{v}} h = \partial_t \phi f_M + \nabla \phi \cdot \nabla_{\boldsymbol{v}} S + \nabla \phi \cdot \boldsymbol{v} f_M, \tag{2.3.26}$$

because the acceleration term of the background $-\nabla \phi \cdot \nabla_{\boldsymbol{v}} S$ and the advection of the adiabatic distribution $-\boldsymbol{v} \cdot \nabla(\phi f_M)$ do not cancel anymore. To compute the distribution function response, we follow the same steps as above. A wave ansatz for the electrostatic potential with a frequency ω with $\operatorname{Im} \omega > 0$ is used and it is assumed that the system is unperturbed at $t = -\infty$. The perturbation at an arbitrary time t can to be obtained by integrating over time

$$h(t, \boldsymbol{r}, \boldsymbol{v}) = \int_{-\infty}^{t} \frac{\mathrm{d}h}{\mathrm{d}t'} \mathrm{d}t = \int (f_M \partial_{t'} \phi + \nabla \phi \cdot \nabla_{\boldsymbol{v}} S + \nabla \phi \cdot \boldsymbol{v} f_M) \mathrm{d}t'. \tag{2.3.27}$$

Now, when we introduce the wave ansatz $\phi = \phi_k e^{i(\boldsymbol{k} \cdot \boldsymbol{r} - \omega t)}$, where we need to introduce the particle trajectories $(\boldsymbol{r}', \boldsymbol{v}')$ from equation (2.3.18). The resulting integral reads

$$h(t, \boldsymbol{r}, \boldsymbol{v}) = (-\omega f_M + \boldsymbol{k} \cdot \nabla_{\boldsymbol{v}} S + \boldsymbol{k} \cdot \boldsymbol{v} f_M) i \phi_k \int_{-\infty}^{t} e^{i \boldsymbol{k} \cdot (\boldsymbol{r} - \boldsymbol{\rho} + \boldsymbol{\rho}' + (t' - t) v_z \hat{\boldsymbol{z}}) - \omega t'} \mathrm{d}t'. \tag{2.3.28}$$

The integral in equation (2.3.28) is in literature typically referred to as the Gordeyev integral for electrostatic waves in magnetized plasma [Mace, 2003]. The background distribution can be written outside the integral because, given the property from equation (2.3.25), it is constant along the particle trajectory. The solution of the integral is the same as for the homogeneous case and for the resulting amplitude of

a Fourier mode of the non-adiabatic distribution function is given by

$$h_k = (\omega f_M - \boldsymbol{k}\cdot\nabla_{\boldsymbol{v}} S - \boldsymbol{k}\cdot\boldsymbol{v} f_M)\phi_k \sum_{m,p\in\mathbb{Z}} \frac{J_m(k_\perp v_\perp)J_p(k_\perp v_\perp)e^{i(p-m)\alpha}}{\omega - k_z v_z - p}. \tag{2.3.29}$$

Before discussing the properties of the general solution, we have a closer look there the contribution of the source term. One has to be careful that the derivatives in the Vlasov equation are always with respect to the phase space variables $(\boldsymbol{r}, \boldsymbol{v})$. The derivative with respect the velocity coordinate $\boldsymbol{v}$ can be rewritten in terms of the derivative with respect to the gyrocenter coordinates

$$\nabla_{\boldsymbol{v}} S(\boldsymbol{r}, \boldsymbol{v}) = \hat{\boldsymbol{z}} \times \nabla_{\boldsymbol{R}} S^\circ(\boldsymbol{R}, \boldsymbol{v}) + \nabla_{\boldsymbol{v}} S^\circ(\boldsymbol{R}, \boldsymbol{v}), \tag{2.3.30}$$

where the first term describes the contribution of spatial gradients, and the second, the influence of the velocity distribution. One has to be careful, when computing the notation of the derivative. When a function is expressed as a function of a set of variables (e.g. $S^\circ(\boldsymbol{R}, \boldsymbol{v})$) and derivative is computed with respect to one of the variables (e.g. $\nabla_{\boldsymbol{v}} S^\circ(\boldsymbol{R}, \boldsymbol{v})$), the other variables (in the example $\boldsymbol{R}$) are held constant. For this section, I refrained from adding an extra notation, for a derivative with respect to variable a with constant variable b, but chose to different names for the functions, when expressed in different coordinate systems.
From the response, macroscopic quantities such as the particle density can be computed and used to derive the dispersion relation. The final dispersion relation will be computed in a later chapter, when it is relevant for the analysis of our simulation results.

2.3.4 Adiabatic electrons and quasi-neutrality

The focus of this work lays on magnetized, electrostatic plasmas, which means that a unchangeable magnetic field is present, but no magnetic field perturbations. Hence, all fields are described by Gauss' law (in this section, I refrain from the normalization, in order to get a better sense of the relations of the quantities)

$$\nabla\cdot\boldsymbol{E} = -\frac{1}{\epsilon_0}\rho = \frac{e}{\epsilon_0}(n_i - n_e), \tag{2.3.31}$$

where $\rho = \sum_s q_s n_s = \sum_s q_s \int f_s \mathrm{d}^3 v$ is the charge density, which is the accumulated charge density of all individual species s. Electrons have a the charge $q_e = -e$ and ions the $q_i = e$. Due to the large mass ration between ion and electrons $\frac{m_i}{m_e} \sim 3600$ (for deuterium ions), the electrons are moving significantly faster than the ions. The thermal velocity v_{th} depends on the square root of the mass and thus, we have a velocity ratio $\frac{v^e_{\mathrm{th}}}{v^i_{\mathrm{th}}} \sim 60$. Because of the large discrepancy between the velocities, it is common when studying the dynamics of one species, the behavior of the other can be simplified. One typical example is the study of electrons with a stationary neutralizing ion background. Normalized to the background density, we

get a Poisson equation which only on the electron density perturbation

$$\frac{\epsilon_0}{e}\nabla \cdot \boldsymbol{E} = -1 + n_e = -1 + \int f_e \mathrm{d}^3 v. \tag{2.3.32}$$

In contrast, when studying ion dynamics it is a quite common approach to assume that electrons respond quasi instantaneously to the behavior of the ions and remain in thermal equilibrium which means that the electrons need to fulfill the stationary Vlasov equation

$$\boldsymbol{v} \cdot \nabla f_e - \frac{q_e}{m_e}\nabla\phi \cdot \nabla_{\boldsymbol{v}} f_e = 0. \tag{2.3.33}$$

It can be shown that the electron distribution function is given by the Boltzmann relation $f_e = e^{-\frac{q_e\phi(\boldsymbol{r})}{T_e}} f_M(v)$, where T_e is the temperature of the electrons [Chen, 1984]. For a small perturbation amplitude $\frac{q_e\phi(\boldsymbol{r})}{T_e} \ll 1$, we can Taylor expand the exponential function and get $f_e \approx f_M - \frac{q_e\phi(\boldsymbol{r})}{T_e} f_M$. Introducing the adiabatic distribution of the electrons into the Poisson equation results in

$$\frac{\epsilon_0}{e}\Delta\phi = n_i - \frac{\phi}{T_e}. \tag{2.3.34}$$

In the quasi-neutral limit, we assume that the electron and ion density are equal $\delta n_i = n_e = \frac{\phi}{T_e}$, which requires the left-hand side to be zero. This condition for the densities gives us a simple equation for the computation of the electrostatic potential.

$$\phi = T_e n_i. \tag{2.3.35}$$

A consequence of the strict quasi-neutrality is, that the plasma frequency $\omega_p = \sqrt{\frac{e^2}{m\epsilon_0}}$ becomes infinite compared to typical system frequencies. This makes intuitive sense, as the electrons respond instantly to the ions and no local charge separation is possible. The quasi-neutrality assumption removes the plasma frequency from the system which in consequence is not required to be resolved numerically.

2.3.5 Penrose criterion for waves in a magnetized plasma

From the combination of the distribution function response to an electrostatic potential and the quasi-neutrality equation the dispersion relation for a magnetized plasma can be formulated. The electrostatic susceptibility χ describes the response of the plasma polarization $\boldsymbol{P}$ of a medium to a present electric field $\boldsymbol{E}$ [Pitaevskii and Lifshitz, 1981]

$$\boldsymbol{P} = \chi\boldsymbol{E} = -\chi\nabla\phi, \tag{2.3.36}$$

where $\boldsymbol{P}$ is the plasma polarization, which is a result of the charge separation in response to an electric field

$$\nabla \cdot \boldsymbol{P} = -\rho = -q \int \delta f \mathrm{d}^3 v - \frac{\phi}{T_e}. \tag{2.3.37}$$

Using the quasi-neutrality equation from equation 2.3.35 and introducing in the relation between the electric field and the plasma polarization results in

$$\chi = \underbrace{\frac{1}{\phi} \int \delta f \mathrm{d}^3 v}_{\chi_i} - \underbrace{\frac{1}{T_e}}_{\chi_e} = \sum_s \chi_s, \tag{2.3.38}$$

which can also be seen as the of the responses of the individual species. The dispersion relation is then given by $\chi = 0$.
Introducing the distribution function response to the electrostatic potential including the source term from equation 2.3.29, we obtain for $T_e = T_i = 1$ (remember $\delta f = h - \phi f_M$)

$$\chi(\boldsymbol{k}, \omega) = \int \left[(\omega f_M - \boldsymbol{k} \cdot \nabla_{\boldsymbol{v}} S - \boldsymbol{k} \cdot \boldsymbol{v} f_M) i \sum_{m,p \in \mathbb{Z}} \frac{J_m(k_\perp v_\perp) J_p(k_\perp v_\perp) e^{i(p-m)\alpha}}{\omega - k_z v_z - p} \right] \mathrm{d}^3 v - 2. \tag{2.3.39}$$

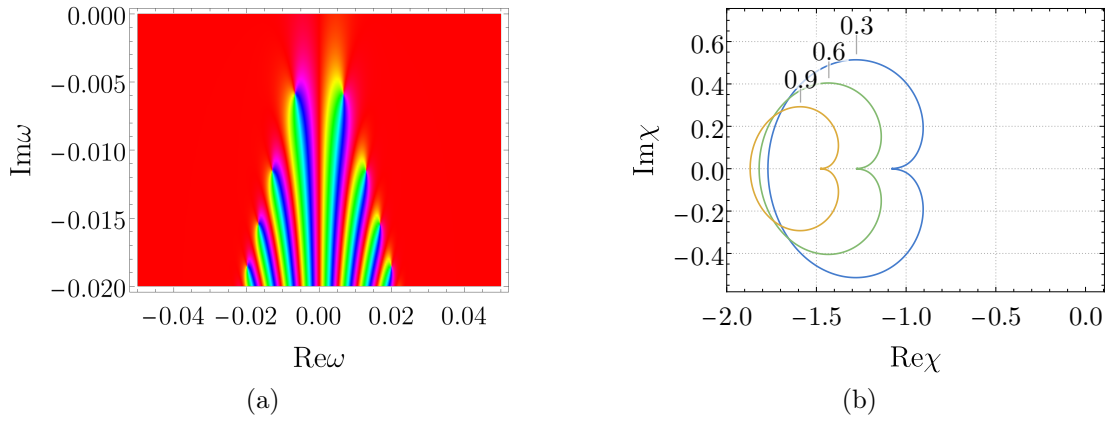

Figure 2.6: Imaginary part of susceptibility for $S = 0$, $k_z = \frac{1}{240}$ and $k_\perp = 0.2$ (a) and parametric plot of $(\mathrm{Re}\chi(\omega), \mathrm{Im}\ \chi(\omega)$ for various $k_\perp$ (indicated by label)

Figure 2.6(a) displays an example susceptibility for a fixed $\boldsymbol{k}$ in the case without a source term $S = 0$. The plot shows the complex phase Im $\log \chi$, as this best illustrates the roots of the function. A point in the graph is a root, if any arbitrary path around the point goes through all the different colors of the color pallet. The pyramidal distribution is very typical distribution of Landau damped modes and is an intrinsic property of the Gordeyev integral. In the second plot 2.6(b), I have

displayed a parametric plot of the real (x-axis) and the imaginary (y-axis) part of the susceptibility as a function of $\omega \in \mathbb{R}$ for a fixed k_z and various $k_\perp$. Section 2.3.2 has discussed that the argument principle is a way to determine whether there are any roots of a function above the real axis, ergo waves with a positive growth rate. In case of a homogeneous plasma in thermal equilibrium no instabilities, and thus no roots with Im $\omega > 0$ exist. In later chapters, multiple options for the source S and the resulting instabilities will be discussed.
The like between the two illustrations can be understood as follows. The colors in the left plot represent the phase, of the complex susceptibility. When the image of the susceptibility of on around a closed path, goes around the origin exactly once, it takes every complex phase value at least one time which corresponds to the a path covering all the colors in the left image.

2.4 Formulating the 6D kinetic equation in gyrocenter coordinates

The introduction (section 1.3) has discussed that gyrokinetic theory is the most commonly used model for kinetic plasma simulations, however, it is limited to applications in with small gradients and low frequencies. To utilize the benefits of the gyrokinetic coordinate system without the limitations, the following framework has been developed The derivation follow the ansatz of cyclokinetics [Deng et al., 2016], while avoiding any linearizations that have been done in the works of Waltz et al..
We start with an arbitrary distribution function in gyrocenter coordinates $g(\boldsymbol{R}, v_\perp, v_z, \alpha)$, where $\boldsymbol{R} = \boldsymbol{r} + \boldsymbol{v} \times \hat{\boldsymbol{z}}$, is the gyration center for a given particle with phase space position $(\boldsymbol{r}, \boldsymbol{v})$. The dependency on the velocity angle α is rewritten as an expansion of Fourier modes

$$g(\boldsymbol{R}, v_\perp, v_z, \alpha) = \sum_{m \in \mathbb{Z}} e^{im\alpha} g_m(\boldsymbol{R}, v_\perp, v_z). \tag{2.4.1}$$

The distribution function is written in the particle frame $(\boldsymbol{r}, \boldsymbol{v})$ as well

$$f(\boldsymbol{r}, \boldsymbol{v}) = g(\boldsymbol{R}(\boldsymbol{r}, \boldsymbol{v}), v_\perp, v_z, \alpha) = \sum_{m \in \mathbb{Z}} e^{im\alpha} g_m(\boldsymbol{r} + \boldsymbol{v} \times \hat{\boldsymbol{z}}, v_\perp, v_z). \tag{2.4.2}$$

The ansatz in equation (2.4.2) for the distribution function is introduced into the Vlasov equation

$$\partial_t f + \boldsymbol{v} \cdot (\nabla_{\boldsymbol{r}} f)_{\boldsymbol{v}} + (-\nabla_{\boldsymbol{r}} \phi + \boldsymbol{v} \times \hat{\boldsymbol{z}}) \cdot (\nabla_{\boldsymbol{v}} f)_{\boldsymbol{r}} = 0. \tag{2.4.3}$$

Caution has to be taken, because the gradients in the Vlasov equation $\nabla, \nabla_{\boldsymbol{v}}$, are computed with respect to the particle coordinates, keeping the conjugated variable constant. We introduce a notation to clarify which coordinate is derived and which is held constant. For the spatial gradient $\nabla f \to (\nabla_{\boldsymbol{r}} f)_{\boldsymbol{v}}$, the derivative is computed

with respect to the components of $\boldsymbol{r}$ at a constant velocity $\boldsymbol{v}$. For the velocity gradient $\nabla_{\boldsymbol{v}} f \to (\nabla_{\boldsymbol{v}} f)_{\boldsymbol{r}}$, the derivative is computed with respect to $\boldsymbol{v}$ at a constant particle position $\boldsymbol{r}$.
The gradients of the distribution function are evaluated individually, before they are introduced into the Vlasov equation. The spatial gradient, after applying the chain rule, reads

$$\left(\nabla_{\boldsymbol{r}} g(\boldsymbol{R}(\boldsymbol{r},\boldsymbol{v}),\boldsymbol{v})\right)_{\boldsymbol{v}} = \nabla_{\boldsymbol{r}}\boldsymbol{R}\cdot\left(\nabla_{\boldsymbol{R}} g(\boldsymbol{R}(\boldsymbol{r},\boldsymbol{v}),\boldsymbol{v})\right)_{\boldsymbol{v}} = \left(\nabla_{\boldsymbol{R}} g(\boldsymbol{R}(\boldsymbol{r},\boldsymbol{v}),\boldsymbol{v})\right)_{\boldsymbol{v}}. \tag{2.4.4}$$

The expression does not change with the transformation as $\nabla_{\boldsymbol{r}}\boldsymbol{R} = \mathbb{1}$ is the identity. For the velocity gradient, one needs to be careful that the gyrocenter coordinate $\boldsymbol{R} = \boldsymbol{r} + \boldsymbol{v}\times\hat{\boldsymbol{z}}$ also has a velocity dependency, and the velocity gradient in is computed with constant $\boldsymbol{r}$, not $\boldsymbol{R}$. The resulting expression for the gradient is

$$\begin{aligned}\left(\nabla_{\boldsymbol{v}} g(\boldsymbol{R}(\boldsymbol{r},\boldsymbol{v}),\boldsymbol{v})\right)_{\boldsymbol{r}} &= \nabla_{\boldsymbol{v}}\boldsymbol{R}\cdot\left(\nabla_{\boldsymbol{R}} g\right)_{\boldsymbol{v}} + \left(\nabla_{\boldsymbol{v}} g\right)_{\boldsymbol{R}} \\ &= \hat{\boldsymbol{z}}\times\left(\nabla_{\boldsymbol{R}} g\right)_{\boldsymbol{v}} + \left(\nabla_{\boldsymbol{v}} v_\perp\right)\left(\frac{\partial g}{\partial v_\perp}\right)_{\boldsymbol{R}} + \left(\nabla_{\boldsymbol{v}} v_z\right)\left(\frac{\partial g}{\partial v_z}\right)_{\boldsymbol{R}} + \left(\nabla_{\boldsymbol{v}}\alpha\right)\left(\frac{\partial g}{\partial \alpha}\right)_{\boldsymbol{R}} \\ &= \hat{\boldsymbol{z}}\times\left(\nabla_{\boldsymbol{R}} g\right)_{\boldsymbol{v}} + \hat{\boldsymbol{v}}_\perp\left(\frac{\partial g}{\partial v_\perp}\right)_{\boldsymbol{R}} + \hat{\boldsymbol{v}}_z\left(\frac{\partial g}{\partial v_z}\right)_{\boldsymbol{R}} + \frac{\hat{\boldsymbol{\rho}}}{v_\perp}\left(\frac{\partial g}{\partial \alpha}\right)_{\boldsymbol{R}},\end{aligned} \tag{2.4.5}$$

where $(\hat{\boldsymbol{z}}, \hat{\boldsymbol{v}}_\perp, \hat{\boldsymbol{\rho}} = \hat{\boldsymbol{z}}\times\hat{\boldsymbol{v}})$ is defined such that it forms a right-handed coordinate system. The derivatives are split into their components and color coded such that the derivation can easier be followed. When computing the scalar product with the force vector $-\nabla\phi$ and $\boldsymbol{v}\times\hat{\boldsymbol{z}}$, some of the terms are zero because $\boldsymbol{v}\times\hat{\boldsymbol{z}} \perp \hat{\boldsymbol{v}}_\perp$, $\boldsymbol{v}\times\hat{\boldsymbol{z}} \perp \hat{\boldsymbol{v}}_z$ and $(\boldsymbol{v}\times\hat{\boldsymbol{z}})\cdot\hat{\boldsymbol{\rho}} = -v$. This simplifies some of the expressions. Furthermore, we introduce the harmonic expansion of our distribution function form equation 2.4.2. The spatial advection term reads,

$$\boldsymbol{v}\cdot\left(\nabla_{\boldsymbol{R}} g\right)_{\boldsymbol{v}} = \sum_{m\in\mathbb{Z}} e^{im\alpha}\left[\boldsymbol{v}\cdot\left(\nabla_{\boldsymbol{R}} g_m\right)_{\boldsymbol{v}}\right], \tag{2.4.6}$$

while we write the velocity advection term separately for the electric field $\nabla\phi$ and magnetic field $\hat{\boldsymbol{z}}$ advection

$$\begin{aligned}-\left(\nabla_{\boldsymbol{R}}\phi\right)_{\boldsymbol{v}}\cdot\left(\nabla_{\boldsymbol{v}} g\right)_{\boldsymbol{r}} = \sum_{m\in\mathbb{Z}} e^{im\alpha}\Bigg[&-\left(\nabla_{\boldsymbol{R}}\phi\right)_{\boldsymbol{v}}\cdot\left(\hat{\boldsymbol{z}}\times\left(\nabla_{\boldsymbol{R}} g_m\right)_{\boldsymbol{v}}\right) - \left(\nabla_{\boldsymbol{R}}\phi\right)_{\boldsymbol{v}}\cdot\hat{\boldsymbol{v}}_\perp\left(\frac{\partial g_m}{\partial v_\perp}\right)_{\boldsymbol{R}} \\ &-\left(\nabla_{\boldsymbol{R}}\phi\right)_{\boldsymbol{v}}\cdot\hat{\boldsymbol{v}}_z\left(\frac{\partial g_m}{\partial v_z}\right)_{\boldsymbol{R}} - \frac{im}{v_\perp}\left(\nabla_{\boldsymbol{R}}\phi\right)_{\boldsymbol{v}}\cdot\hat{\boldsymbol{\rho}} g_m\Bigg],\end{aligned} \tag{2.4.7}$$

$$\left(\boldsymbol{v}\times\hat{\boldsymbol{z}}\right)\cdot\left(\nabla_{\boldsymbol{v}} g\right)_{\boldsymbol{r}} = \sum_{m\in\mathbb{Z}} e^{im\alpha}\left[-\boldsymbol{v}_\perp\cdot\left(\nabla_{\boldsymbol{R}} g_m\right)_{\boldsymbol{v}} + \left(\boldsymbol{v}\times\hat{\boldsymbol{z}}\right)\cdot\hat{\boldsymbol{\rho}}\frac{im}{v_\perp} g_m\right]. \tag{2.4.8}$$

Before introducing all terms together in the Vlasov equation, we recognize that perpendicular component of the spatial advection term (2.4.6) and the first term in (2.4.8) cancel and only the parallel advection term survives. Hence, we obtain for the Vlasov equation in gyrocenter coordinates ($(\boldsymbol{v} \times \hat{\boldsymbol{z}}) \cdot \hat{\boldsymbol{\rho}} = -v$)

$$\sum_{m\in\mathbb{Z}} e^{im\alpha} \left[\frac{\partial g_m}{\partial t} + v_z \left(\frac{\partial g_m}{\partial z} \right)_{\boldsymbol{v}} - img_m \right. \\ \left. - (\nabla_{\boldsymbol{R}}\phi)_{\boldsymbol{v}} \cdot \left(\hat{\boldsymbol{v}}_\perp \left(\frac{\partial g_m}{\partial v_\perp} \right)_{\boldsymbol{R}} + \hat{\boldsymbol{v}}_z \left(\frac{\partial g_m}{\partial v_z} \right)_{\boldsymbol{R}} + \frac{im}{v_\perp} \hat{\boldsymbol{\rho}} g_m + \hat{\boldsymbol{z}} \times (\nabla_{\boldsymbol{R}} g_m)_{\boldsymbol{v}} \right) \right] = 0. \tag{2.4.9}$$

To get a better understanding of the nonlinear term

$$\Xi_m = (\nabla_{\boldsymbol{R}}\phi)_{\boldsymbol{v}} \cdot \left(\hat{\boldsymbol{v}}_\perp \left(\frac{\partial g_m}{\partial v_\perp} \right)_{\boldsymbol{R}} + \hat{\boldsymbol{v}}_z \left(\frac{\partial g_m}{\partial v_z} \right)_{\boldsymbol{R}} + \frac{im}{v_\perp} \hat{\boldsymbol{\rho}} g_m + \hat{\boldsymbol{z}} \times (\nabla_{\boldsymbol{R}} g_m)_{\boldsymbol{v}} \right), \tag{2.4.10}$$

some angle considerations are done. One has to be careful that the electrostatic potential, written in gyrocenter coordinates, has a velocity dependency. The spatial derivative $(\nabla_{\boldsymbol{R}}\phi)_{\boldsymbol{v}}$ can be expressed in terms of the velocity components, the gyroangle α (figure 2.7(a)) and the absolute value of the perpendicular velocity $v_\perp$ (figure 2.7(b)). For instance, for small change in α, the potential $\phi(\boldsymbol{r})$ is varied slightly in the direction of $\hat{\boldsymbol{v}}_\perp$ (compare figure 2.7(a)). In case the absolute value of the perpendicular velocity is changed, the radius of the gyration increases or decreases and $\boldsymbol{r}$ changes in the direction of the Larmor radius vector $\hat{\boldsymbol{\rho}}$ (compare figure 2.7(b)). With these consideration, the derivative $(\nabla_{\boldsymbol{r}}\phi)_{\boldsymbol{v}}$ can be expressed as a derivative with respect to the gyrocenter coordinate $\boldsymbol{R}$ as well as the perpendicular velocity coordinates $(v_\perp, \alpha)$

$$(\nabla_{\boldsymbol{R}}\phi)_{\boldsymbol{v}} \leftrightarrow \hat{\boldsymbol{v}}_\perp \frac{1}{v_\perp} \left(\frac{\partial \phi}{\partial \alpha} \right)_{\boldsymbol{R}} + \hat{\boldsymbol{\rho}}_\perp \left(\frac{\partial \phi}{\partial v_\perp} \right)_{\boldsymbol{R}}. \tag{2.4.11}$$

The reformulation of the gradient in equation (2.4.11) is used to further modify the

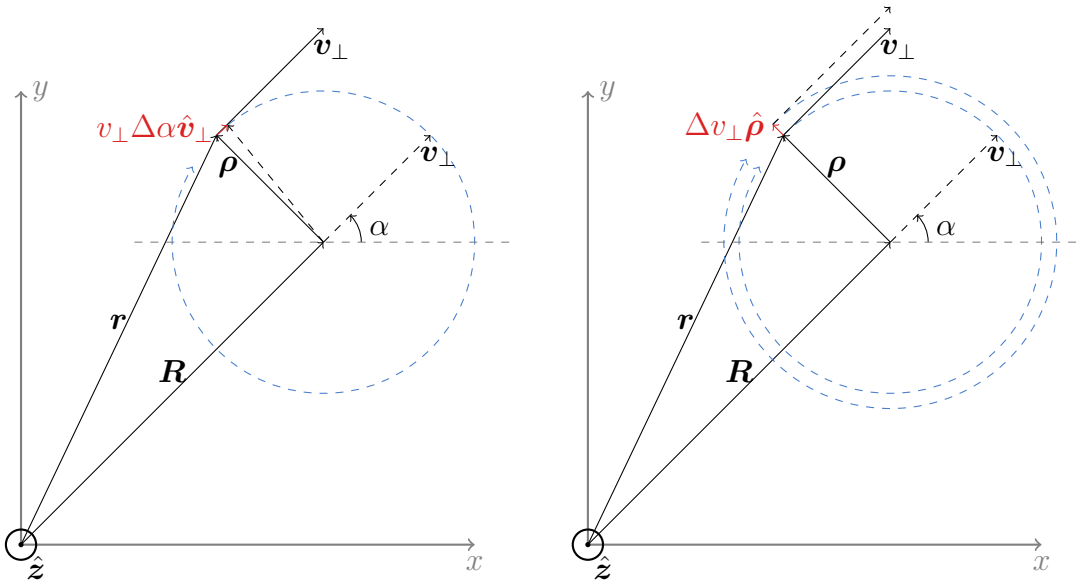

Figure 2.7: Illustration of transformation of spatial derivative of the electrostatic potential $(\nabla_{\boldsymbol{R}}\phi)_{\boldsymbol{v}}$, in terms of a derivative with respect to α (a) or $v_\perp$ (b)

nonlinear term

$$
\begin{aligned}
&(\nabla_{\boldsymbol{R}}\phi)_{\boldsymbol{v}} \cdot (\nabla_{\boldsymbol{v}} g(\boldsymbol{R}(\boldsymbol{r},\boldsymbol{v}),\boldsymbol{v}))_{\boldsymbol{r}} \\
&= (\nabla_{\boldsymbol{R}}\phi)_{\boldsymbol{v}} \cdot \left(\hat{\boldsymbol{z}} \times (\nabla_{\boldsymbol{R}} g)_{\boldsymbol{v}} + \hat{\boldsymbol{v}}_\perp \left(\frac{\partial g}{\partial v_\perp}\right)_{\boldsymbol{R}} + \hat{\boldsymbol{v}}_z \left(\frac{\partial g}{\partial v_z}\right)_{\boldsymbol{R}} + \frac{\hat{\boldsymbol{\rho}}}{v_\perp}\left(\frac{\partial g}{\partial \alpha}\right)_{\boldsymbol{R}} \right) \\
&= (\nabla_{\boldsymbol{R}}\phi)_{\boldsymbol{v}} \cdot \left(\hat{\boldsymbol{z}} \times (\nabla_{\boldsymbol{R}} g)_{\boldsymbol{v}} + \hat{\boldsymbol{v}}_z \left(\frac{\partial g}{\partial v_z}\right)_{\boldsymbol{R}} \right) + \hat{\boldsymbol{v}}_\perp \cdot (\nabla_{\boldsymbol{R}}\phi)_{\boldsymbol{v}} \left(\frac{\partial g}{\partial v_\perp}\right)_{\boldsymbol{R}} + \frac{\hat{\boldsymbol{\rho}}}{v_\perp} \cdot (\nabla_{\boldsymbol{R}}\phi)_{\boldsymbol{v}} \left(\frac{\partial g}{\partial \alpha}\right)_{\boldsymbol{R}} \\
&= (\nabla_{\boldsymbol{R}}\phi)_{\boldsymbol{v}} \cdot \left(\hat{\boldsymbol{z}} \times (\nabla_{\boldsymbol{R}} g)_{\boldsymbol{v}} + \hat{\boldsymbol{v}}_z \left(\frac{\partial g}{\partial v_z}\right)_{\boldsymbol{R}} \right) + \frac{1}{v_\perp}\left(\frac{\partial \phi}{\partial \alpha}\right)_{\boldsymbol{R}} \left(\frac{\partial g}{\partial v_\perp}\right)_{\boldsymbol{R}} + \frac{1}{v_\perp}\left(\frac{\partial \phi}{\partial v_\perp}\right)_{\boldsymbol{R}} \left(\frac{\partial g}{\partial \alpha}\right)_{\boldsymbol{R}}.
\end{aligned}
\tag{2.4.12}
$$

The nonlinear is rewritten in terms of the Fourier components of the quantities. When computing the Fourier transform of the distribution function and the electrostatic potential, one has to be careful in which coordinate system the quantity is defined. The electrostatic potential is a function of the particle coordinates $\boldsymbol{r}$. The Fourier with respect to the gyrocenter coordinate $\phi^*(\boldsymbol{p}) := \mathcal{FT}_{\boldsymbol{R}}(\phi(\boldsymbol{r}))$ is expressed in terms of the Fourier component $\phi(\boldsymbol{p}) = \int \phi(\boldsymbol{r}) e^{-i\boldsymbol{p}\cdot\boldsymbol{r}} \mathrm{d}^3 r$

$$
\phi^*(\boldsymbol{p}) = \mathcal{FT}_{\boldsymbol{R}}(\phi(\boldsymbol{r})) = \int \phi(\boldsymbol{r}) e^{-i\boldsymbol{R}\cdot\boldsymbol{p}} \mathrm{d}^3 R = \int \phi(\boldsymbol{r}) e^{-i(\boldsymbol{r}\cdot\boldsymbol{p} + \boldsymbol{p}\cdot(\boldsymbol{v}\times\hat{\boldsymbol{z}}))} \mathrm{d}^3 r = e^{-i\boldsymbol{p}\cdot(\boldsymbol{v}\times\hat{\boldsymbol{z}})}\phi(\boldsymbol{p}).
\tag{2.4.13}
$$

The scalar product in the exponent is rewritten with the definition of α, such that $\boldsymbol{p}\cdot(\boldsymbol{v}\times\hat{\boldsymbol{z}}) = p_\perp v_\perp \sin(\alpha-\alpha_p)$, where α_p is the angle between the wave vector $\boldsymbol{p}$ and the x-axis. Now, the exponential function is expanded as a series of Bessel functions

$$\phi^*(\boldsymbol{p}) = e^{-i\boldsymbol{p}\cdot(\boldsymbol{v}\times\hat{\boldsymbol{z}})}\phi(\boldsymbol{p}) = e^{-ip_\perp v_\perp \sin(\alpha-\alpha_p)}\phi(\boldsymbol{p}) = \phi(\boldsymbol{p})\sum_{n\in\mathbb{Z}} J_{-n}(p_\perp v_\perp)e^{in(\alpha-\alpha_p)}. \tag{2.4.14}$$

The Fourier transformed electrostatic potential is split into modes n of the velocity angle $\phi_n^*(\boldsymbol{p}) = \phi(\boldsymbol{p})J_{-n}(p_\perp v_\perp)e^{-in\alpha_p}$, with $\phi^*(\boldsymbol{p}) = \sum_{n\in\mathbb{Z}}\phi_n^* e^{in\alpha}$, helps to compute the derivatives

$$\frac{1}{v_\perp}\left(\frac{\partial \phi_n^* e^{in\alpha}}{\partial\alpha}\right)_{\boldsymbol{p}} = \frac{\phi_n^*}{v_\perp}\left(\frac{\partial e^{in\alpha}}{\partial\alpha}\right)_{\boldsymbol{p}} = \frac{in}{v_\perp}\phi_n^* \qquad \text{, and} \tag{2.4.15}$$

$$\left(\frac{\partial\phi_n^*}{\partial v_\perp}\right)_{\boldsymbol{p}} = p_\perp\phi(\boldsymbol{p})J'_{-n}(p_\perp v_\perp)e^{-in\alpha_p}. \tag{2.4.16}$$

The derivatives in equation (2.4.16) are used to compute the blue and green term in equation (2.4.12) which result in

$$\underline{\frac{1}{v_\perp}\left(\frac{\partial\phi}{\partial\alpha}\right)_{\boldsymbol{R}}\left(\frac{\partial g}{\partial v_\perp}\right)_{\boldsymbol{R}}} \to \frac{in}{v_\perp}\phi_n^*(\boldsymbol{p})\partial_{v_\perp} g^{\boldsymbol{q}}, \tag{2.4.17}$$

$$\underline{\frac{1}{v_\perp}\left(\frac{\partial\phi}{\partial v_\perp}\right)_{\boldsymbol{R}}\left(\frac{\partial g}{\partial\alpha}\right)_{\boldsymbol{R}}} \to \frac{p_\perp}{v_\perp}\phi_n(\boldsymbol{p})J'_{-n}(\xi)\partial_\alpha g^{\boldsymbol{q}} e^{-in\alpha_p}, \tag{2.4.18}$$

when written in terms of the Fourier modes of the potential and the distribution function $g^{\boldsymbol{q}}$. The red and the purple term result in

$$\underline{(\nabla_{\boldsymbol{R}}\phi)_{\boldsymbol{v}}\cdot\hat{\boldsymbol{v}}_z\left(\frac{\partial g}{\partial v_z}\right)_{\boldsymbol{R}}} \to ip_z\phi_n^*(\boldsymbol{p})\partial_{v_z} g^{\boldsymbol{q}}, \tag{2.4.19}$$

and

$$\begin{aligned}\underline{(\nabla_{\boldsymbol{R}}\phi)_{\boldsymbol{v}}\cdot\hat{\boldsymbol{z}}\times(\nabla_{\boldsymbol{R}} g)_{\boldsymbol{v}}} &\to -\boldsymbol{p}\cdot(\hat{\boldsymbol{z}}\times\boldsymbol{q})\phi_n^* g^{\boldsymbol{q}} \\ &= -p_\perp q_\perp \sin(\alpha_p-\alpha_q)\phi_n^* g^{\boldsymbol{q}}.\end{aligned} \tag{2.4.20}$$

At this point, the expansion from equation (2.4.1) is introduced. The nonlinear interaction between the two modes $\phi^*(\boldsymbol{p})$ and $g_m^{\boldsymbol{q}}$ is written as $\Xi_m^{\boldsymbol{p},\boldsymbol{q}} = \sum_{n\in\mathbb{Z}} e^{in\alpha}\Xi_{m,n}^{\boldsymbol{p},\boldsymbol{q}}$, where

$$\begin{aligned}\Xi_{m,n}^{\boldsymbol{p},\boldsymbol{q}} := \phi^{\boldsymbol{p}} e^{-in\alpha_p}\Bigg[&\left(\underline{\frac{in}{v_\perp}\partial_{v_\perp} g_m^{\boldsymbol{q}}} + \underline{ip_z\partial_{v_z} g_m^{\boldsymbol{q}}} - \underline{p_\perp q_\perp\sin(\alpha_p-\alpha_q)g_m^{\boldsymbol{q}}}\right)J_{-n}(\xi) \\ &+\underline{\frac{imp_\perp}{v_\perp}J'_{-n}(\xi)g_m^{\boldsymbol{q}}}\Bigg].\end{aligned} \tag{2.4.21}$$

It is important, that in expression (2.4.21), $\phi^{\boldsymbol{p}} = \phi(p)$ is the Fourier component of the electrostatic potential in particle coordinates.
Before we reintroduce the nonlinear term into the Vlasov equation, the interactions of all modes have to be considered, not only two only two with $(m, \boldsymbol{q})$ and $(n, \boldsymbol{p})$. Any mode $(l, \boldsymbol{k})$ is influenced by all modes with $l = n + m$ and $\boldsymbol{k} = \boldsymbol{p} + \boldsymbol{q}$, thus, the entire Vlasov equation reads

$$\begin{aligned}\frac{\partial g_l^{\boldsymbol{k}}}{\partial t} &= -ik_z v_z g_l^{\boldsymbol{k}} + ilg_l + \sum_{\substack{n,m\in\mathbb{Z}\\ l=n+m}} \iint_{\boldsymbol{k}=\boldsymbol{p}+\boldsymbol{q}} \Xi_{m,n}^{\boldsymbol{p},\boldsymbol{q}} \mathrm{d}\boldsymbol{p}\mathrm{d}\boldsymbol{q} \\ &= -ik_z v_z g_l^{\boldsymbol{k}} + ilg_l + \sum_{m\in\mathbb{Z}} \int \Xi_{m,l-m}^{\boldsymbol{p},\boldsymbol{k}-\boldsymbol{p}} \mathrm{d}\boldsymbol{p}, \text{ with} \end{aligned} \tag{2.4.22}$$

For a better comparability with the results from the derivation of cyclokinetics by Waltz et al., some Bessel function identities are used

$$\begin{aligned}\Xi_l^{\boldsymbol{p},\boldsymbol{q}} = \sum_{m\in\mathbb{Z}} \phi^{\boldsymbol{p}} e^{-in\alpha_p} \Big[& ip_z \partial_{v_z} g_m^{\boldsymbol{q}} \\ & - p_\perp q_\perp \sin(\alpha_p - \alpha_q) g_m^{\boldsymbol{q}} J_{m-l}(\xi) \\ & - \frac{mp_\perp}{2v_\perp i} \left(J_{m-l-1}(\xi) - J_{m-l+1}(\xi)\right) g_m^{\boldsymbol{q}} \\ & - \frac{p_\perp}{2i} \left(J_{m-l-1}(\xi) + J_{m-l+1}(\xi)\right) \partial_{v_\perp} g_m^{\boldsymbol{q}} \Big], \end{aligned} \tag{2.4.23}$$

which gives us an expression that is the corresponding to (2.2.11) in [Deng et al., 2016].
For the gyrokinetic equation, we assume that all contributions of the distribution function with an $m \neq 0$ are zero, thus we obtain

$$\frac{\partial g_0^{\boldsymbol{k}}}{\partial t} = -iv_z k_z g_0^{\boldsymbol{k}} + \int \phi^{\boldsymbol{p}} \left(ip_z \partial_{v_z} g_0^{\boldsymbol{k}-\boldsymbol{p}} - p_\perp (k_\perp - p_\perp) \sin(\alpha_p - \alpha_{k-p}) g_0^{\boldsymbol{k}-\boldsymbol{p}} \right) \mathrm{d}\boldsymbol{p}, \tag{2.4.24}$$

which is equivalent to

$$\frac{\partial g_0}{\partial t} = -v_z \partial_z g_0 + \partial_z \phi \partial_{v_z} g_0 - (\nabla_{\boldsymbol{R}} \phi^\circ(\boldsymbol{R}) \times \hat{\boldsymbol{z}}) \cdot \nabla_{\boldsymbol{R}} g_0. \tag{2.4.25}$$

Three terms are remaining, which are in order, the parallel spatial advection, the parallel acceleration by the electric field and the $\boldsymbol{E} \times \boldsymbol{B}$-advection.

2.5 Comparison to gyrokinetic theory

2.5.1 Gyrokinetic ordering

A complete derivation of the gyrokinetic equations can be found in literature [Sugama and Horton, 1998]. For the gyrokinetic ordering is be helpful to introduce the quantities (for the discussion of the ordering, refrain from normalizing the quantities)

$$c_s = \sqrt{\frac{T}{m}} \qquad \text{(sound speed)}, \tag{2.5.1}$$

$$\varrho_s = \frac{c_s}{\omega_c} \qquad \text{(sound-speed gyroradius)}, \tag{2.5.2}$$

with the temperature T and the cyclotron frequency $\omega_c = \frac{qB}{m}$. To quantify the magnitude of the different perturbations, the dimensionless quantity $\varrho^* = \frac{\varrho_s}{R}$ (R is the characteristic system length) is typically introduced. In gyrokinetic models, the sound speed gyroradius is considered to be small compared to R and, therefore, $\varrho^* \ll 1$. All quantities are quantified in powers of ϱ^*.
Furthermore, it is assumed in gyrokinetic theory that the perturbation length scale perpendicular to the magnetic field $k_\perp^{-1}$ is of the same order as the sound-speed gyroradius, $\varrho_s k_\perp \sim 1$, and the length scale of the perturbations parallel to the field lines is larger by a factor of $\frac{1}{\varrho^*}$. The gyrokinetic ordering [Dubin et al., 1983] written in terms of ϱ^* reads

$$\frac{\delta g_0}{f_M} \sim \frac{q\phi}{T} \sim \frac{k_z}{k_\perp} \sim \frac{\omega}{\omega_c} \sim \varrho^*, \tag{2.5.3}$$

where f_M is the homogeneous background Maxwell distribution function and $\delta g_0 = g_0 - f_M$ is the perturbation of the distribution function.
The ordering in equation (2.5.3) summarizes the main assumptions for the derivation of an electrostatic gyrokinetic model. Firstly, it is assumed that the perturbation of the distribution function is small compared to the thermal background. Furthermore, the energy of the electrostatic energy $q\phi$ is small compared to thermal energy T, the parallel wavenumber k_z is small compared to the perpendicular wavenumber $k_\perp$ and the frequencies in the system ω are small compared to the Larmor frequency $\omega_c = \frac{qB}{m}$.

2.5.2 Gyrokinetic equation

The perturbation of the distribution function g_0 consists of two parts. First, the adiabatic perturbation, which originates in a given perturbed electrostatic potential ϕ and second, the non-adiabatic perturbation. The latter is defined as

$$h(\boldsymbol{R}, \boldsymbol{v}, t) := \delta g(\boldsymbol{R}, \boldsymbol{v}) + \phi(\boldsymbol{R}) f_M. \tag{2.5.4}$$

The focus of this work lies on instabilities in slab geometry, in which case, all magnetic field lines are straight and no curvature or gradients in the background magnetic field are present.
The gyrokinetic equation is derived by applying the coordinate transformation from section (2.5.3) is applied and the kinetic equation is reduced such that is only depends on the gyrokinetic distribution (by applying the same coordinate transformation as above in section 2.4 and averaging over the velocity angle. After the ordering (eq. (2.5.3))is applied, the electrostatic gyrokinetic equation for slab geometry is obtained [Candy and Waltz, 2003]

$$\frac{\partial \delta g}{\partial t} + v_z \partial_z h + (\hat{\boldsymbol{z}} \times \nabla_{\boldsymbol{R}} \phi(\boldsymbol{R})) \cdot \nabla g = 0.n \tag{2.5.5}$$

Compared to the result from equation (2.4.25), the parallel acceleration term is missing because it is of a different order when applying the gyrokinetic ordering, as $k_z \ll k_\perp$, which reduces the order of the term compared to the $\boldsymbol{E} \times \boldsymbol{B}$ nonlinearity $\frac{v_z \partial_z g_0}{(\hat{\boldsymbol{z}} \times \nabla_{\boldsymbol{R}} \phi(\boldsymbol{R})) \cdot \nabla g} \sim \rho^*$.

2.6 Implementation of 6D kinetic semi-Lagrangian code

2.6.1 Numerical method: backward semi-Lagrange

Computationally the most expensive part in simulating the Vlasov system is the computation of the advection terms. Several numerical methods can and have been used, ranging from finite difference methods [Jenko, 2000] to particle in cell methods [Hatzky et al., 2002]. The finite difference methods are the category of Eulerian methods which utilize a grid to compute the spacial derivatives and updates the distributions function with a given time discretization. Particle in cell methods use virtual particles, so called markers, which represent the distribution function and are advected along the characteristics of the partial differential equation. The fields can be computed by adding up all markers in a given cell (thus the name, particle in cell methods (PIC)) and creating a histogram, which then can be integrated. Both groups of methods have specific difficulties associated with the methods. In Eulerian methods, the length of the time step underlies the Currant, or CFL criterion $\Delta t \propto v_{\max} \Delta x$. This means that the time step is directly proportional to the grid discretization which can to lead to strong restrictions for high resolution simulations. On the other and PIC methods are subject to high levels of noise, as the distribution function is not represented by a continuous function but rather a collection of individual markers.
The methods used for our simulations the backward semi-Lagrangian method. By combining properties of grid based (Eulerian) and particle based (Lagrangian) methods, semi-Lagrangian methods eliminate the two main problems of the two groups. On the one side, the distribution function is defined as a continuous function on a

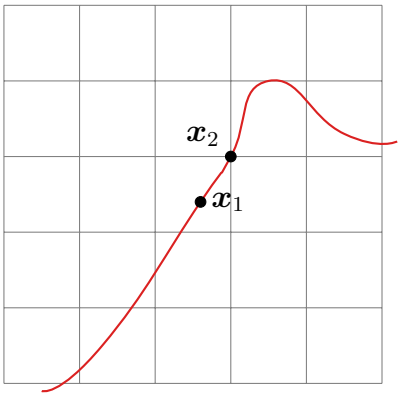

Figure 2.8: Illustration of particle trajectory of particle on grid with position $\boldsymbol{x}$ at time t

grid, which makes the solution less subject to noise, while still solving the characteristic equations, instead of directly computing the partial derivatives on the grid which avoids the problem of strict CFL criteria for the advection. In every time step, the new value of every grid point is determined by following the trajectory of a particle sitting at the grid point back in time. The distribution function is constant along the characteristics (compare discussion in section 2.2), thus, the value at the particle position $\boldsymbol{x}_2$ at time t_2 is the same as the at the particle position $\boldsymbol{x}_1$ at time $t_1 = t_2 - \Delta t$ when following the trajectory of a particle (illustrated in figure 2.8). The traced back position of the particle usually does not lay on a grid point and the value of the distribution function is unknown. After the characteristic is solved and the position is known, the distribution function is computed via interpolation.

2.6.2 Solution to characteristic equations

The equation of motion for the plasma in dimensionless form

$$\partial_t f + \boldsymbol{v} \cdot \nabla f + [\boldsymbol{E} + (\boldsymbol{v} \times \hat{\boldsymbol{z}})] \cdot \nabla_v f = 0. \tag{2.6.1}$$

The characteristic equations of the Vlasov system are the following [Sonnendrücker et al., 1999]

$$\frac{\mathrm{d}\boldsymbol{X}}{\mathrm{d}t} = \boldsymbol{V}, \quad \frac{\mathrm{d}\boldsymbol{V}}{\mathrm{d}t} = \boldsymbol{E}(\boldsymbol{X}, t) + \boldsymbol{V} \times \hat{\boldsymbol{z}}, \tag{2.6.2}$$

where $\boldsymbol{X}(t; \boldsymbol{x}, \boldsymbol{v}, t_0)$ and $\boldsymbol{V}(t; \boldsymbol{x}, \boldsymbol{v}, t_0)$ denote the solutions of the characteristic equations at the time t with the initial condition $\boldsymbol{X}(t_0) = \boldsymbol{x}$ and $\boldsymbol{V}(t_0) = \boldsymbol{v}$. Given the initial condition f_0 at the time t_0, the solution at the time $t > 0$ is given by

$$f(\boldsymbol{x}, \boldsymbol{v}, t) = f_0 \left(\boldsymbol{X}(t_0; \boldsymbol{x}, \boldsymbol{v}, t), \boldsymbol{V}(t_0; \boldsymbol{x}, \boldsymbol{v}, t) \right). \tag{2.6.3}$$

The characteristic equation for the velocity advection consists of two parts, the electric field advection and the magnetic field advection. For all cases, it is assumed that the magnetic field is constant and unidirectional and thus, can be written as $\boldsymbol{B} = B_0\hat{\boldsymbol{z}}$. The idea of moving velocity grid for the Vlasov equation [Sonnendrücker et al., 2004] was applied to a rotating velocity grid [Kormann et al., 2019]. The logical rotating grid is defined such that $\boldsymbol{v} = D(t)\boldsymbol{w}$, where $D(t)$ is the 2D rotation matrix in the x-y-plain

$$D(t) = \begin{pmatrix} \cos(B_0(t-t_0)) & \sin(B_0(t-t_0)) & 0 \\ -\sin(B_0(t-t_0)) & \cos(B_0(t-t_0)) & 0 \\ 0 & 0 & 1 \end{pmatrix}, \tag{2.6.4}$$

which follow the fast oscillating motion of the ions with the Larmor frequency ω_c. The distribution function is defined on the logical grid $g(t, \boldsymbol{x}, \boldsymbol{w}) = f(t, \boldsymbol{x}, D(t)\boldsymbol{v})$.

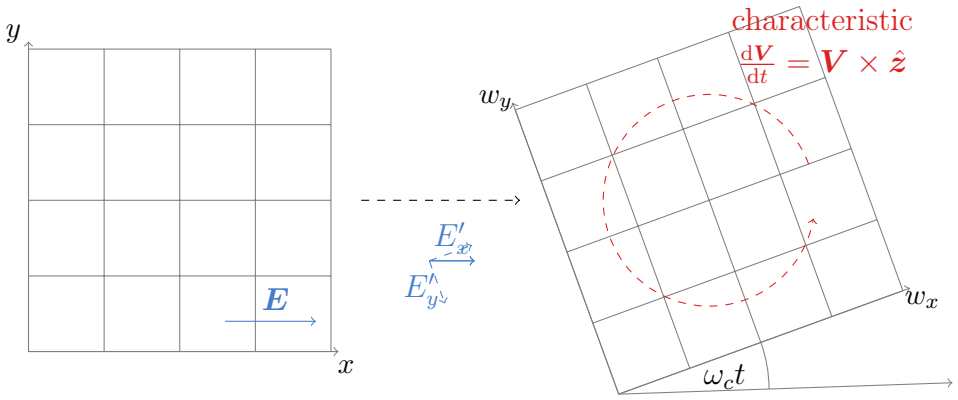

Figure 2.9: Illustration of the transformation of the electric field $\boldsymbol{E}$ into the coordinate system of the rotating grid

For the advection, the velocity is transformed back into physical coordinates and the characteristic is solved. The solutions of the two characteristic equations are

$$\boldsymbol{X}(t; t_0, \boldsymbol{x}, \boldsymbol{v}) = \boldsymbol{x} + (t - t_0)\boldsymbol{v} \tag{2.6.5}$$
$$\boldsymbol{V}(t; t_0, \boldsymbol{x}, \boldsymbol{v}) = D(t)\boldsymbol{v} + A(t)\boldsymbol{E}(t, \boldsymbol{x}), \tag{2.6.6}$$

with

$$A(t) = \frac{1}{B_0}\begin{pmatrix} \sin(B_0(t-t_0)) & 1-\cos(B_0(t-t_0)) & 0 \\ \cos(B_0(t-t_0))-1 & \sin(B_0(t-t_0)) & 0 \\ 0 & 0 & B_0(t-t_0) \end{pmatrix}. \tag{2.6.7}$$

The electric field $\boldsymbol{E}$ is computed on the physical grid. For the computation of the velocity advection, it needs to be transformed into the rotating frame $\boldsymbol{E}'$ (compare 2.9). As we want to compute the distribution function at time t^{m+1}, we need to solve the characteristic with origin at t^m resulting in $V(t^{m+1}; \boldsymbol{x}, \boldsymbol{v}, t^m) = D(t^m -$

$t^{m+1})\boldsymbol{v} + A(t^m - t^{m+1})\boldsymbol{E}$. To compute g^{m+1} at the point $\boldsymbol{w}$ on the logical grid, the distribution function is transformed the back to the physical grid and the the update is performed. One has to be careful that the rotation of the grid is different at time t^m and t^{m+1}, namely

$$g^m(\boldsymbol{x}, \boldsymbol{w}) = f^m(\boldsymbol{x}, D(t^m)\boldsymbol{v}) \tag{2.6.8}$$
$$g^{m+1}(\boldsymbol{x}, \boldsymbol{w}) = f^{m+1}(\boldsymbol{x}, D(t^{m+1})\boldsymbol{v}). \tag{2.6.9}$$

Thus, we can write the update relation for the velocity advection of the distribution function g^{m+1} at time t_{m+1}. We can use some properties of rotation matrices for the simplifications $D(t)^{-1} = D(-t)$ and $D(t+s) = D(t)D(s)$, resulting in

$$\begin{aligned} g^{m+1}(\boldsymbol{x}, \boldsymbol{w}) &= g^m \left(\boldsymbol{x}, D(-t^m) \underbrace{\left[D(t^m - t^{m+1}) D(t^{m+1}) \boldsymbol{w} + A(t^m - t^{m-1}) \boldsymbol{E} \right]}_{V(t^{m+1}; \boldsymbol{x}, \boldsymbol{v}, t^m,)} \right) \\ &= g^m \left(\boldsymbol{x}, \boldsymbol{w} + D(-t^m) A(\Delta t) \boldsymbol{E} \right). \end{aligned} \tag{2.6.10}$$

The update relation of the distribution function for the configuration space advection is

$$g^{m+1}(\boldsymbol{x}, \boldsymbol{w}) = g^m(\boldsymbol{x} - \Delta t D(t^m)\boldsymbol{w}, \boldsymbol{w}). \tag{2.6.11}$$

The advantage of the introduction of the rotating logical grid is that the advection coefficients are constant during the advection, i.e. the electric field does not change during the velocity advection and the advection in a particular direction is independent of the coordinate itself. This allows us to split the interpolation consecutively performed 1D interpolations

$$g^{m+1}(\xi_i) = g^m(\xi_i + \alpha), \quad i = 1, 2, ...6, \tag{2.6.12}$$

with $\xi = (\boldsymbol{x}, \boldsymbol{w})$. Splitting the interpolation in a series of 1D advections avoids the immense cost of performing multidimensional interpolations.

2.6.3 Interpolation method

The method used for interpolation depends on multiple factors which need to be balanced. The two main factors of interest are in this discussion are interpolation accuracy and computational cost. First, I want to distinguish between two main groups, global and local (also piece-wise) interpolation methods. Global methods, like spline interpolation or trigonometric interpolation, depend on solving a linear system on the entirety of nodes given certain constraints, e.g. a given smoothness at any given point. In most applications, such methods are preferred over piece-wise methods, due to their higher accuracy at a comparable computational cost. Furthermore, these methods are not subject to the problem of Runge's phenomenon,

which leads to oscillations and large deviations at the boundaries of polynomial interpolations stencils.
Due to the memory intensity of high dimensional problems, it is not possible to store the entire distribution function on a single computational unit. The problem of distributing data over multiple units is discussed in the following section. In the case of a global interpolation method, all data in one direction needs to be on the same computing unit. When an interpolation is computed in a different direction, the entire data needs to be redistributed among the computing units, which is very costly. The communication intensity makes the use of global interpolation methods impractical in our scenario. Thus, the method of choice of interpolations of distributed domains is a local method, where only a small subset of the nodes in one direction are used to compute the interpolation. Typically, a polynomial of order $n+1$ is used to compute the interpolation on a stencil of n nodes. To avoid the large oscillations that occur at the edge of the interpolation stencil, the location of the stencil is chosen such that the point which should be computed close to the center of the stencil.
The strategy of shifting a distribution function by a given displacement α, as described in the upper section on the semi-Lagrangian method is visualized in Fig. 2.10. First, a grid point x_i is chosen, for which the shift should be computed (marked by the dashed line in Fig. 2.10(a)) and the displacement α by which the function should be shifted. In the next step, an interpolation polynomial is computed based on the values on the neighboring nodes (compare Fig. 2.10(b)). In our example, a 5th-order $f_l(x)$ polynomial is used. The value $f_l(x_0 + \alpha)$ will become the updated value for the function at grid point x_0. After the value is updated, the same is repeated for every grid point in the dimension, until the entire function is shifted. Lagrange polynomials are used to construct the interpolating polynomial.

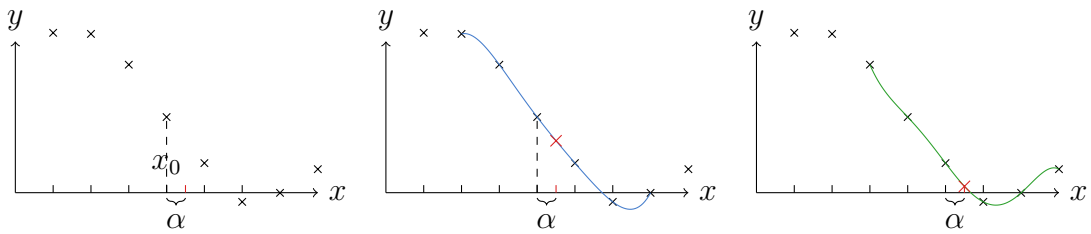

Figure 2.10: Illustration of interpolation step with Lagrange polynomial

Lagrange interpolation

Lagrange interpolation was first formulated by Edward Waring in 1779 [Waring, 1779]. Given a set of discrete data (x_m, y_m), it is a method to generate a polynomial $(L(x))$ of degree k, which passes through $k+1$-nodes at $L(x_m) = y_m$. The interpolating polynomial of degree k with $k+1$ data points is uniquely defined. The

construction of the polynomial is achieved by constructing a base of $k+1$ polynomials $l_i(x)$ of which each takes the values one at exactly one node and zero at all the other nodes $l_i(x_m) = \delta_{j,m}$. The base polynomials can be written in explicit form

$$l_i(x) = \frac{x - x_0}{x_i - x_0} \cdots \frac{x - x_{i-1}}{x_i - x_{i-1}} \frac{x - x_{i+1}}{x_i - x_{i+1}} \cdots \frac{x - x_k}{x_i - x_k} = \prod_{\substack{0<j<k \\ i \neq j}} \frac{x - x_j}{x_i - x_j}. \tag{2.6.13}$$

The interpolating function is then given by the linear combination of the basis polynomials with the coefficients y_i

$$L(x) = \sum_{i=0}^{k} l_i(x) y_i. \tag{2.6.14}$$

To illustrate the construction of a Lagrangian interpolation polynomial, I have plotted the interpolation of the function $f(x) = \sin(2x)$ (black dashed line) with polynomial of order $k = 5$ (solid red line) in figure 2.11. Additionally, I have added the individual base polynomials multiplied with their respective coefficient $y_i l_i(x)$. The plot shows clearly, that all polynomials takes the value of the function at exactly one point $y_m = y_m l_m(x_m)$ and is zero at all other nodes.

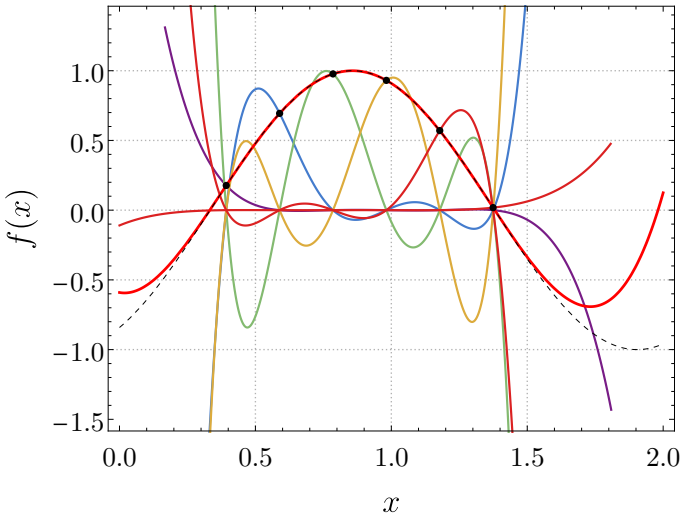

Figure 2.11: Construction of Lagrange polynomial interpolating a sin-function

Interpolation accuracy After understanding the principle of the interpolation, the accuracy is investigated, especially with respect to displacement and order of the interpolating polynomial, by analyzing the reproduction of Fourier modes. In the first step, we are looking into the interpolation accuracy of various Fourier modes depending on the position of interpolation (i.e. the displacement normalized to the distance between the interpolation nodes). Figure 2.12 shows the relative interpolation error ϵ as a function of the displacement for various Fourier modes (with

increasing wavelength from red to blue). When the relative error is $0 \leq \epsilon < 1$, the interpolated Fourier mode is damped, thus is stable. For $\epsilon > 1$, the Fourier mode is numerically unstable. If a numerical method excites certain modes, this leads to numerical instabilities and spurious, nonphysical modes that pollute the simulation. It is very difficult to later separate which modes are physical and which are not. Thus, it is important to design a numerical scheme that does not excite spurious modes. Each plot in the figure is a different order of interpolation from $k = 1$ on the left to $k = 3$ on the right. The first noticeable attribute is, that each interpolation polynomial has at least $k + 1$ points where the function is reproduced exactly.

From the interpolation error can be deduced, that in order to have a numerically

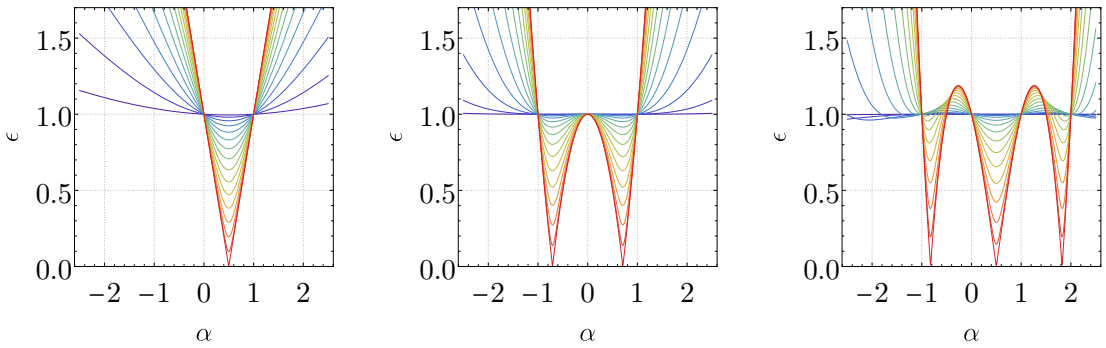

(a) $k = 1$ (b) $k = 2$ (c) $k = 3$

Figure 2.12: Interpolation error for in various Fourier modes depending on the displacement (normalized to the node distance) for different interpolation order from $k = 1$ (left) to $k = 4$ (right)

stable system, the interpolation stencil must be chosen, such that the interpolated position lays in the center of the stencil. One has to be careful that the center, for odd-ordered polynomials is within the inner cell, and for even orders, the two cells are left and right of the center node. For an even interpolation order, the stencil has to be chosen differently depending on the direction of the displacement. The fact that the stencil is chosen depending on the direction of the advection is similar to an up-wind scheme in finite differences, however, here comes the big advantages of semi-Lagrangian schemes over finite difference schemes. For a fixed stencil (on a fixed set of points), the method has the same CFL condition as a standard finite difference scheme. In fact, such a semi-Lagrange scheme with Lagrange interpolation can be rewritten in the form of a finite difference scheme. However, the CFL criterion can be circumvented, if the stencil is shifted accordingly, when the shift is larger than one cell.

After getting a qualitative overview of the numeric error and the stability properties of the Lagrange interpolation, we want to take a closer look at the damping rate of Fourier modes for different interpolation orders. The interpolation error of each Fourier mode is computed at the middle point between the two center nodes $\alpha = \frac{\Delta x}{2}$. In figure 2.13 shows the relative error for different wavenumbers. For the x-axis, I

have chosen 'nodes per wave length' as a quantity, as this ultimately determines the quality of the interpolation. E.g. in a box with length $d = 2\pi$ and $N = 32$ points. The longest wave, fitting in the box, with wavenumber $k = 1$ has 32 points per wavelength, whereas the second harmonic has 16 nodes per wavelength.

The graph in figure 2.13 is important to consider when investigating instabilities

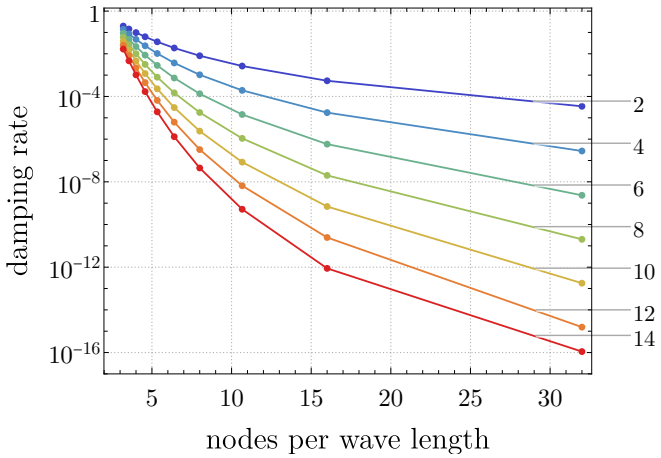

Figure 2.13: Damping rate of various Fourier modes for different interpolation orders from $k = 2$ (blue) to $k = 16$ (red)

with semi-Lagrangian codes, especially when investigating the behavior of growth rates over a range of different wavenumbers. As soon as the relative error gets to a similar order as the growth rate of the instability of interest, the results can not be trusted anymore. It shows that, especially for small interpolation orders, the quality of the interpolation can deteriorate very quickly.

For the calculation that has produced figure 2.13 as fixed shift has been used. However, when computing an advection step in our code, the distribution function is interpolated with a different shift for every velocity or electric field. In case we want to estimate the damping of a density perturbation, an advection step needs to be considered. The plots in figure 2.12 show that error varies greatly with the size of the shift α. We are focusing on the velocity advection, as the electric field is usually (especially in linear scenarios) much smaller. A Fourier mode in position spaced is combined with a Maxwell distribution $f(v) = \frac{e^{-\frac{v^2}{2}}}{\sqrt{(2\pi)}}$. Every point is advected by one time step Δt and the amplitude of the Fourier mode is computed. The shift now depends on the position in velocity space $\alpha = v\Delta t$. The change in the amplitude gives us an estimate for the effective damping rate of the advection step. This test relies on the spatial and velocity space resolution as well as the time step Δt. The results are presented as a function of the spatial resolution, as 'nodes per wavelength'. For the velocity grid, a typical grid with maximum velocity $v_{\max} = 4$ and $N = 32$ points is used. The time step is chosen as $\Delta t = 0.008$, such that the dimension less quantity $\frac{\Delta t v_{\max}}{\Delta x} \approx 0.16$.

As expected, the interpolation accuracy increases when a mode is represented with

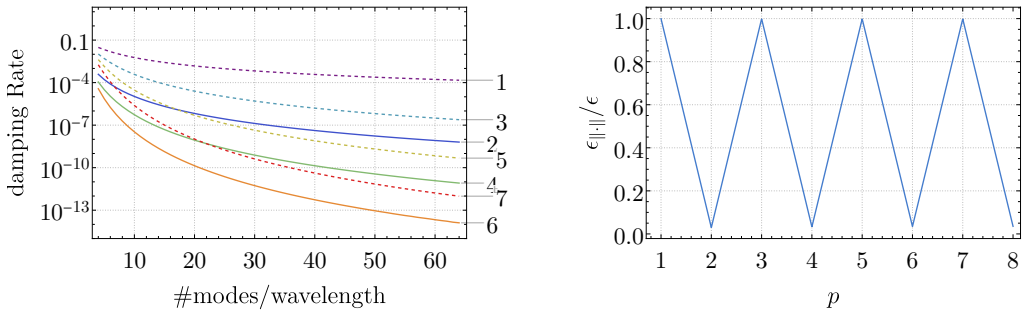

(a) (b)

Figure 2.14: Effective damping rate in velocity advection step as a function of the resolution for various orders (a) and ratio of amplitude error $\epsilon_{||\cdot||}$ and total error ϵ

more nodes per wavelength. We can see, that especially for lower orders, the damping rate is quite significant for badly resolved modes. Especially for odd orders $k = 1$ or $k = 3$, more than 16 points per wavelength are need to achieve a damping rate below 10^{-4}.

It is interesting that the damping rate is qualitatively different between the even and odd orders of interpolation. It is not directly apparent, why an interpolation with four points ($k = 3$) can perform worse than an interpolation with three ($k = 2$) points. For such a Von-Neumann type analysis [Charney et al., 1950], the absolute value of our interpolated Fourier modes $|\hat{a}_i|$ is compared to the expected amplitude $\hat{a}$. Calculating the error from the absolute values, gives insights whether a mode is growing ($|\hat{a}_i|/|\hat{a}| > 1$) or damped ($|\hat{a}_i|/|\hat{a}| < 1$). However, it does not reveal any information about the error in the phase of the complex mode, which is caused by the interpolation. To illustrate the difference between an error in the amplitude and the phase, the total error $\epsilon = \frac{|\hat{a}_i - \hat{a}|}{|\hat{a}|}$ and the amplitude error $\epsilon_{|\cdot|} = \left|\frac{|\hat{a}| - |\hat{a}_i|}{|\hat{a}|}\right|$ have been computed and the ratio for various interpolation orders has been plotted (compare figure 2.12(b)). The results show, what the fraction of the whole error is that originates in the amplitude error. It clearly shows, that for odd orders almost the entire error is in the amplitude of the mode, where for even numbers the error mostly consists of an error in the phase, which explains the result before, when testing for the damping rate of the different orders, that even interpolation orders perform significantly better.

This qualitative difference between even and odd interpolation order is important to keep in mind when designing a numerical method based on interpolation and one might need to choose the order accordingly depending on the importance of certain quantities. If the focus lies on determining growth rates, even orders might be preferred. In contrast, when the frequencies are more important, odd orders might be favored.

2.6.4 Implementation details

Time integration

Within one time step, the distribution function has to be shifted in all six dimensions. Computing these shift with a six-dimensional interpolation would be impractically expensive. Instead, the $\boldsymbol{r}$ and $\boldsymbol{v}$ advection can be split using the Lie splitting, because the electric field does not change during the velocity advection step resulting in an update from the distribution function at time step n to the time $n+1$ in two stages

$$(1) \qquad f^*(\boldsymbol{r},\boldsymbol{v}) = f^n(\boldsymbol{r} - \Delta t\boldsymbol{v},\boldsymbol{v}), \tag{2.6.15}$$

$$(2) \qquad f^{m+1}(\boldsymbol{r},\boldsymbol{v}) = f^*(\boldsymbol{r},\boldsymbol{v} - \Delta t\boldsymbol{E}). \tag{2.6.16}$$

As the interpolations for the directions are independent of each other, they can be executed in successive 1D interpolations. A splitting of the individual interpolations does not introduce an additional error, as the advection operators compute [McLachlan and Quispel, 2002]. The resulting scheme is first order in time [Cheng and Knorr, 1976], however, the time integration scheme can be modified by splitting the electric field advection into two half steps (Strang splitting)

$$(1) \qquad f^*(\boldsymbol{r},\boldsymbol{v}) = f^n(\boldsymbol{r},\boldsymbol{v} - \frac{\Delta t}{2}\boldsymbol{E}), \tag{2.6.17}$$

$$(2) \qquad f^{**}(\boldsymbol{r},\boldsymbol{v}) = f^*(\boldsymbol{r} - \Delta t + \boldsymbol{v},\boldsymbol{v}), \tag{2.6.18}$$

$$(3) \qquad f^{m+1}(\boldsymbol{r},\boldsymbol{v}) = f^{**}(\boldsymbol{r},\boldsymbol{v} - \frac{\Delta t}{2}\boldsymbol{E}), \tag{2.6.19}$$

resulting in a second order update scheme. The change comes at no cost, as the third step of the nth time step can be combined with the first step of the $n+1$th time step.

Parallelization by domain decomposition

High-dimensional simulations are computationally very expensive and require a lot of memory. In a small test scenario on a grid with 32 nodes in every direction, the distribution function requires $\sim$ 8.6GB of memory. In the case of a $64 \times 64 \times 64 \times 32 \times 32 \times 32$-simulation, the memory required for the distribution function is already $\sim$ 68.7GB. It is impractical to perform such simulations on a single processor. Thus, distributed memory parallelization is necessary. There are multiple ways to distribute the computational domain to multiple processing units and depending on the numerical scheme, they come with certain advantages and disadvantages. The main limiting factor for the distribution is the slow communication speed between different nodes in an HPC system. In the example of the A3-Skylake partition of the Marconi supercomputer at the Cineca HPC facility (main HPC unit used for simulations in this work), the inter-node communication has a bandwidth of 100Gbit/s, which is an order of magnitude smaller than the memory bandwidth of a single CPU which peaks at $\sim$ 960Gbit/s.

In section 2.6.3, I have described the difference between global and local (piece-wise) interpolation methods. The former requires that at the time of the interpolation, the data of all grid points in the direction of interest have to be located on the same processing unit, which is achieved by a transposition method [Coulaud et al., 1999]. The interpolations are performed consecutively after each other for the different directions. Before each interpolation step, the memory needs to be redistributed between the nodes. For high dimensional problems, a method where a all-to-all communication between the nodes is necessary is unfavorable, because for every interpolation in every time step, almost all data needs to be exchanged.
Another method of distributing is called domain decomposition which divides the 6D hyper-rectangular into smaller sections by dissecting one or multiple dimensions. The subdomains are distributed to different computational units [Crouseilles et al., 2009]. When using a piece-wise interpolation method, the communication is reduced to so-called halo regions which are illustrated in figure 2.15. We are considering an advection in x-direction on the subdomain (A). In the center of the subdomain, the interpolation can be performed locally, however, closer to the boundaries of the domain, information from neighboring domains is needed. Under the assumption that the displacement α is smaller than the step size $\frac{\alpha}{\Delta x} < 1$, a halo region with the width $w_{\text{Halo}} = \left\lfloor \frac{k+1}{2} \right\rfloor$ needs to be sent from domain (D) for the upper boundary. On the lower boundary, the information needs to be sent from the neighboring domain on the left. In case of periodic boundary conditions, the information is sent from the processing unit at the other end. An illustration is shown in figure 2.15, where the information from the right border of domain (D) is the information needed for the halo region (A.1).
In total, the amount of data sent, when interpolating in direction j, sums up to $2n_{\text{proc},j} \times w_{\text{Halo}} \times \prod_{\substack{1 \le i \le 6 \\ i \neq j}} N_i$, where $n_{\text{proc},j}$ is the number of sub-domains in j-direction and N_i is the number of grid points in the direction i. For the simplified case of $N_1 = N_2 = \cdots = N_6$, one can see that the data which needs to be transferred scales with $\propto N^5$. The lower order in scaling compared to the remapping method, where the amount of data sent is $\propto N^6$. In addition to the less amount of data which needs to be exchanged.
In the implementation, the subdomains are distributed to different MPI processes which are equally arranged in a 6D grid, such that every MPI process can communicate with its direct neighbors. Within one MPI process the computation is parallelized with shared memory parallelization using openMP.
In case of the field solver, a Fourier method is used to solve the Poisson equation and to compute the electric field from the electrostatic potential. The data is transposed such that all data in one direction is available on a single processing unit before the FFT is performed. As the transposition is only performed on three-dimensional quantities, such as the density and the electric fields, the communication effort is negligible compared to the communication during the advection step.

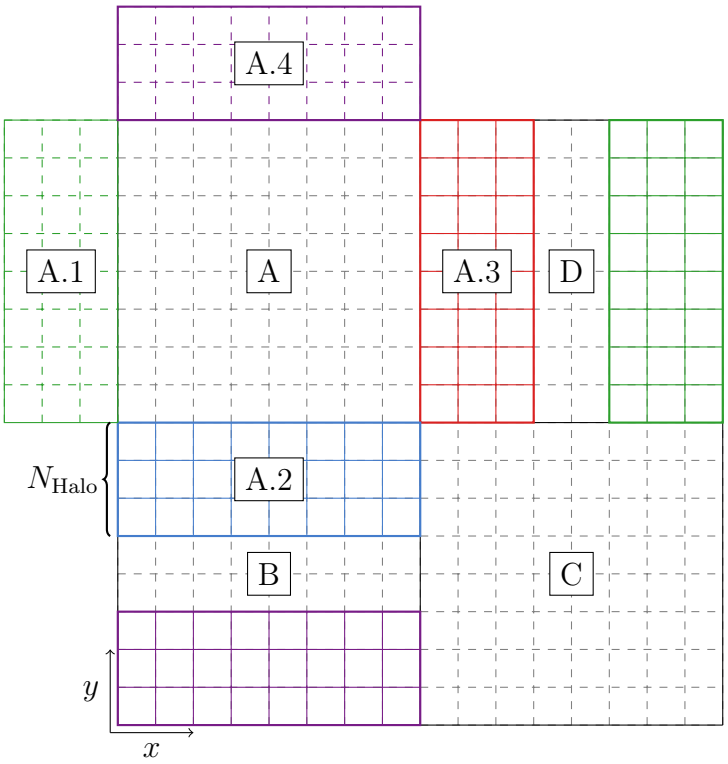

Figure 2.15: Illustration of domain decomposition with halo area in the for a 2D grid

Chapter 3

Simulations of ion temperature gradient (ITG) instabilities

The results of this chapter are partly published in [Raeth et al., 2023] and were presented in the DPG spring meeting 2021 with a poster [Raeth et al., 2021].

As a first physical simulation, 6D kinetic slab ion temperature gradient (ITG) simulation have been performed. The code can be verified by testing the frequency and growth rate of the various modes in the system by computing the dispersion relation. Furthermore, the instability can correctly be described by gyrokinetics, hence, equivalent simulations can be performed with a gyrokinetic code (in our case CGYRO by the team of Candy et al. [Candy et al., 2016]) and the nonlinear saturation can be compared. Similar simulations have already performed by the group of Parker et al. [Sturdevant et al., 2016, Sturdevant et al., 2017], with the major difference, that they assumed a fixed mode number in z-direction and thus, effectively reducing the dimensionality to a 5D system. Whereas in our simulations, the full 6D model is solved and all modes in z-direction, that can be resolved by the given resolution, are included.
In order to perform simulation with such an instability, a local representation of the temperature gradient is used. We assume that a background distribution function f_0 exists, which fulfills

$$\boldsymbol{v} \cdot f_0 + \boldsymbol{v} \times \boldsymbol{B}_0 \cdot \nabla_v = 0, \tag{3.0.1}$$

where $\boldsymbol{B}_0 = \hat{\boldsymbol{z}}$ is the uniform background magnetic field. This condition can be ensured by mandating that the background distribution is parameterized by an arbitrary function g with $f_0(\boldsymbol{r}, \boldsymbol{v}) = f_0(\boldsymbol{R} + \boldsymbol{\rho}, \boldsymbol{v}) = g(\boldsymbol{R}, \boldsymbol{v}) + \boldsymbol{v} \times \hat{\boldsymbol{z}}, v_\perp, v_z)$ (with $v_z = \boldsymbol{v} \cdot \hat{\boldsymbol{z}}$, $v_\perp = |\boldsymbol{v} \times \hat{\boldsymbol{z}}|$ and and $\boldsymbol{R} = \boldsymbol{r} - \boldsymbol{\rho} = \boldsymbol{r} + \boldsymbol{v} \times \hat{\boldsymbol{z}}$ is the the location of the gyrocenter of a given particle, where $\boldsymbol{r}$ is the configurations space coordinate and $\boldsymbol{\rho}$ is the Larmor radius vector). The background distribution is chosen to resemble a

Maxwellian with varying temperature $T(\boldsymbol{R})$, and thus reads

$$g_0(\boldsymbol{R}, v_\perp, v_z) := \left(\frac{1}{2\pi T(\boldsymbol{R})}\right)^{\frac{3}{2}} \exp\left(-\frac{[v_\perp^2 + v_z^2]}{2T(\boldsymbol{R})}\right). \tag{3.0.2}$$

When splitting the distribution function in the Vlasov equation into a perturbation $\delta f = f - g_0$ and the background g_0, one obtains

$$\partial_t \delta f + \boldsymbol{v} \cdot \nabla \delta f + [-\nabla\phi + (\boldsymbol{v} \times \hat{\boldsymbol{z}})] \cdot \nabla_v \delta f = \nabla\phi \cdot \nabla_v g_0. \tag{3.0.3}$$

The additional right hand side, compared to the full-f version, can be computed according to equation 2.3.30

$$\begin{aligned} \nabla_v g_0 &= \hat{\boldsymbol{z}} \times \nabla g_0 + \nabla_v g_0 =: \boldsymbol{v}^* g_0 + \nabla_v g_0 \\ &= -g_0 \hat{\boldsymbol{z}} \times \left(\frac{\nabla T}{T} \frac{3 - (v_\perp^2 + v_z^2)}{2}\right) + \nabla_v g_0. \end{aligned} \tag{3.0.4}$$

The limit that the gradient length is infinite $T(\boldsymbol{R}) \to T = 1$ is taken, in consequence, the background distribution is independent of $\boldsymbol{R}$. Thus, g_0 is replaced with the homogeneous Maxwellian distribution $f_M = \frac{1}{(2\pi)^{\frac{3}{2}}} e^{-\frac{v^2}{2}}$.
For a constant electrostatic potential ϕ, the kinetic equation has the solution $f = e^{-\phi} f_M \approx (1 - \phi) f_M$ (adiabatic response). For the purpose of analytical simplicity the distribution is separated into its adiabatic and non-adiabatic $h = \delta f + \phi f_M$ contribution. Together with the quasi-neutrality condition formulated in section 2.3.4, the full system is

$$\partial_t h + \boldsymbol{v} \cdot \nabla h + (-\nabla\phi + \boldsymbol{v} \times \hat{\boldsymbol{z}}) \cdot \nabla_v h = (\boldsymbol{v}^* \cdot \nabla\phi + \partial_t \phi)\, f_M, \tag{3.0.5}$$

$$\phi = \delta n, \qquad \delta n = \int h \mathrm{d}^3 v. \tag{3.0.6}$$

The electron temperature has been chosen to be the same as the ion temperature $T_e = T = 1$.

3.1 Dispersion relation of ITG instability

Derivation of dispersion relation

The density response of the plasma given a fixed electrostatic potential and a given background gradients is computed. As a starting point is the general solution of the distribution function response which has been derived in (2.3.29)

$$h_k = i(\omega f_M - \boldsymbol{k} \cdot \nabla_{\boldsymbol{v}} S - \boldsymbol{k} \cdot \boldsymbol{v} f_M)\phi_k \sum_{m,p \in \mathbb{Z}} \frac{J_m(k_\perp v_\perp) J_p(k_\perp v_\perp) e^{i(p-m)\alpha}}{\omega - k_z v_z - p}. \tag{3.1.1}$$

The derivative of thermal distribution (3.0.4) is introduced into the ansatz for the response. The two terms $\boldsymbol{k}\cdot\boldsymbol{v}f_M$ and $\boldsymbol{k}\cdot\nabla_{\boldsymbol{v}}g_0$ cancel and new ansatz for the distribution function reads

$$h_k = i\phi_k(\omega-\boldsymbol{v}^*)f_M\sum_{m,p\in\mathbb{Z}}\frac{J_m(k_\perp v_\perp)J_p(k_\perp v_\perp)e^{i(p-m)\alpha}}{\omega-k_z v_z-p}, \tag{3.1.2}$$

where $\boldsymbol{v}^* = \hat{\boldsymbol{z}}\times\frac{\nabla T}{T}\left(\frac{(v_\perp^2+v_z^2)}{2}-\frac{3}{2}\right)$. The density response has been computed and inserted in the equation of the electrostatic potential. The density is obtained by computing the velocity integral of the distribution function

$$\begin{aligned} n_k^h &= \int h_k \mathrm{d}^3v \\ &= \int_{-\infty}^{\infty}\int_0^{\infty}\int_0^{2\pi} i(\omega-\boldsymbol{k}\cdot\boldsymbol{v}^*)\phi_k f_M\sum_{m,p\in\mathbb{Z}}\frac{J_m(k_\perp v_\perp)J_p(k_\perp v_\perp)e^{i(p-m)\alpha}}{k_z v_z-\omega-p}v_\perp \mathrm{d}\alpha\mathrm{d}v_\perp\mathrm{d}v_z. \end{aligned} \tag{3.1.3}$$

The additional label h on the density n_k^h is chosen to highlight the fact that n_k^h is the non-adiabatic density perturbation, which becomes important when the dispersion relation is computed from the density response. Evaluating the α integral reduces the double sum $\int\exp(i(p-m)\alpha)\mathrm{d}\alpha = 2\pi\delta_{p,m}$, resulting in

$$n_k^h = 2\pi\phi_k i\int_{-\infty}^{\infty}\int_0^{\infty}\sum_{p\in\mathbb{Z}}(\omega-\boldsymbol{k}\cdot\boldsymbol{v}^*)f_M\frac{J_p(k_\perp v_\perp)^2}{\omega-k_z v_z-p}v_\perp\mathrm{d}v_\perp\mathrm{d}v_z. \tag{3.1.4}$$

The gradient term $\boldsymbol{v}^*$ complicates the velocity integration because of the additional $|v|^2$ factor. However, the source term can be rewritten using a trick to eliminate the dependency of v. Introducing a helping variable in the Maxwellian background distribution $f_M(v_\perp,v_z)\to f_M(\sqrt{\xi}v_\perp,\sqrt{\xi}v_z)$ allows to compute the derivative with respect to ξ which retrieves the v^2 prefactor $\partial_\xi f_M(\sqrt{\xi}v_\perp,\sqrt{\xi}v_z) = -\frac{v^2}{2}f_M(\sqrt{\xi}v_\perp,\sqrt{\xi}v_z)$. The entire source term can be rewritten in terms of derivatives of ξ

$$\boldsymbol{v}^* = -f_M\hat{\boldsymbol{z}}\times\left(\frac{\nabla T}{T}\frac{3-(v_\perp^2+v_z^2)}{2}\right) = \hat{\boldsymbol{z}}\times\frac{\nabla T}{T}\partial_\xi\left(\xi^{\frac{3}{2}}f_M(\sqrt{\xi}v_\perp,\sqrt{\xi}v_z)\right). \tag{3.1.5}$$

Rewriting the source term allows to remove the source term from the integral and continue the integration. After the integration, the derivative can be computed and the result is evaluated for $\xi=1$. The perpendicular velocity integral results in

$$\int_0^{\infty}e^{-\frac{\xi v_\perp^2}{2}}J_p(k_\perp v_\perp)^2 v_\perp\mathrm{d}v_\perp = \frac{1}{\xi}e^{-\frac{k_\perp^2}{\xi}}I_p\left(\frac{k_\perp^2}{\xi}\right), \tag{3.1.6}$$

where $I_p(x)$ is the modified Bessel function of first kind. The parallel integral is evaluated using the plasma dispersion function $Z(x) = \frac{1}{\sqrt{(\pi)}} \int_{-\infty}^{\infty} \frac{e^{-t^2}}{(t-x)^2} \mathrm{d}t$

$$\int_{-\infty}^{\infty} \frac{e^{-\frac{\xi v_z^2}{2}}}{\omega - v_z k_z - p} \mathrm{d}v_z = \frac{\sqrt{\pi}}{|k_z|} Z\left(\frac{\omega - p}{|k_z|}\sqrt{\frac{\xi}{2}}\right). \tag{3.1.7}$$

When these two integrals are computed, the density response reads

$$n_k^h = \phi_k \left[\omega - k_y \frac{\nabla T}{T} \partial_\xi\right] \frac{1}{|k_z|}\sqrt{\frac{\xi}{2}} e^{-\frac{k_\perp^2}{\xi}} \sum_{p\in\mathbb{Z}} Z\left(\frac{\omega + p}{|k_z|}\sqrt{\frac{\xi}{2}}\right) I_p\left(\frac{k_\perp^2}{\xi}\right), \tag{3.1.8}$$

where $Z(\chi)$ is the plasma dispersion function

$$Z(\zeta) = e^{-\zeta^2}\left(i\sqrt{\pi} - 2\int_0^\zeta e^{t^2} \mathrm{d}t\right). \tag{3.1.9}$$

The symbol $\Gamma_n(x^2) = e^{-x^2} I_n(x^2)$ [Brambilla, 1998] is used to obtain a shorter expression

$$n_k^h = \phi_k \left[\omega - k_y \frac{\nabla T}{T} \partial_\xi\right] \frac{1}{|k_z|}\sqrt{\frac{\xi}{2}} \sum_{p\in\mathbb{Z}} Z\left(\frac{\omega + p}{|k_z|}\sqrt{\frac{\xi}{2}}\right) \Gamma_n\left(\frac{k_\perp^2}{\xi}\right). \tag{3.1.10}$$

After the density response to an electrostatic potential has been computed, the dispersion relation is assembled. The electro static potential, in case of a system with adiabatic electrons with an infinity high plasma frequency, is given by ($T_e = T_i = 1$)

$$\phi_k = n_k. \tag{3.1.11}$$

Note, the calculated response only contains the non-adiabatic part of the distribution function, while for the computation of the electrostatic potential, the full density response $n_k = n_k^h - \phi_k = \int h_k \mathrm{d}^3 v - \phi_k$ is necessary, which is introduced in the equation for the electrostatic potential 3.1.11 resulting in

$$0 = \frac{1}{\phi_k} \int h_k \mathrm{d}^3 v - 2. \tag{3.1.12}$$

This is equivalent to the formulation in terms of the electric susceptibility $\chi = \chi_i + \chi_e = \frac{1}{\phi_k} \int h_k \mathrm{d}^3 v - 2$ (compare equation (2.3.39)). The resulting dispersion relation

$$0 = \left[\omega - k_y \frac{\nabla T}{T} \partial_\xi\right] \frac{1}{|k_z|}\sqrt{\frac{\xi}{2}} \sum_{p\in\mathbb{Z}} Z\left(\frac{\omega + p}{|k_z|}\sqrt{\frac{\xi}{2}}\right) \Gamma_n\left(\frac{k_\perp^2}{\xi}\right) - 2 \tag{3.1.13}$$

describes for the 6D kinetic system. Every element of the sum describes the contribution of a harmonic on the gyro-orbit. The system can easily be simplified to the gyrokinetic solution by cutting the sum after the 0th harmonic (constant in the velocity). The series converges almost immediately for slow waves $\omega \ll \omega_{ci}$, such as the ITG modes, and the higher order contributions have a negligible contribution to the dispersion relation. However, the full expansion will later be important for the computation of high-frequency waves and energy fluxes, which go beyond the standard gyrokinetic description.
Every solution $(\omega, \boldsymbol{k})$ describes a self-consistent mode present in the system. Most of the modes are damped due to Landau damping and thus, have a negative growth rates. The temperature gradient in the system causes some modes to grow. Solutions (ω, $\boldsymbol{k}$) to the dispersion relation can be found with a standard root-finding algorithm.

Simulation of dispersion relation in 6D kinetic code

As a first numerical test, a plasma is simulated with an ion temperature gradient, similar to the system as described in the system in section 3.1. However, for a more cost-effective simulation and an easier determination of the growth rate and the frequency, linear simulations are performed. In the linearized model, the acceleration term from the electric field on the left-hand side $-\nabla\phi \cdot \nabla_v h$ is neglected, which leads to an indefinitely growing state without any nonlinear saturation effects. The system has been initialized with a random density perturbation. For configuration space, a box with $N_x = 128 \times 128 \times 8$ is chosen. The box size has been selected such that the smallest perpendicular wave number is $k_{\perp,0} = 0.3$ ($L_\perp = \frac{20}{3}\pi$). The parallel length has been determined by the wave number of the fastest growing mode in the system which depends on the temperature gradient and selected by computing growth rates with the dispersion relation beforehand. In the displayed result, a temperature gradient $\frac{\nabla T}{T} = 0.05$ has been used, which leads to an ideal parallel wave number of $k_z = \frac{1}{240}$ and, thus, $L_z = 480\pi$. The velocity space is symmetric for all directions with $v_{\max} = 4$ and $N_v = 32$. The full set of parameters can be found in the appendix B.2.1. After a certain time, a fixed growth rate has been established, and the frequency and growth rate of the various modes have been computed from the Fourier-transformed density perturbation.
A comparison between the analytical dispersion relation (solid lines) and the simulated results (dots) can be found in figure 3.1. The figure on the left side shows the frequency, and on the right side the growth rate. The mode with the wave vector perpendicular to the magnetic field $k_x = 0$ is dominant with a peak growth rate at $k_y \sim 0.9$ with $\gamma \approx 0.0021$. For larger wave numbers, the growth rates level at $\gamma \approx 0.0013$. The frequencies are about a factor 5 larger than the growth rates. The numerical results agree almost perfectly with our predicted dispersion relation. In the range from $k_y = 0.6$ till $k_y = 2.7$ the growth rate has an error of $\sim 0.1\%$, while the deviation of the frequency is $\sim 0.01\%$ (compare table 3.1). The values show a larger discrepancy for smaller wave numbers k_y as the growth rates become small

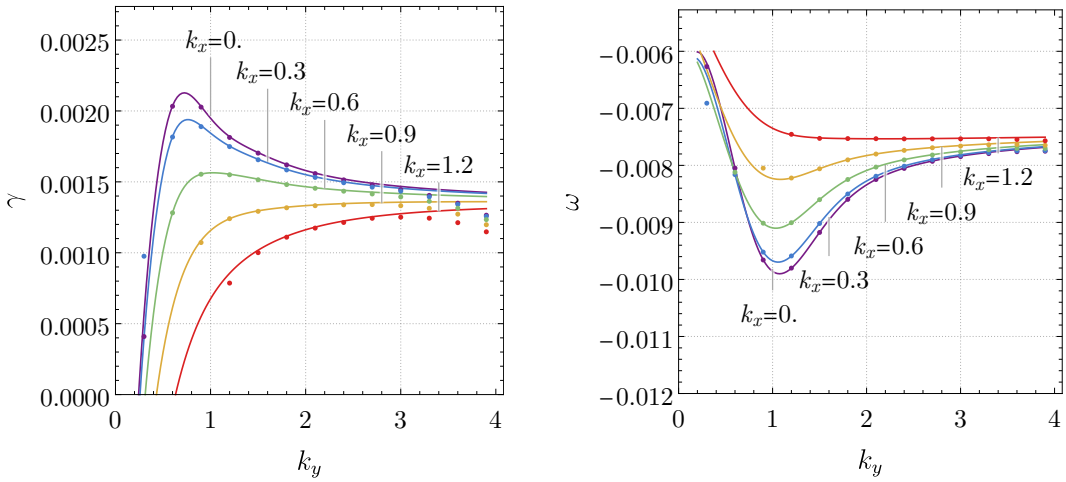

Figure 3.1: Comparison of dispersion relation (line) with growth rates (a) and frequencies (b) determined from simulation with BSL6D (points) for various perpendicular wave vectors (k_x,k_y)

(and partly negative), which makes them difficult to determine with the method which has been used to determine the growth of the modes. For larger wave numbers, the simulation results underestimate the growth rates which is an effect of the numerical diffusion induced by the interpolation method. The accuracy can be improved by a higher interpolation order or a higher resolution, at the expense of higher computational cost. The results give strong confidence that the code reliably produces correct results for linear instabilities.

3.2 Quasi-linear energy fluxes

Another interesting test case for fully kinetic simulation codes, is the study of the quasi-linear fluxes in the system. In comparison to linear fluxes, these energy fluxes do not average to zero when integrated over the entire domain (such as the $\boldsymbol{E}\times\boldsymbol{B}$ particle flux $\int u^{\boldsymbol{E}\times\boldsymbol{B}}\mathrm{d}^3x = \frac{1}{qB^2}\int \boldsymbol{E}\mathrm{d}^3x \times \boldsymbol{B} = 0$). These fluxes are referred to as quasi-linear because they are quadratic in the perturbation amplitude, while being caused by linear modes. In gyrokinetics all energy fluxes described by the $\boldsymbol{E}\times\boldsymbol{B}$ energy flux whereas, the description of the energy fluxes in the 6D kinetic picture is more complicated, where the energy flux consists of multiple contributions. The sum of these contributions result in the $\boldsymbol{E}\times\boldsymbol{B}$ heat flux in the gyrokinetic limit. The change in the kinetic energy obtained by computing the second moment $\int f\frac{v^2}{2}\mathrm{d}^3v$ of the Vlasov equation

$$\partial_t f + \boldsymbol{v}\cdot\nabla f + [-\nabla\phi + (\boldsymbol{v}\times\boldsymbol{B})]\cdot\nabla_v f = 0. \tag{3.2.1}$$

Table 3.1: Comparison of growth rate γ and frequency ω between simulation and analytical results, with respective error ϵ_γ and ϵ_ω in percent

k_y	γ_{ana}	γ_{BSL6D}	$\epsilon_\gamma[\%]$	ω_{BSL6D}	ω_{BSL6D}	$\epsilon_\omega[\%]$
0.3	0.000566	0.000409	38.23	-0.006211	-0.006268	0.906
0.6	0.002036	0.002033	0.162	-0.008050	-0.008049	0.014
0.9	0.002032	0.002027	0.239	-0.009656	-0.009659	0.034
1.2	0.001819	0.001813	0.319	-0.009804	-0.009801	0.028
1.5	0.001706	0.001703	0.213	-0.009175	-0.009176	0.012
1.8	0.001623	0.001620	0.212	-0.008595	-0.008597	0.021
2.1	0.001562	0.001558	0.228	-0.008247	-0.008248	0.012
2.4	0.001520	0.001514	0.380	-0.008049	-0.008054	0.062
2.7	0.001490	0.001479	0.731	-0.007924	-0.007929	0.071
3.0	0.001468	0.001445	1.560	-0.007837	-0.007847	0.135

The result reads

$$2\partial_t \epsilon + 2\nabla \cdot \boldsymbol{Q} + 2\left[\nabla \cdot (\phi \boldsymbol{\Gamma}) + \phi \partial_t n\right]. \tag{3.2.2}$$

In equation 3.2.2, an additional energy flux $\boldsymbol{S} = \phi\boldsymbol{\Gamma}$, the Poynting flux is recognized addition to the energy flux $\boldsymbol{Q} = \frac{1}{2}\int \boldsymbol{v} v^2 f \mathrm{d}^3 v$. The change of the total energy $\partial_t(\epsilon + \frac{n^2}{2})$ can be expressed in terms of these two fluxes

$$\partial_t \epsilon + \phi \partial_t n = -\nabla \cdot \boldsymbol{Q} - \nabla \cdot \boldsymbol{S}. \tag{3.2.3}$$

One has to be careful with the nomenclature of the energy fluxes. The heat flux describes the flow of internal energy in the co-moving reference frame. Meaning that the mean velocity of the fluid is subtracted $\boldsymbol{Q}_{\text{heat}} = \int (\boldsymbol{v} - \boldsymbol{u}) \frac{v^2}{2} f \mathrm{d}^3 v$, where $\boldsymbol{u} = \int \boldsymbol{v} f \mathrm{d}^3 v$. However, this discussion focuses on the energy flux, which is the total transport of internal energy through the domain. The total energy flux should be equal to the $\boldsymbol{E} \times \boldsymbol{B}$ heat flux at least in the gyrokinetic limit which implies that $\boldsymbol{Q}$ must contain a contribution, which balances the Poynting flux and is not part of the gyrokinetic description. To see the different contributions to the energy flux $\boldsymbol{Q}$, the third moment $\int \boldsymbol{v} \frac{v^2}{2} f \mathrm{d}^3 v$ of the Vlasov equation is computed. When an expression for the stress tensor $\boldsymbol{\Pi} = \int \boldsymbol{v}\boldsymbol{v}^T f \mathrm{d}^3 v$ and $\boldsymbol{\Pi}^* = \int \frac{v^2}{2} \boldsymbol{v}\boldsymbol{v}^T f \mathrm{d}^3 v$ is introduced the expression reads

$$\partial_t \boldsymbol{Q} + \nabla \cdot \boldsymbol{\Pi}^* + \boldsymbol{\Pi} \cdot \nabla\phi + \nabla\phi\epsilon - \int (\boldsymbol{v} \times \hat{\boldsymbol{z}}) \frac{v^2}{2} f \mathrm{d}^3 v = 0. \tag{3.2.4}$$

To calculate the perpendicular component of the energy flux, the vector product with the magnetic field and applying the Grassmann identity $-(\boldsymbol{v} \times \hat{\boldsymbol{z}}) \times \hat{\boldsymbol{z}} = \hat{\boldsymbol{z}} \times (\boldsymbol{v} \times \hat{\boldsymbol{z}}) = B^2 \boldsymbol{v} - (\hat{\boldsymbol{z}} \cdot \boldsymbol{v}) \hat{\boldsymbol{z}} = B^2 \boldsymbol{v}_\perp$. The result is an expression for the perpendicular energy

flux

$$B^2\boldsymbol{Q}_\perp = -\dot{\boldsymbol{Q}} \times \hat{\boldsymbol{z}} - (\nabla \cdot \boldsymbol{\Pi}^*) \times \hat{\boldsymbol{z}} - (\boldsymbol{\Pi} \cdot \nabla\phi) \times \hat{\boldsymbol{z}} - (\nabla\phi \times \hat{\boldsymbol{z}})\epsilon. \tag{3.2.5}$$

Only quadratic quantities can have a contribution to the domain integrated energy flux $\langle \boldsymbol{Q}_\perp \rangle$ thus, the expression can be reduced to the two relevant contributions

$$\langle \boldsymbol{Q}_\perp \rangle = -\langle \nabla\phi \times \hat{\boldsymbol{z}}\epsilon \rangle - \langle (\boldsymbol{\Pi} \cdot \nabla\phi) \times \hat{\boldsymbol{z}} \rangle. \tag{3.2.6}$$

The overall change in energy can then be written as

$$\partial_t \epsilon + \phi \partial_t n = -\nabla \cdot (\nabla\phi \times \hat{\boldsymbol{z}}\epsilon) + \nabla \cdot (\boldsymbol{\Pi} \cdot \nabla\phi) \times \hat{\boldsymbol{z}} - \nabla \cdot \boldsymbol{S}. \tag{3.2.7}$$

As described, the energy flux in the gyrokinetic limit consists of the $\boldsymbol{E} \times \hat{\boldsymbol{z}}$ contribution of the energy flux $\boldsymbol{Q}_{\boldsymbol{E}\times\hat{\boldsymbol{z}}} = \nabla\phi \times \hat{\boldsymbol{z}}\epsilon$. Therefore, the other two contributions have to cancel $\boldsymbol{\Pi} \cdot \nabla\phi \times \hat{\boldsymbol{z}} - \boldsymbol{S} \approx 0$ are expected to cancel. The balancing of the two energy fluxes useful test of the correctness of the energy flux in the gyrokinetic regime.
Before the energy fluxes are determined from the simulations with the BSL6D code, and expression has been derived to compute the various energy flux contributions for a given electrostatic wave.

Analytical computation of quasi-linear energy fluxes

The Poynting flux $\boldsymbol{S} = \phi\boldsymbol{\Gamma}$ consists of the particle flux multiplied by the electrostatic potential. The derivation of the particle flux $\boldsymbol{\Gamma} = \int \boldsymbol{v} f \mathrm{d}^3 v$ follows the same approach as for the dispersion relation. The particle flux response is computed from the ansatz for the distribution function from equation (3.1.8). For the perpendicular flux, the two directions $(v_1, v_2) = v_\perp(-\sin\alpha, \cos\alpha)$ have been computed independently, where α is the azimuth angle in velocity space, with the property that the angle of $\hat{\boldsymbol{z}} \times \boldsymbol{k}$ corresponds to $\alpha = \frac{\pi}{2}$. For a more general calculation, the integral has been evaluated for an arbitrary complex Fourier mode $P_l = \int v_\perp e^{ila} f \mathrm{d}^3 v$, and later the fluxes have been assembled. The computation of the Fourier expansion on a gyroorbit goes analogous to the derivation of the density response

$$\begin{aligned} P_l &= \int v_\perp h_k e^{il\alpha} \mathrm{d}^3 v \\ &= \int i(\omega - \boldsymbol{k} \cdot \boldsymbol{v}^*)\phi_k f_M \sum_{m,p\in\mathbb{Z}} \frac{J_m(k_\perp v_\perp) J_p(k_\perp v_\perp) e^{i(p-m)\alpha}}{\omega - k_z v_z - p} v_\perp e^{il\alpha} \mathrm{d}^3 v. \end{aligned} \tag{3.2.8}$$

The double sum simplifies when the angle integral is evaluated with

$$\int_0^{2\pi} e^{i(p-m+l)\alpha} \mathrm{d}\alpha = 2\pi\delta_{m,p+l}. \tag{3.2.9}$$

Which gives the expression

$$P_l = 2\pi\phi_k i \int_{-\infty}^{\infty}\int_{0}^{\infty} (\omega - \boldsymbol{k}\cdot\boldsymbol{v}^*) f_M \sum_{p\in\mathbb{Z}} \left[\frac{J_{p+l}(v_\perp k_\perp) J_p(v_\perp k_\perp)}{(\omega - k_z v_z - p - l)}\right] v_\perp^2 \mathrm{d}v_\perp \mathrm{d}v_z. \quad (3.2.10)$$

The velocity integrals can be solved numerically for a given set of parameters. To compute the correct fluxes, the solution of the dispersion relation $(\omega, \boldsymbol{k})$ needs to be inserted. The fluxes can be assembled from combinations of such modes. When combining the modes on a gyro-orbit together to obtain a flux in a direction, the definition of the velocity angle α has to be kept in mind. The angle is defined such that $\boldsymbol{k}\cdot\hat{\boldsymbol{z}}$ corresponds to $\alpha = \frac{\pi}{2}$. Thus, the fluxes

$$\Gamma_1 = \frac{i}{2}\left(P_{-1} - P_1\right), \quad (3.2.11)$$

$$\Gamma_2 = \frac{1}{2}\left(P_{-1} + P_1\right), \quad (3.2.12)$$

point in the direction perpendicular (for Γ_1) and parallel (for Γ_2) of the wave vector. In the case of $\boldsymbol{k} = k\hat{\boldsymbol{y}}$, Γ_1 and Γ_2 corresponds to the x and y direction respectively. For a general wave vector, the fluxes need to be combined to compute the correct fluxes in x and y direction. The resulting velocity integrals are given by

$$\frac{\Gamma_1}{\phi_k} = -\Xi\pi \int_{-\infty}^{\infty}\int_{0}^{\infty} f_M(\sqrt{\xi}v_z, \sqrt{\xi}v_\perp) \left[\sum_{p\in\mathbb{Z}} \left(\frac{J_{p-1}(v_\perp k_\perp) J_p(v_\perp k_\perp)}{\omega - k_z v_z - p + 1} - \frac{J_{p+1}(v_\perp k_\perp) J_p(v_\perp k_\perp)}{\omega - k_z v_z - p - 1}\right)\right] v_\perp^2 \mathrm{d}v_\perp \mathrm{d}v_z, \quad (3.2.13)$$

$$\frac{\Gamma_2}{\phi_k} = \Xi\pi i \int_{-\infty}^{\infty}\int_{0}^{\infty} f_M(\sqrt{\xi}v_z, \sqrt{\xi}v_\perp) \left[\sum_{p\in\mathbb{Z}} \left(\frac{J_{p-1}(v_\perp k_\perp) J_p(v_\perp k_\perp)}{\omega - k_z v_z - p + 1} + \frac{J_{p+1}(v_\perp k_\perp) J_p(v_\perp k_\perp)}{\omega - k_z v_z - p - 1}\right)\right] v_\perp^2 \mathrm{d}v_\perp \mathrm{d}v_z, \quad (3.2.14)$$

where $\Xi = \left[\omega - k_y\left(\frac{\nabla T}{T}\partial_\xi\right)\right]$, are then computed numerically for a given wave number.

The energy flux $\boldsymbol{Q}_\perp = -\nabla\phi \times \hat{\boldsymbol{z}}\epsilon - (\boldsymbol{\Pi}\cdot\nabla\phi)\times\hat{\boldsymbol{z}}$ can be computed analogously to the Poynting flux.
For the computation of the $\boldsymbol{E}\times\boldsymbol{B}$ heat flux $\boldsymbol{Q}_\perp^{E\times B}$, the energy density response $\epsilon_k = \int \frac{v^2}{2} h_k \mathrm{d}^3 v$ needs to be computed. In Fourier space, the flux can be written as $\boldsymbol{Q}_\perp^{\boldsymbol{E}\times\boldsymbol{B}} = i\phi\boldsymbol{k}\times\hat{\boldsymbol{z}}\epsilon_k$. A tick has been applied, which significantly simplifies the computation of the energy density response. In the derivation of the dispersion relation in section 3.1, the gradient term has been written in terms of

a derivative of modified Maxwell distribution with respect to a helping variable $f_M \hat{\boldsymbol{z}} \times \frac{\nabla T}{T}\left(\frac{v_\perp^2+v_z^2}{2}-\frac{3}{2}\right) = \hat{\boldsymbol{z}} \times \frac{\nabla T}{T}\partial_\xi\left(\xi^{\frac{3}{2}} f_M(\sqrt{\xi}v_\perp, \sqrt{\xi}v_z)\right)$. The following combination of derivatives has been used

$$\frac{v^2}{2}\left[\omega - \hat{\boldsymbol{z}} \times \left(\frac{\nabla T}{T}\frac{3-(v_\perp^2+v_z^2)}{2}\right)\right] f_M = \left[\omega\partial_\xi f_M - \hat{\boldsymbol{z}} \times \frac{\nabla T}{T}\partial_\xi\left(\xi^{\frac{3}{2}}\partial_\xi f_M\right)\right], \tag{3.2.15}$$

where the helping variable ξ has been introduced in the background distribution function $f_M = f_M(\sqrt{\xi}v_\perp, \sqrt{\xi}v_z)$. The resulting energy response reads

$$\epsilon_k = \phi_k\left[\omega\partial_\xi\Psi - \hat{\boldsymbol{z}} \times \frac{\nabla T}{T}\partial_\xi\left(\xi^{\frac{3}{2}}\partial_\xi\Psi\right)\right], \text{ with} \tag{3.2.16}$$

$$\Psi = \frac{1}{|k_z|}\sqrt{\frac{\xi}{2}}e^{-\frac{k_\perp^2}{\xi}}\sum_{p\in\mathbb{Z}} Z\left(\frac{\omega+p}{|k_z|}\sqrt{\frac{\xi}{2}}\right) I_p\left(\frac{k_\perp^2}{\xi}\right).$$

For the stress induced energy flux, the Cauchy stress tensor response is computed

$$\boldsymbol{\Pi}_k = \int \boldsymbol{v}\boldsymbol{v}^T h_k \mathrm{d}^3 v. \tag{3.2.17}$$

The computation is simplified $(v_x, v_y, v_z) = (-v_\perp \sin\alpha, v_\perp\cos\alpha, v_z)$. The given definition for v_x and v_y are correct for a wave vector pointing in y-direction. Later the system can rotated to fit the given wave vector. The Cauchy stress tensor is given by

$$\boldsymbol{\Pi}_k = \int \begin{pmatrix} \frac{1}{2}v_\perp^2(1-\cos 2\alpha) & -\frac{1}{2}v_\perp^2\sin 2\alpha & -v_\perp v_z \sin\alpha \\ -\frac{1}{2}v_\perp^2\sin 2\alpha & \frac{1}{2}v_\perp^2(1+\cos 2\alpha) & v_\perp v_z\cos\alpha \\ -v_\perp v_z\sin\alpha & v_\perp v_z\cos\alpha & v_z^2 \end{pmatrix} h_k \mathrm{d}^3 v. \tag{3.2.18}$$

When introduced to the stress induced energy flux, the following result is obtained

$$\boldsymbol{Q}_\perp^\Pi = i\phi_k\left[(\boldsymbol{\Pi}_k\cdot\boldsymbol{k})\times\hat{\boldsymbol{z}}\right] = i\phi_k\int \boldsymbol{v}\boldsymbol{v}^T h_k \mathrm{d}^3 v \tag{3.2.19}$$

$$= i\phi B\int\frac{1}{2}\begin{pmatrix} k_y v_\perp^2 - k_y v_\perp^2\cos(2\alpha) + 2k_z v_\perp v_z\sin\alpha + k_x v_\perp^2\sin(2\alpha) \\ -k_x v_\perp^2 - k_x v_\perp^2\cos(2\alpha) - k_y v_\perp^2\sin(2\alpha) - 2k_z v_z v_\perp\sin\alpha \\ 0 \end{pmatrix} f\mathrm{d}^3 v. \tag{3.2.20}$$

The energy flux is assembled using the response derived in equation (3.2.10). The velocity integrals have been computed numerically for the given parameters.

Numerical results

For the numerical test, diagnostics have been implemented that can directly measure the different quantities responsible for the quasi-linear fluxes. Namely, the particle flux $\boldsymbol{\Gamma} = \int \boldsymbol{v} f \mathrm{d}^3 v$, the energy density $\epsilon = \int \frac{v^2}{2} f \mathrm{d}^3 v$ and the stress tensor components $\boldsymbol{\Pi} = \int \boldsymbol{v}\boldsymbol{v}^T \mathrm{d}^3 v$. These can be determined for each $\boldsymbol{k}$. For the simulations in section 3.1, where the growth rate and frequency of various modes have been determined, the simulations have been performed with a linearized model. In the linearized limit, the velocity advection reduces to $\nabla\phi \cdot \nabla_v f \approx \nabla\phi \cdot \boldsymbol{v} f_M$ to avoid nonlinear effects. Whereas, the simplified model still results in the correct particle flux, higher moments of the distribution function are not properly reproduced. For the purpose of these simulations, the full advection of the background distribution by the electric field has to be taken into account. To avoid saturation effects, a very small initial perturbation has to be chosen $\frac{\delta f}{f_M} \sim 10^{-8}$. All other parameters are chosen to be the same as in the simulation of the dispersion relation in section 3.1 ($N = 128 \times 128 \times 8 \times 32 \times 32 \times 32$, $L_x = L_y = \frac{20}{3}\pi$, $L_z = 480\pi$, $\Delta t = 0.03$) and the distribution function is initialized with a white noise density perturbation.
In the computation of the analytical fluxes, the coordinate system for the velocity space is chosen such at $\alpha = 0$ corresponds to the direction of the wave vector $\boldsymbol{v}|_{\alpha=0} \parallel \boldsymbol{k}$. When the fluxes are compared to the analytical results, the analytical fluxes have to rotated by the angle of the wave vector $\boldsymbol{k}$ and the x-axis.

The resulting energy fluxes in x-direction are displayed in figure 3.2. The lines show the analytical solution for the fluxes for various k_x as a function of k_y. The dots in the same color show the corresponding fluxes which have been determined from the solution. The results form the simulation show a very good agreement to analytically computed fluxes. The plot in the top row shows the $\boldsymbol{E} \times \boldsymbol{B}$ heat flux, while the plots in the bottom row show the Poynting flux (b) and the stress induced energy flux (c). The $\boldsymbol{E} \times \boldsymbol{B}$ heat flux is an order of magnitude larger than the other two fluxes. For large wave numbers, the $\boldsymbol{E} \times \boldsymbol{B}$ heat flux is proportional to the y-component of the wave vector k_y. The the values of the energy fluxes in the bottom row are almost identical, which has been expected as the gradient has been chosen close to the gyrokinetic limit and in gyrokinetic theory, the entire energy flux is given by the $\boldsymbol{E} \times \boldsymbol{B}$ heat flux.
The stress induced energy flux is caused by the magnetic field deflecting the plasma by the Lorenz force when trying to cross magnetic field lines. The Poynting flux is the energy flux in the magnetic field, that compensates for the deflections, such that no net energy flux across the magnetic field lines exists, similar to a wall deflecting a stream of fluid. The deflected water stream is deflected causing a change in energy in the stream, without any net energy fluxes that crosses the wall.

3.3 Nonlinear simulations of ITG instability

After showing that the simulations perform well in the linear regime, the nonlinear saturation of the ITG instability is studied. The grid size is changed to

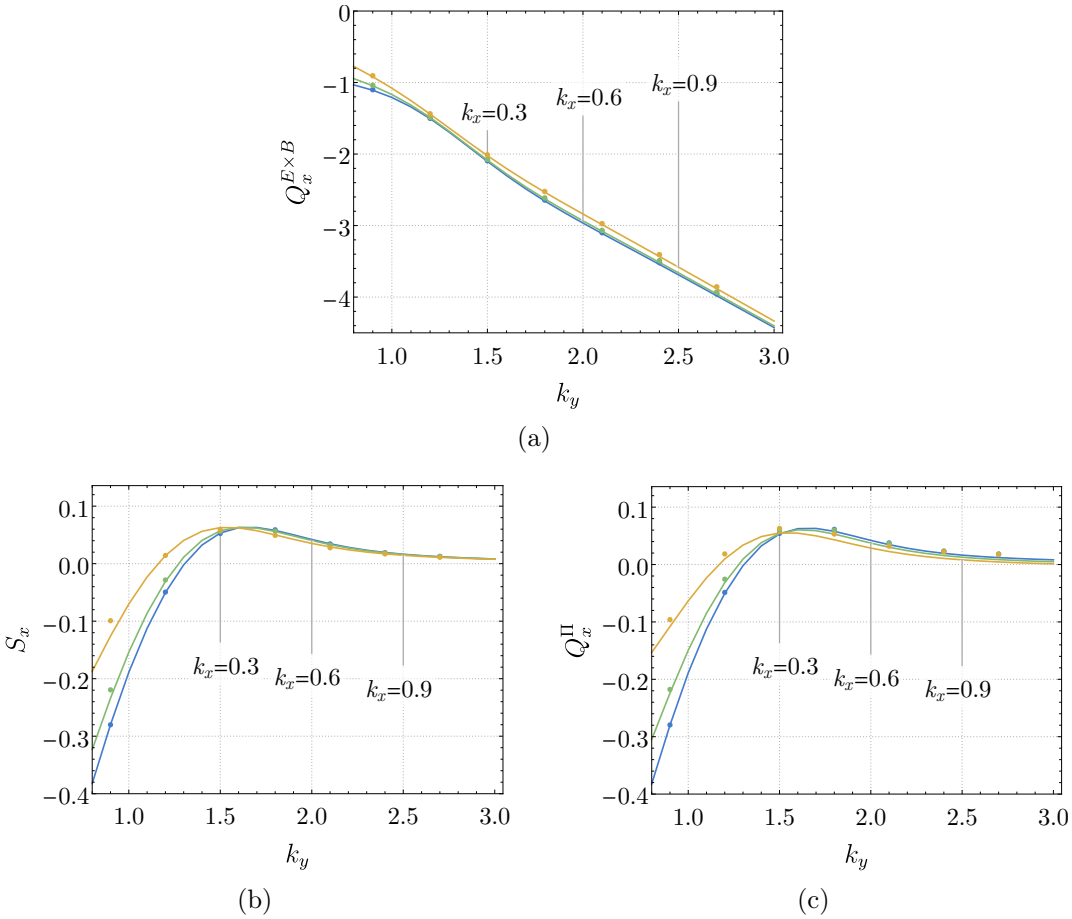

Figure 3.2: Comparison of energy fluxes (Poynting flux $\boldsymbol{S}$, $\boldsymbol{E}\times\boldsymbol{B}$ heat flux $\boldsymbol{Q}^{\boldsymbol{E}\times\boldsymbol{B}}$, and stress induced energy flux $\boldsymbol{Q}^{\Pi}$) in the direction of the temperature gradient for various wave numbers (k_x is indicated by the label) between results from numerical simulations (•) and analytical computations (-)

$N = 64 \times 64 \times 64$ compared to the simulation in section 3.1. The higher resolution in z-direction is necessary because of the occurrence of high-frequency waves in the nonlinear phase. The full set simulation parameters is found in the appendix B.2.2. Figure 3.3 shows snapshots of the density perturbation for different points in time. The density has been plotted in the x-y-plane for a fixed z-coordinate ($z = 0$). The first frame shows the initial condition. The simulation has been initialized with a white noise density perturbation, such that no Fourier mode is favored from the start. After a short initialization phase, the perturbation starts to grow due to the ion temperature gradient present in the system. The dispersion relation (compare fig. 3.1) predicts that the linear phase is dominated by modes with a wave vector which is perpendicular to the temperature gradient (compare fig. 3.3(b)), as the growth rate decays quickly with increasing wave number parallel to the gradient. After a linear growth phase, the amplitude of the perturbation saturates (fig. 3.3(c)). After the saturation phase, the simulation reaches a turbulent state (fig.

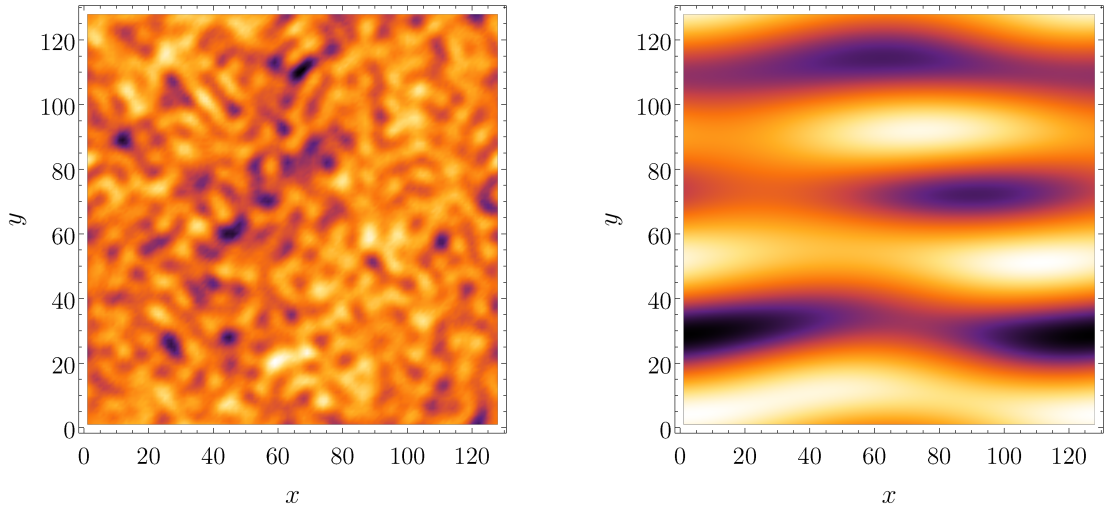

(a) t = 1000

(b) t = 3000

(c) t = 4000

(d) t = 5000

Figure 3.3: Snapshots of the particle density in the x-y-plane (with fixed z) for various points in time

3.3(d)).
For verification, the simulation results have been compared with a simulation with the gyrokinetic code CGYRO [Candy et al., 2016]. The configuration space parameters N and L have been chosen to be identical. The velocity space in the gyrokinetic code is parameterized by the kinetic energy $\epsilon \in [0, 8]$ with $N_\epsilon = 12$ points and the cosine of the pitch angle $\xi = [-1, 1]$ with $N_\xi = 32$ points. The heat flux has been chosen as a comparing quantity. The results are displayed in figure 3.4. The two

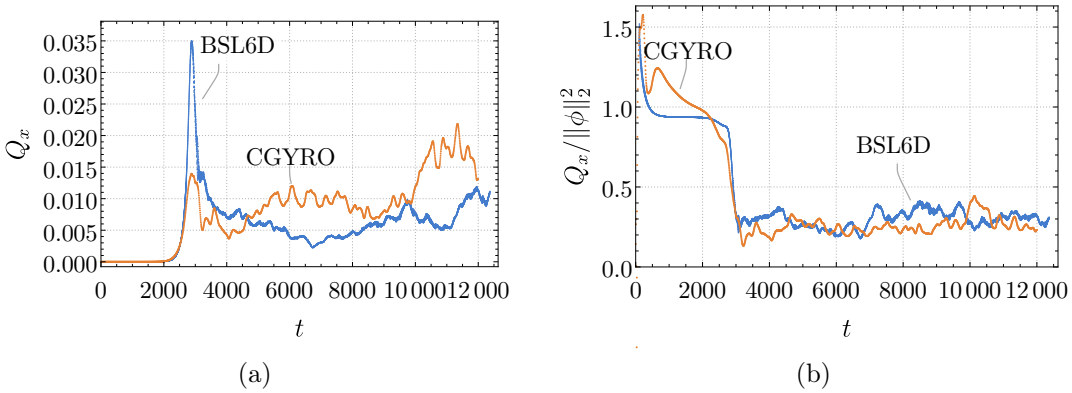

Figure 3.4: Comparison between BSL6D and gyrokinetic simulation (CGYRO) for the heat flux (a) and the ratio from heat flux and electrostatic potential

simulations are both initialized with a random noise density perturbation with the same amplitude. In the linear phase, both curves show the same growth rate. After $t \sim 3000$ both simulations saturate nonlinearly and the heat fluxes saturate to a similar level. A quantitative comparison of the fluxes in the two simulations is difficult as the fluxes are highly intermittent of the small domain size. The smallest wavenumber in the system is $k_0 = 0.3$, while the dominant growing mode has a wave number $k_y = 0.9$. Thus, only three wavelengths of the dominate mode fit into the system. Increasing the domain size would help average out the fluctuations. Apart from increasing the domain, a longer run time would improve the comparison, as more data would be obtained and a statistical comparison would be possible. Due to the high computational cost of the fully kinetic simulation, the results are deemed to be sufficient. For further validation, the ratio between the heat flux and the square mean of the electrostatic potential is shown in figure 3.4(b). In the linear phase, where the system is dominated by one mode with $k_y = 0.9$ and $k_x = 0$, the ratio is expected be $\left|\frac{Q_x}{\|\phi\|_2^2}\right| \sim 0.9$ (compare figure 3.2) which can be verified in the linear phase $t < 3000$ in the result for the BSL6D simulation. After the nonlinear saturation, the ratio drops for both simulations to $\left|\frac{Q_x}{\|\phi\|_2^2}\right| \sim 0.25$. Overall, the turbulent energy fluxes produced by the two simulation code agree well.
When studying the system in the turbulent state, one notices that high-frequency oscillations are present. The modes can be seen well when producing a video from the perturbation of the electrostatic potential, but also when looking more closely

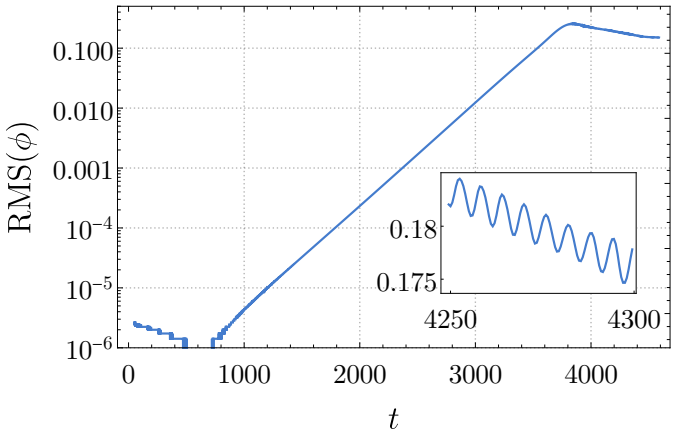

Figure 3.5: Amplitude of electrostatic potential in nonlinear ITG simulation with highlighted fast oscillations after nonlinear saturation (insert)

at the electrostatic potential amplitude in the nonlinear phase. In figure 3.5, where the root mean square (RMS) of the electrostatic potential is displayed, an insert is added, which focuses on a short period $t\omega_{\mathrm{ci}} = 4250{-}4300$ after the saturation. A first estimate suggests that the period of these oscillations is $\frac{\#\text{ oscillations}}{\text{time}} \approx \frac{8}{50} = 6.25$. The time is normalized such that the period of one Larmor oscillation of the ion has a period of $T = 2\pi$, suggesting that the frequency of these oscillations is close to the Larmor frequency.
The occurrence of such high-frequency oscillations in the saturation of nonlinear ion temperature gradient simulations has been mentioned before in literature [Miecnikowski et al., 2018]. However, a detailed description, let alone, a study of their excitation is yet missing.

Properties of fast oscillations occurring during nonlinear saturation

To obtain a better understanding of the modes that are excited in the later stage of the simulation, a spectrogram $\sigma(t, \omega)$ of the density perturbation is computed

$$\sigma(t,\omega) = \frac{1}{V}\int \left| \int_{t-\Delta t/2}^{t+\Delta t/2} n(\tau, \boldsymbol{r}) w(\tau) e^{i\omega\tau} \mathrm{d}\tau \right| \mathrm{d}^3 x, \tag{3.3.1}$$

where V is the volume of the domain, Δt is the period over which the Fourier transform is computed and $w(\tau)$ is a window function, which increases the quality of the Fourier transform by suppressing the signal at the boundaries of the time window. In our case, a Kaiser window [Oppenheim et al., 2001] has been used, which has yielded the best separation of the modes.
A logarithmic density plot of the spectrogram is displayed in figure 3.6. The spectro-

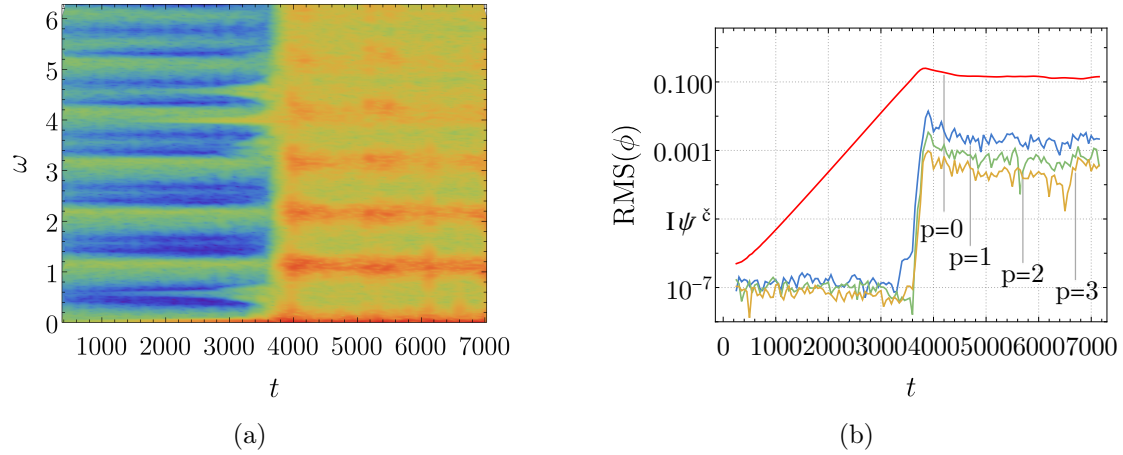

Figure 3.6: Logarithmic density plot of density perturbation spectrogram (a) and amplitude of perturbation filtered by various frequencies corresponding to different gyro-harmonics (b). (0) is the ITG contribution, (1-3) are the amplitudes of the first three frequency bands

gram shows clearly that at the time of nonlinear saturation ($t \sim 3800$), a multitude of modes with high frequencies $\omega \sim \omega_c$ are excited. In the linear phase, modes are limited to low-frequency modes $\omega \ll \omega_c$. The fact that the high-frequency modes are excited close to the harmonics of the Larmor frequency suggests that these modes are ion Bernstein waves [Bernstein, 1958].
To get a more quantitative view of the excitation of these oscillations, the amplitude of the density perturbation has been subjected to a frequency band filter. The amplitudes of modes in the frequency ranges $|\omega| \in \left[0, \frac{1}{2}\right] (p = 0)$, $|\omega| \in \left[\frac{1}{2}, \frac{3}{2}\right] (p = 1)$, $|\omega| \in \left[\frac{3}{2}, \frac{5}{2}\right] (p = 2)$ and $|\omega| \in \left[\frac{5}{2}, \frac{3}{2}\right] (p = 3)$, are displayed in figure 3.6. The first curve $(p = 0)$ corresponding to the lowest frequency interval contains all the gyrokinetic physics. The plot shows the linear growth of the ITG instability and the nonlinear saturation. The other three graphs describe the perturbation amplitude filtered for the frequencies around the harmonics of the Larmor frequency. At the beginning of the simulation, these modes are stable and remain on the same level as their initial amplitude. At the point in time, when the ITG mode starts to saturate, these modes are excited. The growth period coincides with the saturation phase of the ITG, in which the amplitude takes its maximum and saturates to its turbulent state. After the short excitement phase, the high-frequency modes also saturate and remain on a constant level. The amplitude decreases with higher frequencies.
After investigating the frequency of these fast Bernstein-like oscillations, the spatial distribution has been studied. The same frequency filter as in equation 3.3.1 has been applied to the density perturbation. However, instead of computing the RMS of the filtered perturbation, 3D renders of the fluctuations with low frequencies $|\omega| \in \left[0, \frac{1}{2}\right]$ and for frequencies around the first harmonic $\omega \in \left[\frac{1}{2}, \frac{3}{2}\right]$ have been produced. The resulting images for $t = 4000$ are displayed in figure 3.7. From studying the spatial distribution of these high-frequency oscillations, two main insights have

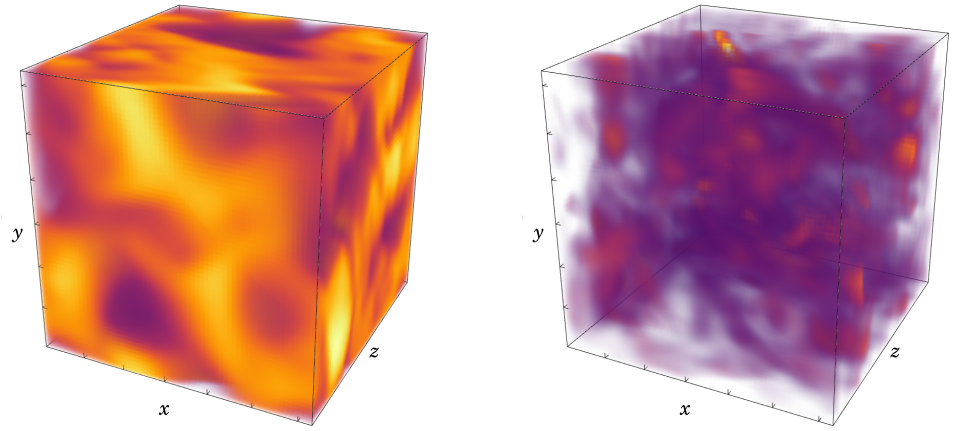

(a) (b)

Figure 3.7: 3D render of the density perturbation filtered for low frequencies $\omega \in \left[0, \frac{1}{2}\right]$ (a) and frequencies close to the Larmor frequency $\omega \in \left[\frac{1}{2}, \frac{3}{2}\right]$ (b)

been gained. The plot of the filtered density perturbation 3.7(b) shows that the excitation of these waves is very localized, leading to higher wave numbers compared to the ITG modes. Furthermore, the excitation of these modes coincides with the maxima and minima of the ITG perturbation. This is very difficult to display in static images, however, is apparent in video renderings of the time evolution.
The discussion of excitation mechanisms of such high-frequency waves is not subject of this section. The stability of ion Bernstein waves is discussed in chapter 4. However, the local conditions surrounding the excitation of the excitation of the IBWs have been investigated. The ITG modes are of gyrokinetic modes, hence, the velocity distribution is isotropic (i.e. consists of the $m = 0$ modes) when described in gyrocenter coordinates $(\boldsymbol{R}, v_\perp, v_z)$. The complete description of the relation between gyrokinetics and the fully kinetic model can be found in 2.4, where the Vlasov equation has been transformed to to gyrocenter coordinates $\boldsymbol{R} = \boldsymbol{r} + \boldsymbol{v} \times \hat{\boldsymbol{z}}$. After the coordinate transformation, the distribution function can be expanded in Fourier modes in the velocity angle

$$g(\boldsymbol{R}, v_\perp, v_z, \alpha) = \sum_{m \in \mathbb{Z}} e^{im\alpha} g_m(\boldsymbol{R}, v_\perp, v_z). \tag{3.3.2}$$

The gyrokinetic part $g_0(\boldsymbol{R}, v_\perp, v_z)$ is obtained by integrating over the velocity angle α. During the discussion of the Penrose criterion in section 2.3.2 we have learned, that the stability of a mode is strongly determined by the perpendicular velocity profile of the background distribution. To get a sense of the velocity profile, the profile for different times (marked by the dashed lines in figure 3.8) leading up to the saturation point at the position of the maximal perturbation has been plotted in

in figure 3.8(b). The profiles show that the distribution function becomes negative in the course of the saturation.
Two parts in the numerical description can potentially cause negative phase space densities. On the one side, Lagrange interpolation is known for creating large oscillations towards the edges of the stencil, which can overshoot into the negative. Large overshoots can be largely circumvented by either limiting the time step to comply with the CFL criteria $\Delta t < \frac{\Delta x}{\sqrt{2} v_{\max}}$ (the factor $\sqrt{2}$ originates in the rotating grid) or moving the stencil such that the point of interpolation is always located within the center nodes of the stencil. However, the interpolation method is still not positivity preserving and can lead to negative phase space densities. The second effect that can cause negative phase space densities is the source term $\nabla_{\boldsymbol{v}} S(\boldsymbol{r}, \boldsymbol{v})$ that is introducing the linearized temperature gradient. Its integrated profile $\int S(v_z, v_z) \mathrm{d}v_\perp$ is displayed alongside the distribution function in figure 3.8 as the light gray line. The source term (3.0.4) is added every time step to the distribution function independent of the perturbation amplitude. The derivation of the local temperature gradient assumes small amplitudes which is not necessarily fulfilled for the given simulation, in which the perturbation level reaches $\sim 25\%$ of the background.
The impact on the stability of ion Bernstein modes is discussed in chapter 4, where

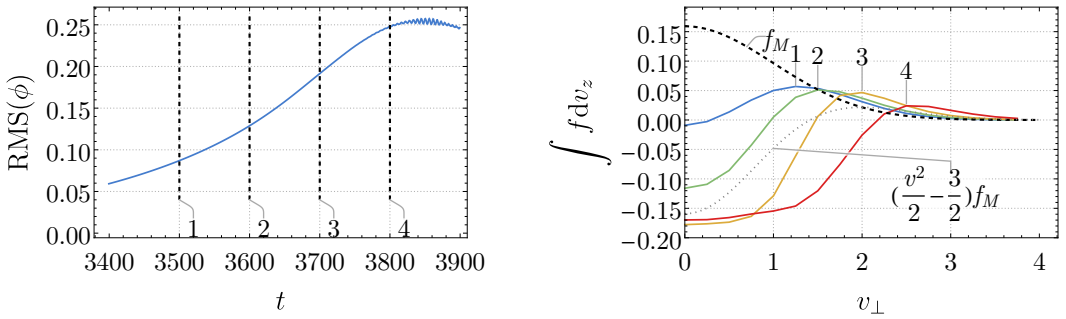

Figure 3.8: Perturbation amplitude of electrostatic potential leading up to saturation point (a), with markings (dashes lines) corresponding to perpendicular velocity profiles of the distribution function at the position of the maximal perturbation (b) in comparison to equilibrium distribution (dashed black line)

different excitement mechanisms for high-frequency oscillations are discussed. In chapter (chapter 5), simulations with a nonlinear treatment of the temperature gradient are performed, which do not show the same negative phase space densities.

3.4 Summary

This chapter, focuses on the verification of the kinetic simulation code BSL6D [Kormann et al., 2019] in the gyrokinetic regime. Various simulations of an ion temperature gradient instability have been performed. Section 3.1 show that the kinetic

code BSL6D is able to reproduce the correct growth rates and frequencies for modes in a large range of wave vector. In addition to the dispersion relation, the energy flux induced by the linear modes have been studied. A comprehensive description of the various contribution to the energy flux in the fully kinetic system has been derived which shows that the energy flux in our system consist of three main contributions, the $\boldsymbol{E} \times \boldsymbol{B}$ heat flux, a stress induced energy flux and the Poynting flux. The calculations in section 3.2 have confirmed that the Poynting flux and the stress induced energy flux cancel almost completely in the gyrokinetic limit and the entire energy flux is caused by the $\boldsymbol{E} \times \boldsymbol{B}$ heat flux.
Furthermore, the nonlinear saturation if the ITG instability and the resulting turbulence has been simulated. The code produces the correct nonlinear saturation level and heat transport values in the turbulent state which has been verified by a comparative study with the gyrokinetic code CGYRO.
In these simulations, the system shows the presence of fast oscillating waves $\omega \sim \omega_{\mathrm{ci}}$ with frequencies close to the harmonics Larmor frequency. These waves are excited at the time of saturation and are very localized, thus, have wavenumbers significantly larger than the ITG modes. When investigating the surrounding conditions of the excited high-frequency waves, one sees that the distribution function locally has negative phase space densities. Investigation of the negative phase space densities have shown that these are caused by the local treatment temperature gradient, which is induced in the system by the means of a source term (3.0.4). The source term is added in every time step and does not conserve the positivity of the distribution function. In the nonlinear saturation phase, the amplitude of the perturbation reaches around 25% of the background density. For such large perturbations, the local treatment might not be applicable anymore. In chapter 5, a nonlinear treatment of the temperature gradient is introduced, eliminating some of the problems caused by the local gradient.

Chapter 4

Study of stability of ion Bernstein waves (IBWs)

Parts of this chapter have been presented at the DPG spring meeting 2022 [Raeth et al., 2022] and is going to be published in [?](Manuscript in preparation)

This chapter discusses the existence of waves in the Vlasov system, that lay outside the gyrokinetic regime. Chapter 3 has shown that such waves can be excited in the nonlinear saturation phase of the slab-ITG simulation. The existence high-frequency waves in electrostatic plasmas have been known since 1958 [Bernstein, 1958] and a few studies on the possible cyclotron instabilities have been published [Gary and Sanderson, 1979, Yoon et al., 2014, Noreen et al., 2019]. However, the stability properties of the ion Bernstein waves are scarcely studied.

4.1 Dispersion relation of stable IBWs

The existence of high frequency waves in the Vlasov system can be shown from the dispersion relation (3.1.8)

$$0 = \left[\omega - k_y \frac{\nabla T}{T}\partial_\xi\right] \frac{1}{|k_z|}\sqrt{\frac{\xi}{2}} e^{-\frac{k_\perp^2}{\xi}} \sum_{p\in\mathbb{Z}} Z\left(\frac{\omega + p}{|k_z|}\sqrt{\frac{\xi}{2}}\right) I_p\left(\frac{k_\perp^2}{\xi}\right) - 2. \tag{4.1.1}$$

With $\frac{\nabla T}{T} = 0$ and $\xi = 1$, the dispersion relation reads

$$0 = \frac{\omega}{2|k_z|} \sum_{p\in\mathbb{Z}} Z\left(\frac{\omega + p}{\sqrt{2}|k_z|}\right) \Gamma_n - 2, \tag{4.1.2}$$

with $\Gamma_n = e^{-k_\perp^2} I_n(k_\perp^2)$. In case of fast oscillations in the perpendicular plane, any parallel motion has a small to negligible influence (compare discussion 6.2), as the parallel transition time is much larger than the Larmor period $\omega_c \gg k_z v_{th}$ and thus, the limit $k_z \to 0$ can be taken which reduces The plasma dispersion function $Z(x)$

to

$$\lim_{k_z \to 0} \frac{1}{\sqrt{2}|k_z|} Z\left(\frac{\omega + p}{\sqrt{2}|k_z|}\right) = \frac{1}{\omega + p}. \tag{4.1.3}$$

The dispersion relation from equation 4.1.2 results in

$$0 = \omega \sum_{p \in \mathbb{Z}} \frac{\Gamma_n}{\omega + p} - 2 = \Gamma_0 + \omega \sum_{\substack{p \in Z \\ p \neq 1}} \frac{\Gamma_n}{\omega + p} - 2. \tag{4.1.4}$$

Before solving the solutions the dispersion relation, a discussion should make the expression more tangible. A better understanding will greatly help later when discussing possible instabilities. Contrary to the case of finite k_z, the dispersion relation is a purely real function depending on the frequency $\omega \in \mathbb{R}$ and the amplitude of the perpendicular wave vector $k_\perp$. When extracting the 0th element of the sum (compare eq. 4.1.4) three destined parts are obtained. The "-2" on the right-hand side originates from a combination of the contribution of the adiabatic electrons (with $T_e = 1$) and the adiabatic response of the distribution function $f_{\text{adia}} = \phi f_M$ (compare 3.1). The zeroth term of the sum is the gyrokinetic density response. In the case without gradients, the dependen of the frequency ω cancels, and results in a frequency independent response. Figure 4.1 shows the right-hand side of (4.1.4) for different cut off $p_{\max}$ of the sum. The blue line (with the label (0)) shows the frequency-independent part of the three contributions just above. Every other line increases $p_{\max}$ by one, adding the two terms $-p_{\max}$ and $p_{\max}$. Every term adds two

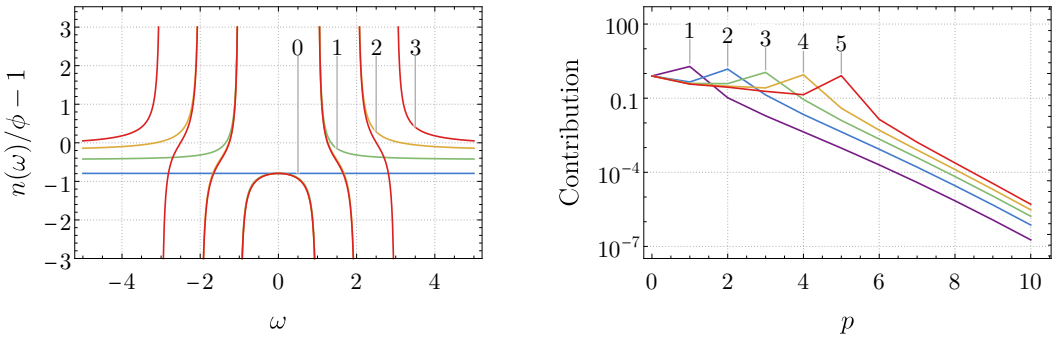

(a) (b)

Figure 4.1: Dispersion function (4.1.4) for a fixed $k_\perp = 2$ as a function of the frequency for different number of $p_{\max}$ indicated by the label (b) and contribution $|\chi^p(\omega, k_\perp) - \chi^{p-1}(\omega, k_\perp)|$ by the summands p to the susceptibility (4.1.5) to the different solutions

poles or resonances and two roots to the dispersion relation. Because the resonances are the harmonics of the Larmor frequencies, the resulting roots are located close to the respective resonance.

To compute the roots numerically, the infinite sum has to be cut at a certain $p_{\max}$ such that

$$\chi^{p_{\max}} = \Gamma_0 + \sum_{p=1}^{p_{\max}} \left(\frac{\omega\Gamma_n}{\omega + p} + \frac{\omega\Gamma_n}{\omega - p} \right) - 2. \tag{4.1.5}$$

In order to confidently cut the sum without loosing too much accuracy, the contribution of each term in the infinite sum is studied. Figure 4.1(b) shows the absolute value of the contribution of each term to the density response. Every line corresponds to a different solution n close to the different harmonics at a fixed $k_\perp$. To compute the contribution, the solution $(\omega, k_\perp)$ close to the nth harmonic has been determined with a very large $p_{\max}$. The contribution of each pth summand is then given by $|\chi^p(\omega, k_\perp) - \chi^{p-1}(\omega, k_\perp)|$. Figure 4.1.5(b) shows that for each harmonic n, the contribution of the $p = n$ term is dominant. The summands with $p < n$ are smaller but not negligible. For larger $k_\perp$, their significance increases (not shown in the figure). For the term $p > n$, the absolute value decays exponentially. Thus, for computing the solution for the nth harmonic, the sum can be cut at $p_{\max} > n$.
The dispersion function is solved analytically for the lower harmonics, while for higher harmonics a standard root-finding algorithm is used. The solutions with positive frequencies are displayed in figure 4.2. Solutions close to every harmonic of the Larmor frequency are obtained and the frequency ω for each solution is slightly shifted up compared to the harmonic.
The dispersion relation can also be reproduced in simulations with th 6D kinetic code BSL6D [Kormann et al., 2019]. A grid with $L_\perp = \frac{20\pi}{3}$ and $N_x = 128 \times 8 \times 8$ has been chosen for the linear simulations. As the system is completely rotationally symmetric around the z-axis, the discussion focuses on the dispersion relation for k_x with $k_y = 0$. The complete simulation parameters can be found in the appendix B.3.1.

After the simulation has been initialized with a random density perturbation, most modes in the system are damped and after a certain period ($t = 6000$), the only remaining modes in the systems are the IBWs. Their dispersion relation has been determined by Fourier transforming the electrostatic potential in time and space $\phi(\boldsymbol{k}, \omega)$(figure 4.2(b)). The spectrum shows in red branches of modes with frequencies around the harmonics. The analytical solutions have been plotted as black dashed lines for a better comparison, which perfectly match the mode structure from the simulation. For larger k_x, the amplitude of the IBWs is decaying which is an effect of the numerical diffusion discussed in section 2.6.3. Close to the signal, other branches can be seen in light yellow. These signals are orders of magnitude smaller and are only visible due to the logarithmic scale. These signals are caused by aliasing. Increasing the time resolution of the simulation decreases the amplitude of these spurious modes. The excellent agreement between the analytically derived and simulated dispersion relation has shown that the code is capable in producing correct results, even in regimes far beyond the gyrokinetic description.

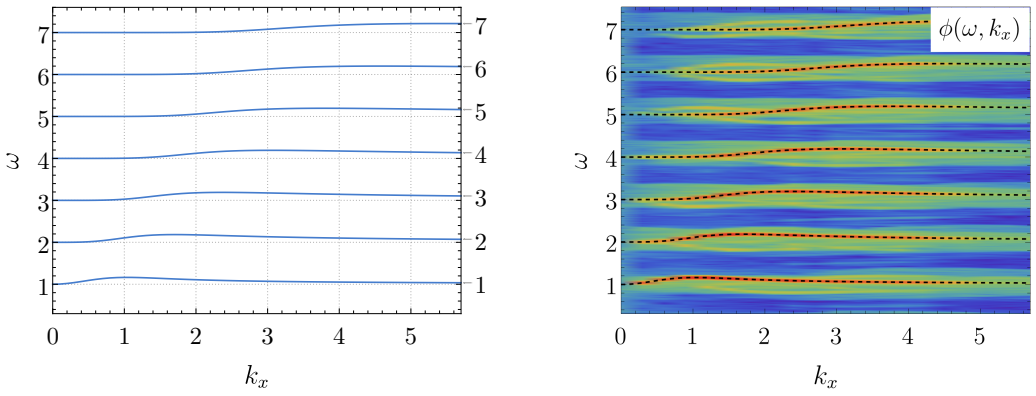

(a) (b)

Figure 4.2: Dispersion relation for non-damped ion Bernstein waves determined from linear simulations (a) and the spectrum $\phi(\omega, k_\perp)$ overlaid with the analytical solutions (b)

4.2 Linear instability of IBW with background velocity distribution

In the following sections, I study the stability of ion Bernstein waves in various scenarios by developing and using various methods to investigate instabilities. These include, the demonstration of the existence of unstable modes with the Cauchy argument principle, determining stability thresholds given a certain background distribution function, and simulating instabilities with the 6D kinetic code BSL6D.

4.2.1 Stability of IBW in nonlinear ITG simulations

After showing that the Vlasov system has electrostatic solutions with frequencies close to the harmonics of the Larmor frequency and that the BSL6D code can correctly reproduce the dispersion relation of these modes, the focus is shifted the focus to the study of the stability of these modes. A natural starting point for the investigation is the nonlinear ITG simulation from section 3.3 which have shown the presences of such waves.
Unstable modes exist, when the dispersion relation

$$\chi(\boldsymbol{k}, \omega) = \sum_s \chi_s(\boldsymbol{k}, \omega) = 0, \tag{4.2.1}$$

has a solution with Im $\omega > 0$. Cauchy's argument principle can be used to determine the existence of solutions in a given domain, without finding solutions to the complex equation. Section 2.3.3 discusses a general expression for the electric susceptibility for a general source for which the distribution function from the ITG simulation

f^{ITG} is introduced in the ansatz of the susceptibility from equation (2.3.39)

$$\chi(\boldsymbol{k},\omega) = \int \left[(\omega f_M - \boldsymbol{k}\cdot\nabla_{\boldsymbol{v}} f^{\mathrm{ITG}} - \boldsymbol{k}\cdot\boldsymbol{v} f_M)\phi_k \sum_{m,p\in\mathbb{Z}} \frac{J_m(k_\perp v_\perp)J_p(k_\perp v_\perp)e^{i(p-m)\alpha}}{\omega - k_z v_z - p} \right] \mathrm{d}^3 v - 2. \tag{4.2.2}$$

The distribution function from the ITG simulation f^{ITG} consists of two parts, a homogeneous Maxwellian background f_M and the perturbation S. When both are introduced in the expression for the susceptibility, the Maxwellian is cancel with the $-\boldsymbol{k}\cdot\boldsymbol{v} f_M$ term resulting in

$$\chi(\boldsymbol{k},\omega) = \int \left[(\omega f_M - \boldsymbol{k}\cdot\nabla_{\boldsymbol{v}} S)\phi_k \sum_{m,p\in\mathbb{Z}} \frac{J_m(k_\perp v_\perp)J_p(k_\perp v_\perp)e^{i(p-m)\alpha}}{\omega - k_z v_z - p} \right] \mathrm{d}^3 v - 2. \tag{4.2.3}$$

The derivation follows the assumption that $S(\boldsymbol{r},\boldsymbol{v})$ is a function of the gyration center and the parallel and perpendicular velocity $S(\boldsymbol{r},\boldsymbol{v}) = S(\boldsymbol{R}+\boldsymbol{\rho}, v_\perp, v_z) = S^\circ(\boldsymbol{R}, v_\perp, v_z)$ and the velocity derivative can be written as

$$\nabla_{\boldsymbol{v}} S(\boldsymbol{r},\boldsymbol{v}) = \hat{\boldsymbol{z}}\times\nabla_{\boldsymbol{R}} S^\circ + \nabla_{\boldsymbol{v}} S^\circ. \tag{4.2.4}$$

The derivation the dispersion relation for the ITG instability focused on spatial gradients $\hat{\boldsymbol{z}}\times\nabla_{\boldsymbol{R}} S^\circ$. In this section, the influence of the velocity gradient of the source $\nabla_{\boldsymbol{v}} S^\circ$ is studied here. The spatial dependency is neglected which corresponds assumption that the wave length of the background perturbation is much larger than the wave length of the perturbation and that the background can be considered homogeneous in configuration space over the wavelength of the unstable modes. The background distribution S° only depends on the absolute values of perpendicular and parallel velocity and thus the gradient can be written as

$$\begin{aligned} \boldsymbol{k}\cdot\nabla_{\boldsymbol{v}} S^\circ &= \boldsymbol{k}\cdot\left(\nabla_{\boldsymbol{v}} v_\perp \frac{\partial S^\circ}{\partial v_\perp} + \nabla_{\boldsymbol{v}} v_z \frac{\partial S^\circ}{\partial v_z}\right) \\ &= \boldsymbol{k}_\perp\cdot\hat{\boldsymbol{v}}_\perp \frac{\partial S^\circ}{\partial v_\perp} + k_z \frac{\partial S^\circ}{\partial v_z}. \end{aligned} \tag{4.2.5}$$

Furthermore, we is assumed that $k_\perp \gg k_z$ and thus, the parallel velocity derivative can be neglected

$$\boldsymbol{k}\cdot\nabla_{\boldsymbol{v}} S^\circ \approx k_\perp \cos\alpha \frac{\partial}{\partial v_\perp}, \tag{4.2.6}$$

where α is the angle coordinate of the velocity in cylindrical coordinates defined with respect to $\boldsymbol{k}$ such that for $\alpha = 0 \to \boldsymbol{v}_\perp \parallel \boldsymbol{k}_\perp$. Introducing the angle as the source in the expression for the susceptibility, Euler's identity $\cos\alpha = \frac{e^{i\alpha}}{2} + \frac{e^{-i\alpha}}{2}$ is

used to solve the integral

$$\int_0^{2\pi} e^{i(p-m\pm1)}\mathrm{d}\alpha = 2\pi\delta_{m,p\pm1}, \tag{4.2.7}$$

resulting in the susceptibility

$$\chi = 2\pi\int_0^\infty\int_{-\infty}^\infty \left[\omega P_0 f_m - \frac{1}{2}\frac{\partial S}{\partial v_\perp}P_{+1} - \frac{1}{2}\frac{\partial S}{\partial v_\perp}P_{-1}\right]\mathrm{d}^3v - 2, \tag{4.2.8}$$
$$\text{with } P_l = \sum_{p\in\mathbb{Z}}\frac{J_{p+l}(k_\perp v_\perp)J_p(k_\perp v_\perp)}{\omega - k_z v_z - p}.$$

After deriving an expression for the electric susceptibility for arbitrary velocity gradient of a source, results from the nonlinear simulation in chapter 3 are introduced. Here, I am only interested in an illustration of the instability of nonlinear ion Bernstein waves in the nonlinear saturation phase rather than a full quantitative description, the problem is simplified significantly.
I have used the distribution function at $t = 3800$, the time shortly before the occurrence of the IBWs in the simulation (compare figure 3.8). In section 3.3, the discussion of IBWs distribution in position space has shown that the excitation of these fast oscillating modes coincides with the maxima and minima of the density perturbation. Hence, the distribution function is selected at the point of maximal perturbation and is assumed to be constant over the configuration space.
The distribution function is transformed to gyrocenter coordinates $\boldsymbol{R} = \boldsymbol{r} - \boldsymbol{\rho}$ and gyroaveraged to compute the velocity angle independent part $S^\circ(\boldsymbol{R}, v_\perp, v_z)$. The coordinate transformation is computed by Fourier transforming the distribution and multiplying the Fourier modes with the phase corresponding to the shift about the Larmor radius or each velocity.
The result is displayed in figure 4.3(a) as a function of the $(v_\perp, v_z)$. The negative phase space density has already been discussed in figure 3.8. For the computation of the susceptibility, the derivative with respect to $v_\perp$ (shown in figure 4.3(b)) has been computed with a first order finite difference approximation and the integrals are evaluated numerically using the rectangle rule

$$\chi = 2\pi\frac{1}{\Delta v^2}\sum_i\sum_j\left[\omega P_0(v_\perp^i, v_z^j)f_M(v_\perp^i, v_z^j) - \frac{1}{2}\frac{S^\circ(v_\perp^{i+1}, v_z^j) - S^\circ(v_\perp^i, v_z^j)}{\Delta v}P_{+1}(v_\perp^i, v_z^j)\right.$$
$$\left.\frac{1}{2}\frac{S^\circ(v_\perp^{i+1}, v_z^j) - S^\circ(v_\perp^i, v_z^j)}{\Delta v}P_{-1}(v_\perp^i, v_z^j)\right] - 2. \tag{4.2.9}$$

The expression in equation 4.2.9 can be evaluated for a set of $(k_\perp, k_z, \omega)$. The goal is to find a set of $(k_\perp, k_z, \omega)$ such that $\chi(k_\perp, k_z, \omega) = 0$. Evaluating the numerical integration for every ω in the complex plane and searching for solutions to the dispersion relation is computationally too expensive, and is not necessary to show the

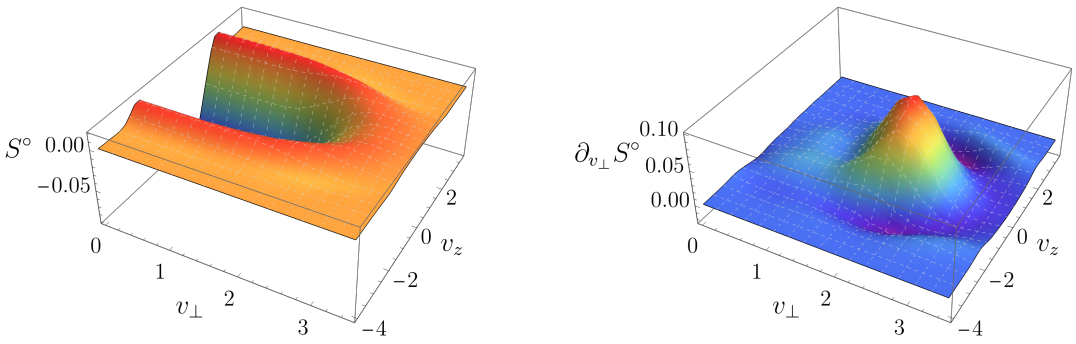

(a) (b)

Figure 4.3: Distribution function of nonlinear ITG simulation in gyrocenter coordinates S° (a) and the derivative $\partial_{v_\perp} S^\circ$ at point of maximum density perturbation

existence of unstable solutions (Im $\omega > 0$). Cauchy's argument principle (compare 2.3.2) is used to prove the presence of solutions with Im $\omega > 0$. Given a complex function $f(z)$, with $z \in \mathbb{C}$ tracing out a closed path $\partial\Omega$ in the complex plane, the line integral

$$\frac{1}{2\pi i} \oint_{\partial\Omega} \frac{f'(z)}{f(z)} \mathrm{d}z = N - P, \tag{4.2.10}$$

gives the difference of the number of roots N and poles P of $f(z)$ inside the domain Ω enclosed by the path $\partial\Omega$. This is equivalent to the winding number of the image of $f(z)$ around the origin, i.e. if the path $\partial\Omega$ traces out a path around the root of $f(z)$ in counter-clockwise direction, the image of $f(z)$ traces out a path circling around the origin exactly once. Section 2.3.2 has explained how the principle argument can be used to find any root above the real axis and to find the number of unstable modes. However, instead of integrating over the entire real axis of ω, our knowledge about the distribution pf the solutions can be. All roots of $\chi(\omega)$ are located close to the harmonics of the Larmor frequency and that the susceptibility quickly approaches a constant value when moving away from the solution, which can be seen in figure 2.6. Instead of using one path that covers the entire upper half of the complex plane, the path can be split into multiple small paths covering the region around the harmonics as visualized in figure 4.4.
The paths consist of a line parallel to the real axis at $\omega = \omega' + i\epsilon$, with $\omega' \in \mathbb{R}$ and $\epsilon \ll 1$ and circular bow closing the loop on top. When the closing path is chosen wide enough, it can be assumed that the susceptibility is constant and its contribution to the path integral can be neglected. The image the path ω under map $\chi(\omega)$ can be plotted in the complex plane and the winding number around the origin corresponds to the number of solutions for the given frequency and $\boldsymbol{k}$. I have plotted the images of the paths illustrated in figure 4.4 for multiple $k_\perp = \frac{8}{10}, \frac{16}{10}, \frac{24}{10}$ and $k_z = \frac{1}{120}, \frac{1}{240}$ in figure 4.5. The different columns correspond to the different harmonics $\omega = 1, 2, 3, 4$

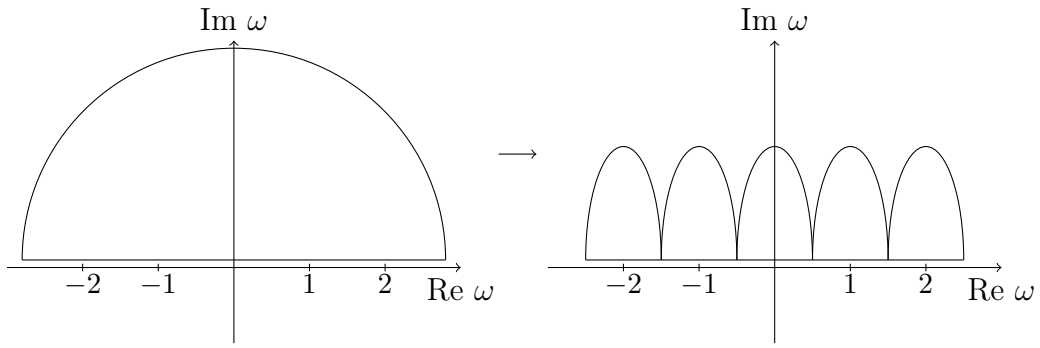

Figure 4.4: Integration paths for Cauchy argument principle covering the entire upper half (a) or small sections around the harmonics of the Larmor frequency (b) of the complex plane

and the rows to the different $k_\perp$, while the lines in the plot show different different k_z. The plots shown that for some combinations of parameters, the curve loops around the origin. The number of times the curve inscribes the origin corresponds to the winding number and thus, to the number of solutions with a positive growth rate. One has to be careful that these plots have been computed for $\omega = \omega' + i\epsilon$, whith $\epsilon = 0.0001$, which means that only modes with a growth rate Im $\omega > 0.0001$ can be found. The reason for the choice of ϵ is that the numerical integration is unstable for small offsets from the real axis. A finite ϵ is not an issue for this discussion, as I am interested in instabilities with growth rates large enough, that they can account for the existence of the high-frequency waves in the nonlinear simulations from section 3.3.

The presence of negative phase space densities is non-physical and is an artifact of the local treatment of the temperature gradient. In a simulation with a realistic gradient model, the Vlasov equation, when discretized correctly, preserves the positivity of the distribution function. The result in this section shows that negative phase space densities can cause spurious high-frequency waves in the non-linear phase. The demonstration gives a possible explanation the presence of high-frequency waves in simulations with a local treatment of the temperature gradient, which have already been witnessed by others [Sturdevant et al., 2016]. Understanding the origin provides me with more confidence in the functionality of the BSL6D code because the modes are an artifact of the model rather than the discretization. Furthermore, the example provides a first example of the instability of ion Bernstein waves.

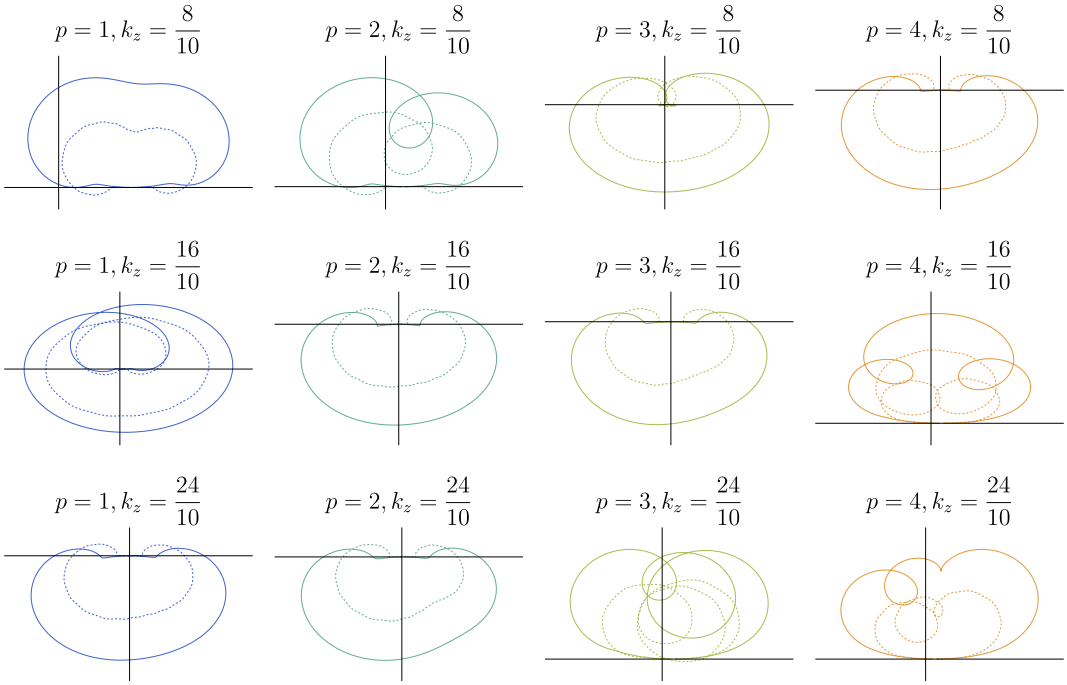

Figure 4.5: Images of the paths $\partial\Omega$ displayed in figure 4.4 surrounding areas close to the harmonics of the Larmor frequency under the mapping $\chi(\omega)$ in the complex plane (Re χ, Im χ). The columns correspond to the various harmonics of the Larmor frequency and the row to the various $k_\perp$ (rows) and $k_z = \frac{1}{120}$ (solid line) and $k_z = \frac{1}{240}$ (dashed line). Every system with for which the image inscribes the origin, has a solution $\chi(\omega) = 0$ with Im $\omega > 0$

4.2.2 Gradient source term in form of δ-ring

Section 4.2.1 has outlined an explanation for the occurrence of IBWs in the saturation phase of nonlinear ITG simulations with a local temperature gradient. Although the source for the instability is the negative phase space density generated by the local gradient source term, the example presents a first example of such an instability. The following sections works towards more realistic scenarios, in which the cyclotron instability occurs. In this work I denote all linearly unstable ion Bernstein waves as cyclotron instability independent of the source.
In a first step, I investigate the influence of a δ-ring distribution on top of a Maxwellian distribution on the stability of the IBWs. For the derivation the expression for the electrostatic susceptibility (derived in equation 2.3.39)

$$\chi(\boldsymbol{k},\omega) = \int \left[(\omega f_M - \boldsymbol{k}\cdot\nabla_{\boldsymbol{v}} S + \boldsymbol{k}\cdot\nabla_{\boldsymbol{v}} f_M) \sum_{m,p\in\mathbb{Z}} \frac{J_m(k_\perp v_\perp) J_p(k_\perp v_\perp) e^{i(p-m)\alpha}}{\omega - k_z v_z - p} \right] \mathrm{d}^3 v - 2 \tag{4.2.11}$$

is used as starting point. The contribution of the background distribution $\boldsymbol{k}\cdot\nabla S$ replaced by

$$\boldsymbol{k}\cdot\nabla_{\boldsymbol{v}} S = \gamma k_\perp \delta(v_\perp - \tilde{v}_\perp) f_M(v_\perp, v_z) + \boldsymbol{k}\cdot\nabla_{\boldsymbol{v}} f_M. \tag{4.2.12}$$

Similar studies can be found in literature [Noreen et al., 2019, Yoon et al., 2014]. The integral over the velocity angle can be computed directly, because (4.2.12) is independent of α. Before the source is introduced, the integrals are rearranged

$$\begin{aligned}
\chi &= \int_{-\infty}^{\infty}\int_{0}^{\infty} (\omega f_M - \boldsymbol{k}\cdot\nabla_{\boldsymbol{v}} S + \boldsymbol{k}\cdot\nabla_{\boldsymbol{v}} f_M) \sum_{p\in\mathbb{Z}} \frac{2\pi J_p(v_\perp k_\perp)^2}{\omega - k_z v_z - p} v_\perp \mathrm{d}v_\perp \mathrm{d}v_z - 2 \\
&= \sum_{p\in\mathbb{Z}} \int_0^\infty 2\pi J_p(v_\perp k_\perp)^2 v_\perp \int_{-\infty}^{\infty} \frac{(\omega f_M - \boldsymbol{k}\cdot\nabla_{\boldsymbol{v}} S + \boldsymbol{k}\cdot\nabla_{\boldsymbol{v}} f_M)}{\omega - k_z v_z - p} \mathrm{d}v_z \mathrm{d}v_\perp - 2.
\end{aligned} \tag{4.2.13}$$

The goal in this section is, to find a threshold γ' such that for $\gamma > \gamma'$ the IBWs become unstable. This is equivalent with the idea, that one wants to find a γ' such that a solution to $\chi(\omega, \boldsymbol{k}) = 0$ exists with $\omega = \tilde{\omega} + i\epsilon$ ($\tilde{\omega} \in \mathbb{R}$) and $0 < \epsilon \ll 1$. For the rephrased problem the Sokhotski–Plemelj theorem can be used, assuming $\tilde{\omega} - k_z v_z - p \in \mathbb{R}$

$$\lim_{\epsilon\to 0} \frac{1}{x + i\epsilon} = -i\pi\delta(x) + P(\frac{1}{x}) \tag{4.2.14}$$

to modify the integrand. $\delta(x)$ is the Dirac-delta function and $P(\frac{1}{x})$ is the Cauchy principle value of $\frac{1}{x}$. Applying the Sokhotski–Plemelj theorem and taking the imag-

inary part of (4.2.13) results in

$$0 = \sum_{p\in\mathbb{Z}} \int_0^\infty 2\pi J_p(v_\perp k_\perp)^2 v_\perp \int_{-\infty}^\infty (\tilde{\omega} f_M - \boldsymbol{k}\cdot\nabla_{\boldsymbol{v}} S + \boldsymbol{k}\cdot\nabla_{\boldsymbol{v}} f_M)\times \tag{4.2.15}$$
$$\mathrm{Im}\left[-i\pi\delta(\tilde{\omega} - k_z v_z - p) + P\left(\frac{1}{\tilde{\omega} - k_z v_z - p}\right)\right] \mathrm{d}v_z \mathrm{d}v_\perp.$$

The principle value $P\left(\frac{1}{\tilde{\omega}-k_z v_z - p}\right)$ is real. Hence, the integral reads

$$0 = \sum_{p\in\mathbb{Z}} \int_0^\infty J_p(v_\perp k_\perp)^2 v_\perp \int_{-\infty}^\infty (\omega f_M - \boldsymbol{k}\cdot\nabla_{\boldsymbol{v}} S + \boldsymbol{k}\cdot\nabla_{\boldsymbol{v}} f_M)\delta(\omega - k_z v_z - p)\mathrm{d}v_z \mathrm{d}v_\perp. \tag{4.2.16}$$

In the further derivation the "$\sim$" in the real part of the frequency $\tilde{\omega}$ is omitted. The source term $\boldsymbol{k}\cdot\nabla_{\boldsymbol{v}} S^\circ$ from equation 4.2.12 is introduced and the integrals evaluated

$$0 = \sum_{p\in\mathbb{Z}} \Bigg[\underbrace{\int_0^\infty J_p(v_\perp k_\perp)^2 v_\perp \int_{-\infty}^\infty \omega f_M(v_z, v_\perp)\delta(\omega - k_z v_z - p)\mathrm{d}v_z \mathrm{d}v_\perp}_{(1)}$$
$$\underbrace{- \int_0^\infty J_p(v_\perp k_\perp)^2 v_\perp \int_{-\infty}^\infty k_\perp \gamma \delta(v_\perp - \tilde{v}_\perp) f_M(v_z, v_\perp)\delta(\omega - k_z v_z - p)\mathrm{d}v_z \mathrm{d}v_\perp}_{(2)} \Bigg]. \tag{4.2.17}$$

The perpendicular integral in the second term is integrated

$$\begin{aligned}(2) \to &\int_0^\infty J_p(v_\perp k_\perp)^2 v_\perp \\ &\times \int_{-\infty}^\infty k_\perp \gamma \delta(v_\perp - \tilde{v}_\perp) f_M(v_z, v_\perp)\delta(\omega - k_z v_z + p)\mathrm{d}v_z \mathrm{d}v_\perp \\ &= J_p(\tilde{v}_\perp k_\perp)^2 \tilde{v}_\perp \int_{-\infty}^\infty k_\perp \gamma f_M(v_z, \tilde{v}_\perp)\delta(\omega - k_z v_z + p)\mathrm{d}v_z. \end{aligned} \tag{4.2.18}$$

From $\delta(\omega - k_z v_z - p)$, the condition is obtained that $v_z = \frac{\omega - p}{k_z}$. The result of the integral is given by

$$(2) \to J_p(\tilde{v}_\perp k_\perp)^2 \tilde{v}_\perp k_\perp \gamma f_M\left(\left(\frac{\omega + p}{k_z}\right), \tilde{v}_\perp\right). \tag{4.2.19}$$

The parallel integral of the first term is solved with the same condition, after which the dispersion relation is given by

$$0 = \sum_{p\in\mathbb{Z}} e^{-\frac{1}{2}\left(\frac{\omega-p}{k_z}\right)^2} \left[\int_0^\infty J_p(v_\perp k_\perp)^2 v_\perp \omega e^{-\frac{1}{2}v_\perp^2} \mathrm{d}v_\perp - k_\perp \tilde{v}_\perp \gamma e^{-\frac{1}{2}\tilde{v}_\perp^2} J_p(\tilde{v}_\perp k_\perp)^2\right]. \tag{4.2.20}$$

I assume that the parallel wavenumber is small $k_z \ll 1$ and that the frequency of the growing mode is close to a harmonic of the cyclotron frequency $\omega = n + \delta\omega$, with $\frac{\delta\omega}{\omega} \ll 1$. With this assumption, the sum is reduced, as the only significant contribution comes from the term with $p = n$

$$0 = \int_0^\infty J_n(v_\perp k_\perp)^2 v_\perp \omega e^{-\frac{1}{2}v_\perp^2} \mathrm{d}v_\perp - k_\perp \gamma \tilde{v}_\perp e^{-\frac{1}{2}\tilde{v}_\perp^2} J_n(\tilde{v}_\perp k_\perp)^2. \tag{4.2.21}$$

The remaining integral is evaluated in the same way as in the calculations of a dispersion function with $\Gamma_n = \int_0^\infty e^{-\frac{v_\perp^2}{2}} J_n(k_\perp v_\perp)^2 v_\perp \mathrm{d}v_\perp = I_n(k_\perp^2) e^{-k_\perp^2}$. The final dispersion relation reads

$$0 = \Gamma_n \omega - k_\perp \gamma e^{-\frac{1}{2}\tilde{v}_\perp^2} J_n(\tilde{v}_\perp k_\perp)^2 \tilde{v}_\perp. \tag{4.2.22}$$

The derived equality can be solved for γ and the stability condition

$$\gamma' = \frac{I_p(k_\perp^2)\omega e^{-k_\perp^2}}{k_\perp e^{-\frac{1}{2}\tilde{v}_\perp^2} J_p(\tilde{v}_\perp k_\perp)^2 \tilde{v}_\perp}, \tag{4.2.23}$$

is derived. The threshold is shown in figure 4.6 as a function of the perpendicular wavenumber $k_\perp$ for a mode with frequency close to the first (a) or second (b) harmonic of the Larmor frequency. The different lines show the threshold for different positions $\tilde{v}_\perp$ of the ring in velocity space. Overall fairly large wave numbers are required to get threshold $\gamma' < 0.1$. The results in figure 4.6 show that there are in principle source terms that can be introduced into the Vlasov equation which lead to a destabilization of the ion Bernstein wave. The ansatz for the perturbation (4.2.12) has two limitations. Firstly, the extreme nature of a δ-function with its singularity is far from any real application, an) secondly, any velocity gradient of any distribution function $\boldsymbol{k} \cdot \nabla_{\boldsymbol{v}} f(v_\perp) = \boldsymbol{k} \cdot \hat{\boldsymbol{v}}_\perp \partial_{v_\perp} f = k_\perp \cos(\alpha) \partial_{v_\perp} f$ contains a dependency of the velocity angle, which complicates the integration. The second problem is addressed in section 4.2.3.

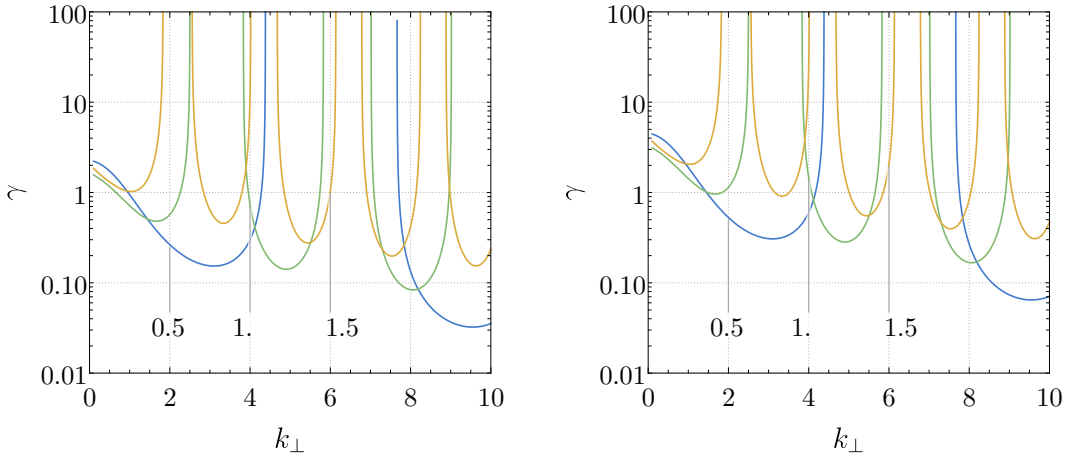

(a) $\omega \approx 1$ (b) $\omega \approx 2$

Figure 4.6: Stability threshold γ as a function of $k_\perp$ for various $\tilde{v}_\perp$ indicated by the labels

4.2.3 Instability induced by ring-distribution function

Starting from the ansatz for the susceptibility (2.3.39)

$$\chi(\boldsymbol{k},\omega) = \int \left[(\omega f_M - \boldsymbol{k}\cdot\nabla_{\boldsymbol{v}} S + \boldsymbol{k}\cdot\nabla_{\boldsymbol{v}} f_M) \sum_{m,p\in\mathbb{Z}} \frac{J_m(k_\perp v_\perp) J_p(k_\perp v_\perp) e^{i(p-m)\alpha}}{k_z v_z - \omega - p} \right] \mathrm{d}^3 v - 2, \tag{4.2.24}$$

a more realistic ansatz for the perturbation $\boldsymbol{k}\cdot\nabla_{\boldsymbol{v}} S^\circ$ compared to section 4.2.2 has been chosen. The ansatz for the distribution function consists of two parts, a Maxwellian background f_M and secondly, a stationary background $h_0 = h_0(\boldsymbol{R}, v_\perp, v_z)$. The function $g(\boldsymbol{R},\boldsymbol{v})$ and $h(\boldsymbol{r},\boldsymbol{v})$ are both used for the same distribution function depending on the coordinate system is expressed in. As an ansatz for the stationary background distribution function, a δ-function in $v_\perp$ in $g(\boldsymbol{R},\boldsymbol{v})$

$$g_0(\boldsymbol{R},\boldsymbol{v}) = \gamma f_M(\tilde{v}_\perp, v_z) \int e^{i\boldsymbol{k}\cdot\boldsymbol{R}} \delta(v_\perp - \tilde{v}_\perp)\delta(\boldsymbol{k}-\boldsymbol{k}_0)\mathrm{d}^3 k, \tag{4.2.25}$$

is used. While the distribution function in gyrocenter coordinates is independent of the velocity angle, the same distribution expressed in configuration space $h_0(\boldsymbol{r},\boldsymbol{v})$ shows depends on the velocity angle

$$h_0(\boldsymbol{r},\boldsymbol{v}) = \gamma f_M(\tilde{v}_\perp, v_z) \int e^{i(\boldsymbol{k}\cdot\boldsymbol{r} - \boldsymbol{k}\cdot\boldsymbol{\rho})} \delta(\boldsymbol{k}-\boldsymbol{k}_0)\mathrm{d}^3 k. \tag{4.2.26}$$

In figure 4.7, two illustrations of the ring-distribution are shown for $\tilde{v}_\perp = 1$ with different $\boldsymbol{k}_0$. The ring was broadened with a Gaussian for illustrative purposes. In

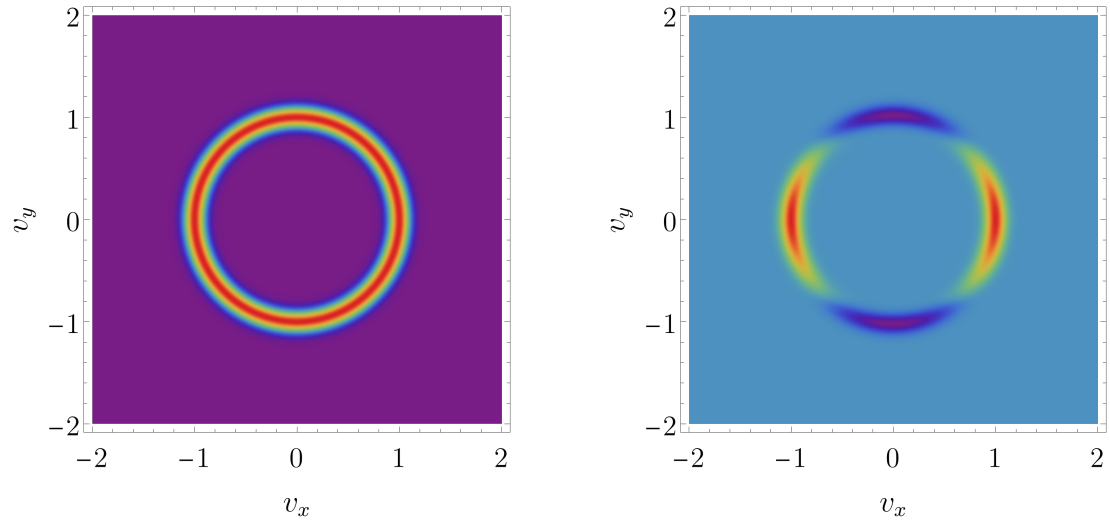

(a) $\boldsymbol{k} = 0$ (b) $\boldsymbol{k} = \hat{\boldsymbol{x}}$

Figure 4.7: Illustration for the ring distribution (broadened for visibility) $h(\boldsymbol{r}, \boldsymbol{v})$ for $\boldsymbol{k}_0 = 0$(a) and $\boldsymbol{k}_0 = \hat{\boldsymbol{x}}$(b)

the case of $\boldsymbol{k} = 0$, the transformation does not change the distribution function and $h(\boldsymbol{r}, \boldsymbol{v})$ is independent of the velocity angle. For a finite $\boldsymbol{k} > 0$ (b), the transformation introduces a velocity dependence.

We assume that the distribution function h_0 is the result of a primary perturbation which resides on top of a thermal background. Together, these can be introduced in (4.2.24) as the source for the system $S = f_M + h(\boldsymbol{r}, \boldsymbol{v})$. The two Maxwellian distributions cancel and the velocity gradient $\nabla_{\boldsymbol{v}} h$ is computed

$$\nabla_{\boldsymbol{v}} h_0 = \hat{\boldsymbol{z}} \times \nabla g_0 + \nabla_{\boldsymbol{v}} g_0. \tag{4.2.27}$$

In Fourier space that velocity distribution for a single wave vector $\boldsymbol{k}_0$ is give by

$$h_0^k(v_\perp, \theta) = \gamma f_M(\tilde{v}_\perp, v_z)\delta(v_\perp - \tilde{v}_\perp) \exp(i(\hat{\boldsymbol{z}} \times \boldsymbol{k}_0) \cdot \boldsymbol{v}), \tag{4.2.28}$$

$$g_0^k(v_\perp, \theta) = \gamma f_M(\tilde{v}_\perp, v_z)\delta(v_\perp - \tilde{v}_\perp). \tag{4.2.29}$$

From here on the Fourier space specific decorations of h_0 and g_0 are dropped. The velocity space gradient of the ring distribution function reads

$$\begin{aligned}
\nabla_{\boldsymbol{v}} h_0 =& \gamma \left[(\hat{\boldsymbol{z}} \times i\boldsymbol{k}_0)\delta(v_\perp - \tilde{v}_\perp) + \nabla_{\boldsymbol{v}}\delta(v_\perp - \tilde{v}_\perp)\right] f_M(\tilde{v}_\perp, v_z) e^{i(\hat{\boldsymbol{z}} \times \boldsymbol{k}_0)\cdot \boldsymbol{v}} \\
=& \gamma \left[(\hat{\boldsymbol{z}} \times i\boldsymbol{k}_0)\delta(v_\perp - \tilde{v}_\perp) + (\nabla_{\boldsymbol{v}} v_\perp)\delta'(v_\perp - \tilde{v}_\perp)\right] f_M(\tilde{v}_\perp, v_z) e^{i(\hat{\boldsymbol{z}} \times \boldsymbol{k}_0)\cdot \boldsymbol{v}} \\
=& \gamma \left[(\hat{\boldsymbol{z}} \times i\boldsymbol{k}_0)\delta(v_\perp - \tilde{v}_\perp) + \frac{\boldsymbol{v}_\perp}{v_\perp}\delta'(v_\perp - \tilde{v}_\perp)\right] f_M(\tilde{v}_\perp, v_z) e^{i(\hat{\boldsymbol{z}}_0 \times \boldsymbol{k}_0)\cdot \boldsymbol{v}}.
\end{aligned} \tag{4.2.30}$$

The derivative of the ring distribution displayed in figure 4.7 is shown in figure 4.8.

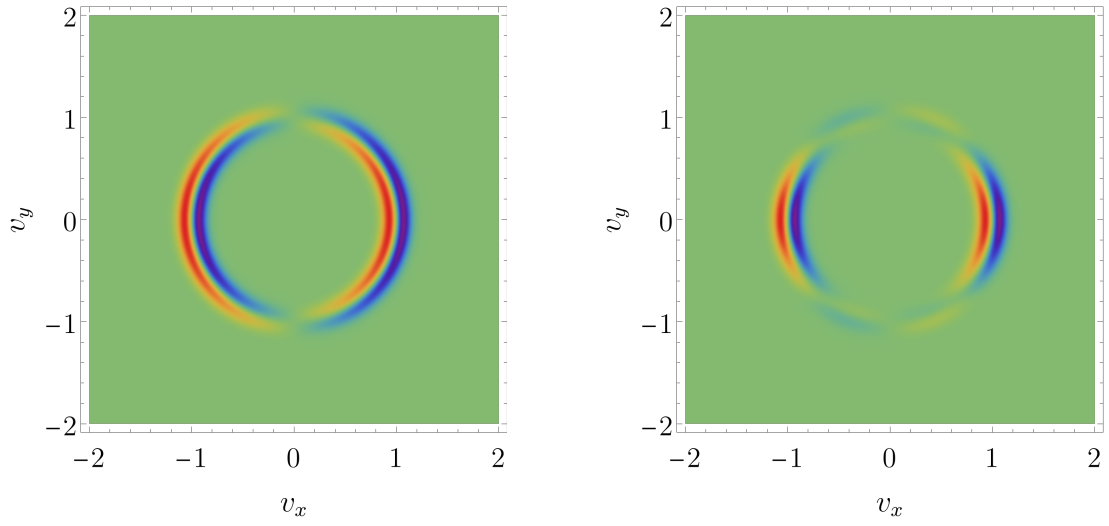

(a) $\boldsymbol{k} = 0$ (b) $\boldsymbol{k} = \hat{\boldsymbol{x}}$

Figure 4.8: Illustration for the velocity gradient ring distribution (broadened for visibility) $\partial_{v_x} h(\boldsymbol{r}, \boldsymbol{v})$ for $\boldsymbol{k}_0 = 0$(a) and $\boldsymbol{k}_0 = \hat{\boldsymbol{x}}$(b)

In case of $\boldsymbol{k}_0 = 0$ (figure 4.8(a)) the graph shows that $m = 1$ behavior caused by the prefactor $\hat{\boldsymbol{x}} \cdot \frac{\boldsymbol{v}_\perp}{v_\perp} = \cos\alpha$.
The expression of the velocity gradient from equation (4.2.30) is introduced in the expression for the susceptibility (4.2.24).

$\delta-$ring distribution with $\boldsymbol{k}_0 = 0$ We focus on a source distribution with $\boldsymbol{k}_0 = 0$, which drastically simplifies the calculation as no mode interaction between the wavenumber of the background $\boldsymbol{k}_0$ and the wavenumber $\boldsymbol{k}$ of the perturbations needs to be considered. Without a spatial dependency the gyrotransformation becomes unity and $g_0 = h_0 = \gamma f_M(\tilde{v}_\perp, v_z)\delta(v_\perp - \tilde{v}_\perp)$. Hence, the velocity derivative is given by

$$\boldsymbol{k}_\perp \cdot \nabla_{\boldsymbol{v}} h_0 = \gamma k_\perp \cos\alpha \delta'(v_\perp - \tilde{v}_\perp) f_M(\tilde{v}_\perp, v_z). \tag{4.2.31}$$

The limit $k_z \to 0$ is assumed, because the frequency ω of the IBWs is so large, that any parallel motion can be neglected $v_{\text{th}} k_z \ll \omega$. The first part of the integral in (2.3.39) is independent of the background distribution h_0 and can be computed identically to the computation of the dispersion relation for the ITG instability (compare 3.1). Thus, in the first step, we focus the contribution of the ring-distribution to

the susceptibility

$$\chi^S(\boldsymbol{k},\omega) = \int \left[\boldsymbol{k}_\perp \cdot \nabla_{\boldsymbol{v}} h_0 \sum_{m,p\in\mathbb{Z}} \frac{J_m(k_\perp v_\perp) J_p(k_\perp v_\perp) e^{i(p-m)\alpha}}{k_z v_z - \omega - p} \right] \mathrm{d}^3 v$$
$$= \int \left[\gamma k_\perp \cos\alpha \delta'(v_\perp - \tilde{v}_\perp) f_M(\tilde{v}_\perp, v_z) \sum_{m,p\in\mathbb{Z}} \frac{J_m(k_\perp v_\perp) J_p(k_\perp v_\perp) e^{i(p-m)\alpha}}{\omega - p} \right] \mathrm{d}^3 v. \tag{4.2.32}$$

The integral over the velocity angle is solved by using Euler's formula

$$\int_0^{2\pi} \cos\alpha e^{i(p-m)\alpha} \mathrm{d}^3 v = \frac{1}{2} \int_0^{2\pi} e^{i(p-m+1)} + e^{i(p-m-1)} \mathrm{d}^3 v$$
$$= \pi \left(\delta_{m,p-1} + \delta_{m,p+1} \right). \tag{4.2.33}$$

The resulting Kronecker delta eliminates one of the two sums and the susceptibility reads ($a(v_\perp, v_z) = \pi\gamma k_\perp \delta'(v_\perp - \tilde{v}_\perp) f_M(\tilde{v}_\perp, v_z)$ is introduced to shorten the expression)

$$\chi^S(\boldsymbol{k},\omega) = \int_{-\infty}^{+\infty} \int_0^{\infty} \left[\sum_{m,p\in\mathbb{Z}} a(v_\perp, v_z) \frac{\left[J_{p+1}(k_\perp v_\perp) + J_{p-1}(k_\perp v_\perp) \right] J_p(k_\perp v_\perp)}{\omega - p} \right] v_\perp \mathrm{d}v_\perp \mathrm{d}v_z. \tag{4.2.34}$$

The recursion relation for the Bessel functions $\frac{2p}{x} J_p(x) = J_{p+1}(x) + J_{p-1}(x)$ is used to further simplify the expression

$$\chi^S(\boldsymbol{k},\omega) = \int_{-\infty}^{+\infty} \int_0^{\infty} \left[\sum_{m,p\in\mathbb{Z}} a(v_\perp, v_z) \frac{2p}{k_\perp v_\perp} \frac{J_p(k_\perp v_\perp)^2}{k_z v_z - \omega - p} \right] v_\perp \mathrm{d}v_\perp \mathrm{d}v_z$$
$$= \int_{-\infty}^{+\infty} \int_0^{\infty} \left[\sum_{m,p\in\mathbb{Z}} \frac{\gamma p}{\sqrt{2\pi}} \delta'(v_\perp - \tilde{v}_\perp) e^{-\frac{\tilde{v}_\perp^2 + v_z^2}{2}} \frac{J_p(k_\perp v_\perp)^2}{\omega - p} \right] \mathrm{d}v_\perp \mathrm{d}v_z. \tag{4.2.35}$$

We can use integration by parts to move the derivative away from the $\delta-$distribution $\int \delta'(v - \tilde{v}_\perp) f(v) \mathrm{d}v = -\int \delta(v - \tilde{v}_\perp) f'(v) \mathrm{d}v$. After introducing the transformation, the perpendicular velocity integral can be evaluated

$$\chi^S(\boldsymbol{k},\omega) = -\int_{-\infty}^{+\infty} \left[\sum_{m,p\in\mathbb{Z}} \frac{\gamma p}{\sqrt{2\pi}} e^{-\frac{\tilde{v}_\perp^2 + v_z^2}{2}} \frac{\partial}{\partial \tilde{v}_\perp} \frac{J_p(k_\perp \tilde{v}_\perp)^2}{\omega - p} \right] \mathrm{d}v_z. \tag{4.2.36}$$

At this point, the parallel velocity integral is computed resulting in the susceptibility contribution of the δ-ring background distribution

$$\chi^S(\boldsymbol{k},\omega) = -\sum_{p\in\mathbb{Z}} \gamma p e^{-\frac{\tilde{v}_\perp^2}{2}} \frac{\partial}{\partial \tilde{v}_\perp} \frac{J_p(k_\perp \tilde{v}_\perp)^2}{\omega - p}. \tag{4.2.37}$$

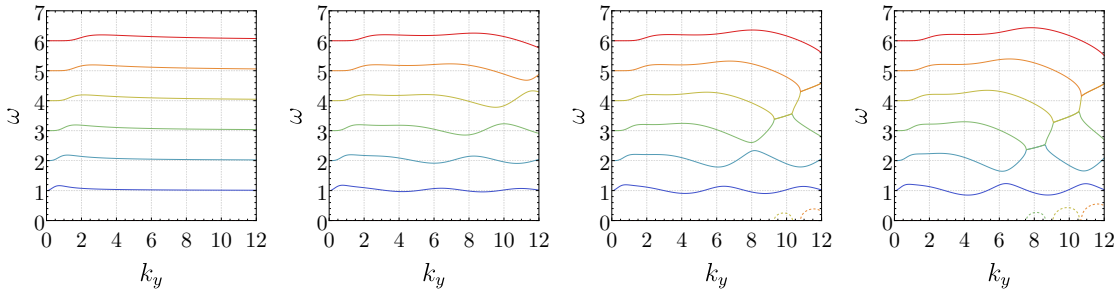

(a) $\gamma = 0.0$ (b) $\gamma = 0.1$ (c) $\gamma = 0.2$ (d) $\gamma = 0.3$

Figure 4.9: Frequencies (solid lines) and growth rates (dashed lines) for δ-ring distribution with $\tilde{v}_\perp = 0.5$ for various $\gamma = 0, 0.1, 0.2, 0.3$ (Lines of the same color correspond to the same solution)

Together with the susceptibility of the unperturbed system, which was derived in the discussion of the stable ion Bernstein waves (4.1.4), dispersion relation can be derived. The full susceptibility is given by

$$\chi(\boldsymbol{k}, \omega) = \varphi \sum_{p \in \mathbb{Z}} \frac{1}{\omega - p} \left[-\gamma p e^{-\frac{\tilde{v}_\perp^2}{2}} \partial_{\tilde{v}_\perp} J_p(k_\perp \tilde{v}_\perp)^2 + \Gamma_n \right] - 2, \tag{4.2.38}$$

with $\Gamma_n = I_n(k_\perp^2) e^{-k_\perp^2}$. The dispersion relation is given by solutions $(\omega, \boldsymbol{k})$ of the equation $\chi = 0$.
Some example dispersion relations for various γ are displayed in figure 4.9. We can confirmed as a first sanity check, that the correct dispersion relation for the stable ion Bernstein waves is reproduced with $\gamma = 0$.
With an increase in γ, the individual branches start to warp until two neighboring branches meet and the imaginary part of the frequency becomes non-zero and the instability arises. To understand better how these instabilities behave, we want to focus on the merge of the two branches $p = 2$ and $p = 3$ at $k_y = 8$. The complex phase of the susceptibility Im $\log \chi$ is plotted in figure 4.10 for in creasing γ starting at $\gamma = 0.2$. The color scheme is chosen, such that every color corresponds one particular phase. If the phase of χ circles through all the phases (all the colors) when following a path P in the complex plane, the path encircles either a pole or a root of χ. The direction in which χ goes through the values of the complex phase determines whether the feature is a root or a pole. This is the visual equivalent of Cauchy's argument principle. The plots in figure 4.10(a) show the poles located at the harmonics of the Larmor frequency $\omega = 1, 2, 3$ and the two roots in between $\omega = 2$ and $\omega = 3$. For increasing γ these roots move closer together until they merge, and an instability is formed Im $\omega > 0$.

Gauss ring distribution function The derived dispersion relation can be used as a Green's function [Green, 1828] to derive the dispersion relation of any distribution

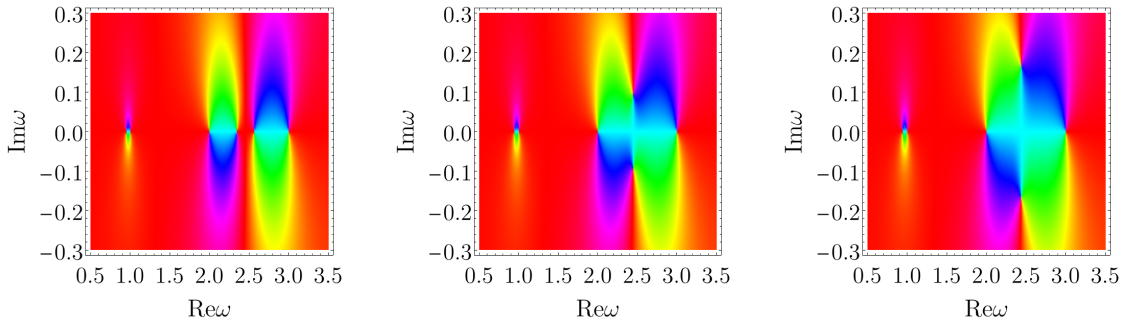

(a) $\gamma = 0.2$ (b) $\gamma = 0.22$ (c) $\gamma = 0.24$

Figure 4.10: Complex phase of susceptibility response for a δ-ring background with varying amplitude $\gamma = 0.2$(a), 0.22(a), 0.24(a), for $k_\perp = 8$

function which is isotropic in the perpendicular velocity plane. Given the result $\chi(\boldsymbol{k}, \omega, \tilde{v}_\perp)$ from (4.2.38), the susceptibility for an arbitrary distribution $h(v_\perp)$ is given by

$$\chi^{h(v_\perp)}(\boldsymbol{k}, \omega) = \int \chi(\boldsymbol{k}, \omega, \tilde{v}_\perp) h(\tilde{v}_\perp) \mathrm{d}\tilde{v}_\perp. \tag{4.2.39}$$

As an example, I illustrate the broadening of the distribution function from a δ-ring to a Gaussian ring. The background distribution is defined as

$$h_{\text{Gauss}}(v_\perp) = \frac{\sqrt{\alpha} e^{-\frac{v_\perp^2}{2} - \alpha(v_\perp - \tilde{v}_\perp)^2}}{\pi^{\frac{3}{2}}(1 + \operatorname{erf}(\sqrt{\alpha}\tilde{v}_\perp))}. \tag{4.2.40}$$

The distribution function is chosen, such that the properties of a δ-function are retained in the limit $\alpha \to \infty$ and $\int_0^\infty h_{\text{Gauss}}(v_\perp)\mathrm{d}v_\perp = 1$. In figure 4.11, the distribution function is plotted for various $\alpha = 1, 10, 100, 1000$. The functions are normalized to their maximum value for the visualization.

The dispersion relation has been computed by numerically finding solutions $(\omega, k_\perp)$ of

$$0 = \chi^{h_{\text{Gauss}}}(\boldsymbol{k}, \omega) = \int_0^\infty \chi(\boldsymbol{k}, \omega, \tilde{v}_\perp) h_{\text{Gauss}}(\tilde{v}_\perp) \mathrm{d}\tilde{v}_\perp. \tag{4.2.41}$$

The results are displayed in figure 4.12. The distribution function resembles the original δ-distribution for large α $\lim_{\alpha\to\infty} h_{\text{Gauss}} = \frac{e^{-\frac{\tilde{v}_\perp^2}{2}}}{2\pi}\delta(v_\perp - \tilde{v}_\perp)$. Henceforth, the dispersion relation is expected converges to the results shown in figure 4.9. For comparability, an amplitude of $\gamma = 0.3$ is chosen. The dispersion relation for $\alpha = 1000$ (figure 4.12(d)) is almost identical to the result in plot 4.9(d). For smaller α (from (d) $\to$ (a)), the Gauss distribution gets broader and the instability disappears.

With the example of the Gauss ring-distribution, I have demonstrated that the

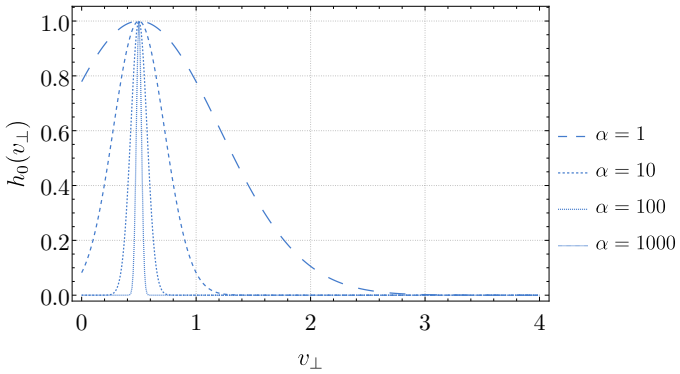

Figure 4.11: Different Gauss profiles of the background distribution function

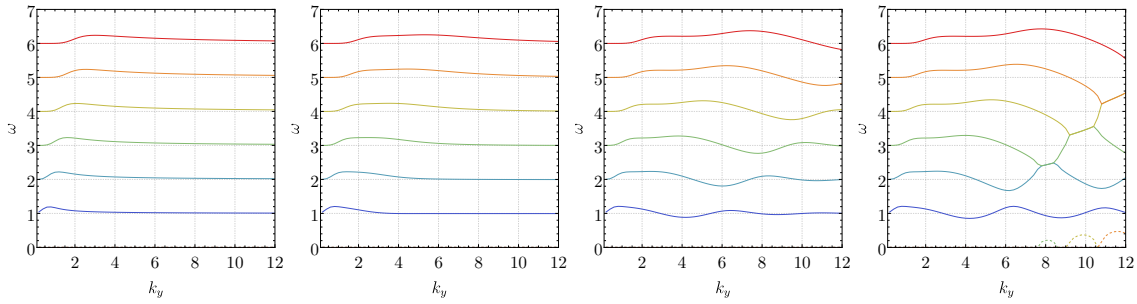

(a) $\alpha = 1$ (b) $\alpha = 10$ (c) $\alpha = 100$ (d) $\alpha = 1000$

Figure 4.12: Frequencies (solid lines) and growth rates (dashed lines) for for Gauss-ring distribution with $\tilde{v}_\perp = 0.5$ for various $\alpha = 1$(a),10(b),100(c),1000(d) (Lines of the same color correspond to the same solution)

dispersion relation for an arbitrary isotropic distribution function can be computed. As already discussed, a more general Green's function can be derived when allowing for the background distribution to have a finite $\boldsymbol{k}_\perp$, allowing the derivation the dispersion relation for an arbitrary gyrokinetic distribution function as a background. However, including the inhomogeneity of the background distribution would involve a significantly more complicated derivation as there would be a nonlinear interaction between the wave vector of the background $\boldsymbol{k}_0$ and the wave vector of the perturbation $\boldsymbol{k}$. Instead, the focus is shifted to scenarios where cyclotron instability is induced by temperature and density gradients.

4.3 Destabilization of IBWs by temperature and density gradients

After exploring the possibilities of cyclotron instabilities with ring-distributions, I want to return the focus back to more classical scenarios. In the following section, the destabilization of the ion Bernstein waves due to the presence of a temperature and density gradient is explored. The linear stability of our system described in section 3 is completely described by the dispersion relation $\omega(\boldsymbol{k})$ described by the roots of the susceptibility equation (3.1.8)

$$\chi = \frac{n_k}{\phi_k} = \left[\omega - k_y \frac{\nabla T}{T}\partial_\xi\right] \frac{1}{|k_z|}\sqrt{\frac{\xi}{2}} \sum_{p\in\mathbb{Z}} Z\left(\frac{\omega + p}{|k_z|}\sqrt{\frac{\xi}{2}}\right)\Gamma_p\left(\frac{k_\perp^2}{\xi}\right) - 2 = 0. \quad (4.3.1)$$

However, the additional presence of a density gradient is taken into account, which modifies the source term from 3.0.4 resulting in

$$\nabla_{\boldsymbol{v}} S = \hat{\boldsymbol{z}} \times \nabla S^\circ + \nabla_{\boldsymbol{v}} S^\circ = \hat{\boldsymbol{z}} \times \left[\frac{\nabla T}{T}\left(\frac{v^2}{2} - \frac{3}{2}\right) + \frac{\nabla n}{n}\right] S^\circ - \boldsymbol{v} S^\circ. \quad (4.3.2)$$

The dispersion relation with both gradients reads

$$0 = \left(\omega - k_y \times \left[\frac{\nabla T}{T}\frac{\partial}{\partial\xi} + \frac{\nabla n}{n}\right]\right) \frac{\sqrt{\xi}}{\sqrt{2}|k_z|} \sum_{p\in\mathbb{Z}} Z\left(\frac{\omega + p}{|k_z|}\sqrt{\frac{\xi}{2}}\right)\Gamma_p\left(\frac{k_\perp^2}{\xi}\right) - 2. \quad (4.3.3)$$

In the first section, a stability criterion is derived, using the Cauchy argument principle. In the second part, cyclotron instability is simulated with BSL6D code and investigate the growth rates and frequencies of the IBWs at various wave numbers.

4.3.1 Stability criterion

Cauchy argument principle Before deriving the actual criterion for the density and temperature gradient, I have the method described in section 2.3.2 of using the Cauchy argument principle to better understand the later instability. Using the argument principle helps to develop an understanding of the instability without any complicated calculations and makes later results more plausible.
Firstly, a short recap the method of studying the stability of a system using Cauchy's argument principle. Section2.3.2 has introduced the principle and I have applied the principle in section 4.2.1 to understand the stability of IBWs in the context of nonlinear ITG simulations. Cauchy's argument principle gives information about the existence of roots and poles of the complex function $f(z)$ in a domain Ω by investigating the winding number of f along the boarder $\partial\Omega$. The winding number

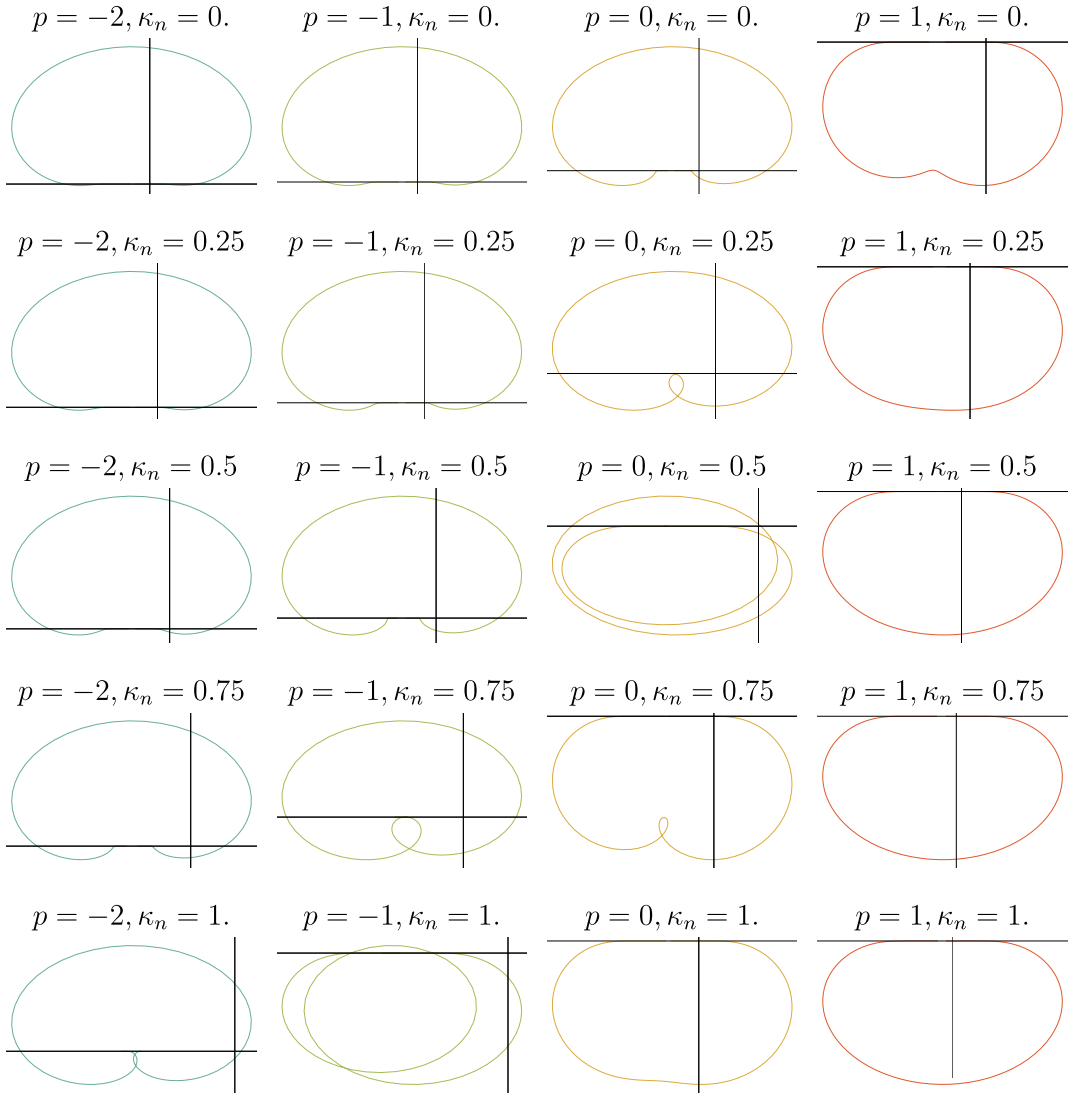

Figure 4.13: Image of a closed path ω under the map $\chi(\omega)$ from equation (4.3.1) in complex plane for $p = -2, -1, 0, 1$ (columns) and different density gradients $\kappa_n := \frac{\nabla n}{n} = 0, 0.25, 0.75, 1$ for a fixed $\kappa_T := \frac{\nabla T}{T} = 0.5$, $k_\perp = \frac{3}{2}$ and $k_z = \frac{1}{40}$. The winding number around the origin indicates the number of unstable solutions.

is given by

$$\frac{1}{2\pi i}\oint_{\partial\Omega}\frac{f'(z)}{f(z)}\mathrm{d}z = N - P, \tag{4.3.4}$$

which gives the difference between the number of roots N and the number of poles P of $f(z)$ within the domain Ω. The principle is applied to the susceptibility $\chi(\omega)$ in order to show the existence of unstable modes. $\chi(\omega)$ can be potted along a complex path $\omega \in \partial\Omega$ and visual impression of the stability is obtained about the ω in the domain Ω. In simple words, for each time the curve $\chi(\omega)$ winds around the origin of the coordinate system, the system has one solution within the domain (under the assumption that there are no poles within the domain).
The method to choose the paths $\delta\Omega$, such that cyclotron instabilities close to the various harmonics of the Larmor frequency can be isolated, is described in figure 4.4. In essence, the susceptibility can be plotted on a short path $\omega = \omega' + i\epsilon$ with $\omega', \epsilon \in \mathbb{R}$ for $\omega \in [p - 0.5, p + 0.5]$. The winding number of $\chi(\omega)$ which can be determined from the plots provides information about the stability of modes in the vicinity of the pth harmonic.
The influence of a density gradient on the stability of ion Bernstein waves is the first focus of this discussion. The stability properties of the IBWs $p \neq 0$ are compared to the properties of the low frequency ITG modes $p = 0$. A density gradient, in parallel to the present temperature gradient, acts stabilizing on the system for ion temperature gradient instabilities.
The image of $\chi(\omega)$ in the complex plane along the closed path *omega* is displayed in figure 4.13 for the harmonics $p = -2, -1, 0, 1$ and the density gradients $\kappa_n = 0, 0.25, 0.5, 0.75, 1$ for a given $\kappa_T = 0.5$, $k_\perp = \frac{3}{2}$ and $k_z = \frac{1}{40}$. Each column (and color) corresponds to the IBW close to the harmonic p, while the rows correspond to the various gradients, increasing from the top.
The first notable characteristic of these plots is the asymmetry between the image for positive and negative p. For $p > 0$, the image has a negative imaginary part which becomes increasingly negative with an increasing density gradient.
The temperature and density gradient are parallel in most system, such as the plasma edge [Bateman et al., 1998]. The plots show that the IBWs with $p > 0$ are not destabilized when the gradients are parallel.
For the ITG instability at $p = 0$ the susceptibility has a winding number of one for $\kappa_n = 0$ and with increasing gradient, the instability disappears which is expected as density gradients are known to stabilize ITG instabilities. The difference, that IBWs are unstable while ITG modes are stabilized for $\eta \sim 1$ will be important for the discussion of the relevance in of the cyclotron instability in realistic scenarios (see section 6.2).
For $p < 0$ and $\kappa_n > 0$, the system some modes are unstable (e.g. $p = -1$, $\kappa_n = 0.5$). With increasing density gradient shows that the instability disappears, similar to the case of $p = 0$.
For $\kappa_n = 0$, the curve passes so close to the origin which renders it impossible to

distinguish whether an instability is present. This issue is addressed later when discussing the results of the stability criterion.
The next step focuses on the role of the temperature gradient and its interplay with the density gradient. Hence, in figure 4.14, the image of $\chi(\omega)$ with $\omega \in [-1.5, -0.5]$ is plotted for the temperature gradients $\kappa_T = 0, 0.25, 0.5, 0.75$(columns) and gradient ratios $\kappa_n = 0, 0.25, 0.5, 0.75, 1$(rows). For reference, the third column in figure 4.14 corresponds to the second column in figure 4.13. The plots show, that neither a pure temperature gradient, first row, nor a pure density gradient (first columns) is sufficient to destabilize the ion Bernstein waves. Neither the plots in the first row, nor the first column exhibit a winding number > 0. In contrast, for the ITG modes a temperature gradient alone is sufficient to induce the instability. Increasing both gradients (going from the top left to the bottom right) eventually leads to an instability (e.g for $\kappa_T = 0.5$ and $\kappa_n = 0.5$). The mode is stabilized again, when the density gradient is increased further, at a constant temperature gradient (compare $\kappa_n = 0.5$ and $\kappa_T = 1$).

Derivation of stability criterion for density gradient Starting from the dispersion relation (4.3.3), a stability criterion is derived for the cyclotron instability. The properties of the plasma dispersion function [Poppe and Wijers, 1990] suggest that the contribution of the summands $q \neq p$ are small when studying the solution with $\omega \sim q$. Hence, a constant approximation $\omega = q$ for all summands except the resonance is assumed

$$\chi(\boldsymbol{k}, \omega) \approx \chi^q(\boldsymbol{k}, \omega) := (\omega - \boldsymbol{k} \cdot \boldsymbol{v}^*) \frac{\sqrt{\xi}}{\sqrt{2}|k_z|} Z\left(\frac{\omega - q}{|k_z|}\sqrt{\frac{\xi}{2}}\right) \Gamma_q\left(\frac{k_\perp^2}{\xi}\right) - 2 + \beta^q \tag{4.3.5}$$

with a ω independent contribution from the background

$$\beta^q := (q - \boldsymbol{k} \cdot \boldsymbol{v}^*) \frac{\sqrt{\xi}}{\sqrt{2}|k_z|} \sum_{\substack{p \in \mathbb{Z} \\ p \neq q}} Z\left(\frac{q - p}{|k_z|}\sqrt{\frac{\xi}{2}}\right) \Gamma_p\left(\frac{k_\perp^2}{\xi}\right), \tag{4.3.6}$$

and $\Gamma_p = \Gamma_p(k_\perp^2) = e^{-k_\perp^2} I_p(k_\perp^2)$. The gradients are summarized in the term $\boldsymbol{v}^* = \hat{\boldsymbol{z}} \times \left[\frac{\nabla T}{T}\frac{\partial}{\partial \xi} + \frac{\nabla n}{n}\right]$. The stability criterion is given by the gradient, for which a mode changes from stable to unstable (i.e. where the imaginary part Im $\omega = 0$ and crosses from negative to positive).
An expression for $\kappa_n = \frac{\nabla n}{n}$ is found by solving Im $\chi^q = 0$ for κ_n. It can be assumed that Im $\beta^q \approx 0$, because Im $Z(\frac{q-p}{k_z}) = \sqrt{\pi} e^{-\left(\frac{q-p}{k_z}\right)^2}$ and $k_z \ll 1$, which gives the solution

$$\kappa_n = \kappa_T \left(-\frac{k_\perp^2 \left(\frac{1}{2}\left(\Gamma_{p-1} + \Gamma_{p+1}\right) - \Gamma_p\right)}{\Gamma_p} - \frac{(p - \omega)^2}{2k_z^2} + \frac{1}{2} \right) - \frac{\omega}{k_y}. \tag{4.3.7}$$

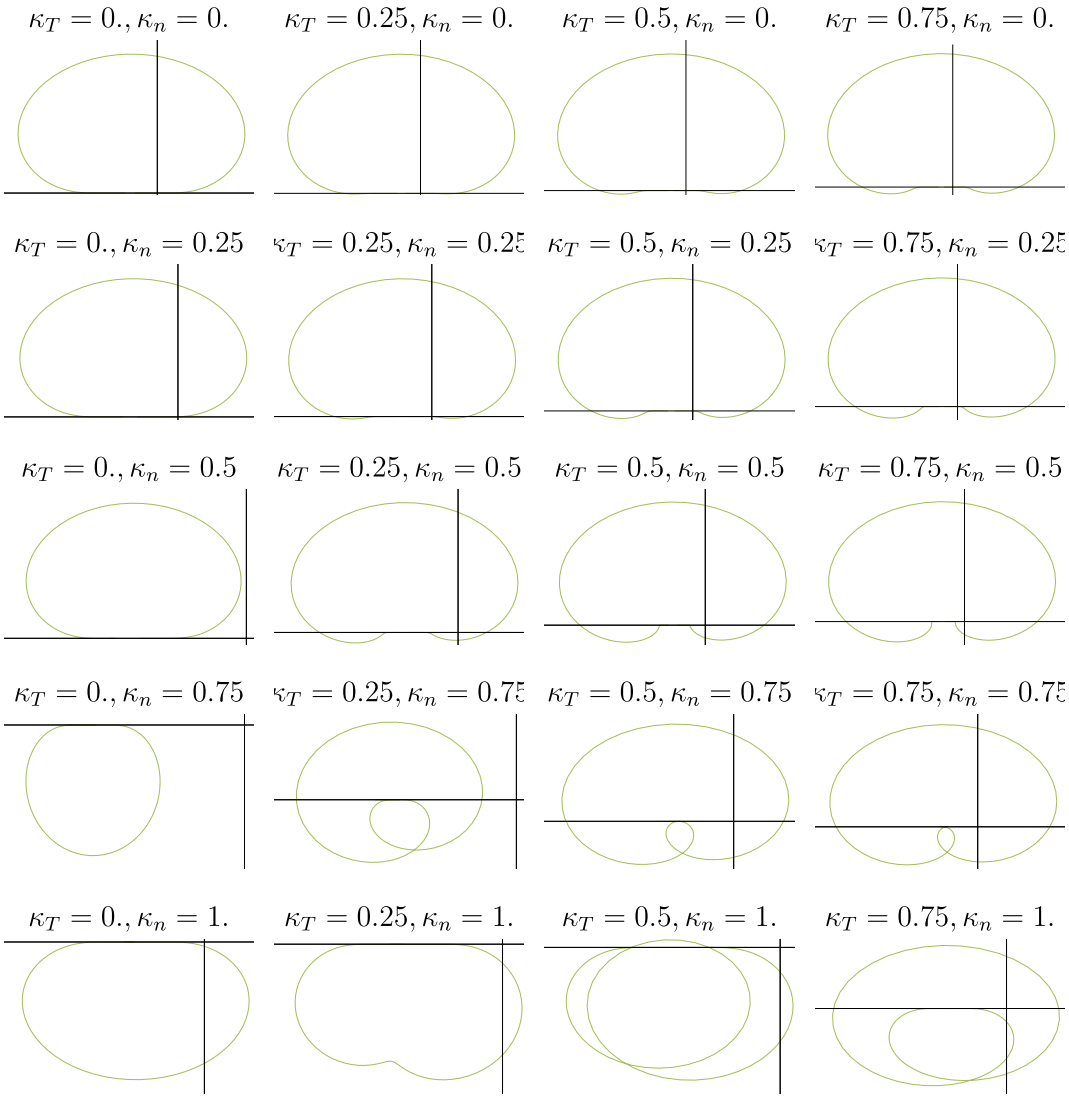

Figure 4.14: Image of a closed path $\omega \in [-1.5, 0.5]$ under the mapping $\chi(\omega)$ from equation (4.3.1) in complex plane for $\kappa_T = 0, 0.25, 0.5, 0.75$ (columns) and different density gradients $\kappa_n = 0, 0.25, 0.75, 1$ for a fixed $k_\perp = \frac{3}{2}$ and $k_z = \frac{1}{40}$

Using introducing equation 4.3.7 in the dispersion relation 4.3.5, gives the solution for ω

$$\omega = \frac{2k_z^2\left(\beta^q - 2\right)}{\kappa_T k_y \Gamma_q} + q. \tag{4.3.8}$$

Reintroducing the solution for ω in the stability condition for κ_n from equation (4.3.7) results in

$$\kappa_n = -\frac{q}{k_y} - \frac{2k_z^2(\beta^q - 2)\left((\beta^q - 2) + \Gamma_q\left(k_\perp^2\right)\right)}{\kappa_T k_y^2 \Gamma_q \left(k_\perp^2\right)^2} + \kappa_T\left(\frac{1}{2} - \frac{k_\perp^2 \Gamma'_p}{\Gamma_p}\right), \tag{4.3.9}$$

with $\Gamma'_p = -\Gamma_p + \frac{1}{2}(\Gamma_{p-1} + \Gamma_{p+1})$. A sanity check shows that the stability condition diverges for $k_y \to 0$, which is expected as the mode has to have a wave vector component perpendicular to the gradient.
The IBWs are stable with out gradients, become unstable for increasing density gradient and are stabilized for an increasing density gradient (compare figure 4.13). Hence, two solutions for the stability threshold would be expected. However, only one solution is found. This inconsistency will be discussed after comparing the stability criterion to solutions of the dispersion relation.
For a comparison I have plotted equation (4.3.9) alongside the growth rates in figure 4.15 which are determined by finding solutions ω to equation $\chi(\omega) = 0$ (4.3.3) with a numerical root finding algorithm. The growth rate Im $\omega > 0$ as the color intensity (the choice of color corresponds to the plots in figure 4.13). The expression for κ_n from equation 4.3.9 has been plotted as a red dotted line alongside and traces out the upper bound of the instability region.
The curve for the stability limit from equation 4.3.9 agrees well with the outline of the region. For the higher harmonics p, a deviation can be seen, which originates from the simplifications that are made during the derivation of the criterion. I have assumed in the derivation for the criterion of the harmonic q that the contribution of the summands $p \neq q$ are independent of ω. The accuracy of the simplification can be improved by performing a Taylor expansion include more than just the constant term.
The results agree well with the study of the instability in figure 4.13. The resonance at $p = 1$ does not show a instability for $\kappa_n/\kappa_T > 0$ (gradients point in the same direction) except for a very large temperature gradient. In the case of the resonance at $p = 0$, the instability occurs for a pure temperature gradient, while the instability disappears for an increasing density gradient. The results for $p < 0$ show that an additional density gradient is needed to destabilize the modes.
The comparison with the growth rates in figure 4.15 reveal that the stability condition $\kappa_n(\kappa_T)$ derived in equation (4.15) gives the density gradient which stabilizes the instability. For a better understanding of the behavior for small density gradients, the growth rates for a fixed temperature gradient, with an increasing density gradient are displayed in figure 4.16. In each plot, I have displayed the growth rate of the cyclotron instability close to the harmonic p for various κ_T. A log-scale has been

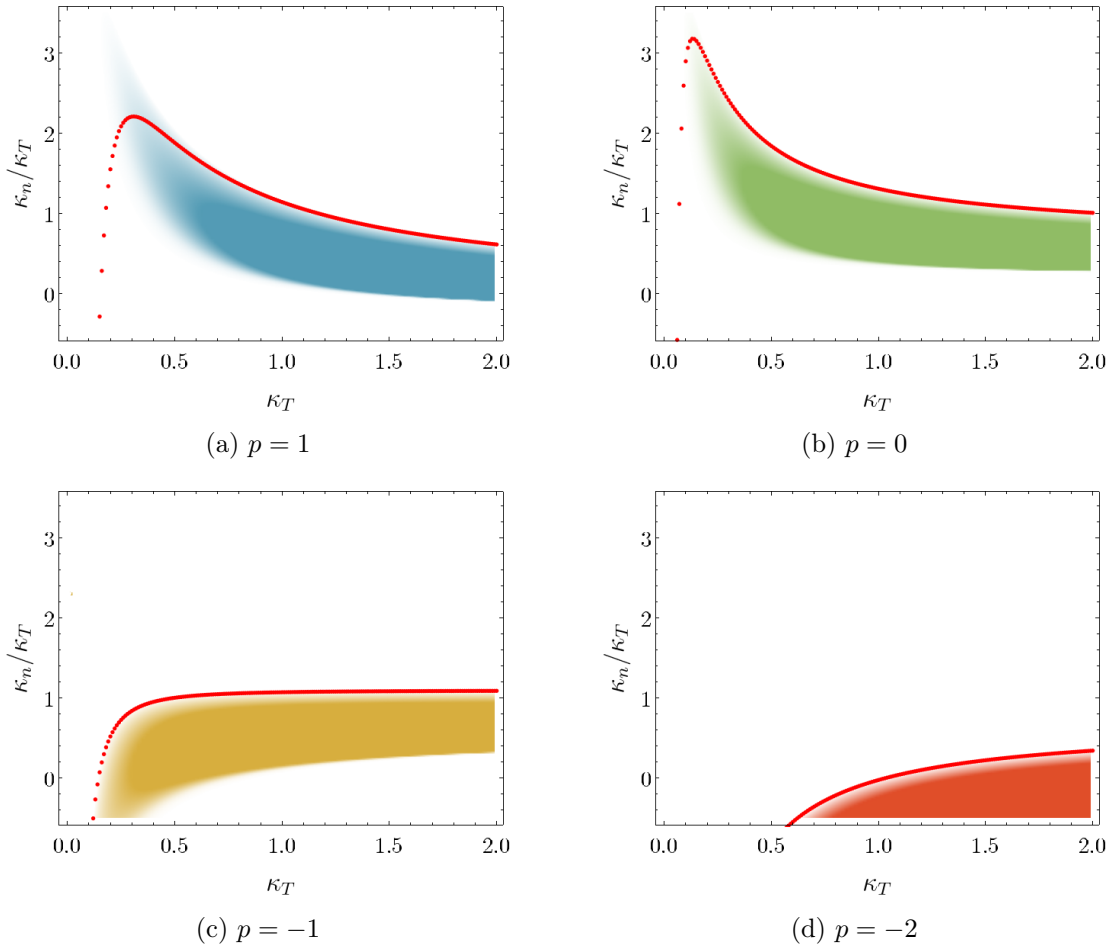

(a) $p = 1$ (b) $p = 0$

(c) $p = -1$ (d) $p = -2$

Figure 4.15: Comparison of the numerically determined stability criterion $\kappa_n(\kappa_T)/\kappa_T$ (4.3.7) (red dots) and regions of instability computed numerically from the dispersion relation (4.3.3) (colored regions) for various harmonics p ($k_\perp = \frac{3}{2}$, $k_z = \frac{1}{40}$)

used to observe the behavior of the instability at the lower bound of the stability region. The plots show that the growth rates decay but do not have a zero crossing. For small density gradients, the instability effectively vanishes, however, the modes do not experience a negative growth rate. This explains, why in the derivation above no stability criterion for the lower bound was found because no solutions with Im $\omega = 0$ exist that separate stable from unstable regions.

Derivation of stability criterion for temperature gradient After obtaining a stability condition for the density gradient in equation 4.3.9, I have derived a stability threshold for the temperature gradient, which is performed after the same logic. Equation (4.3.5) Im $\chi = 0$ is solved for the κ_T and the result is used to find an expression for ω by solving $\chi(\omega) = 0$ under the assumption $\omega \in \mathbb{R}$. which is then used to find an expression for κ_T. The derivation and the resulting condition involves

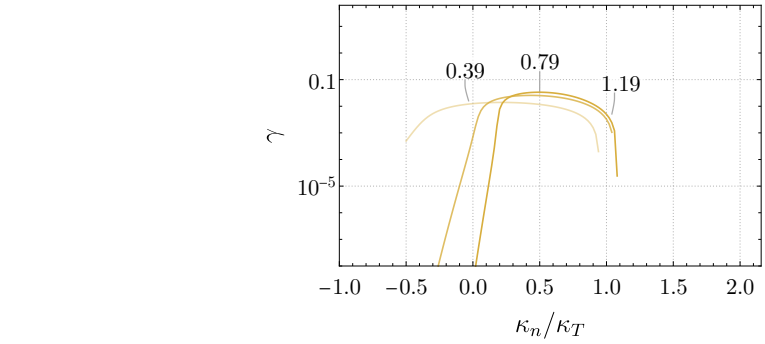

(a) $p = -2$

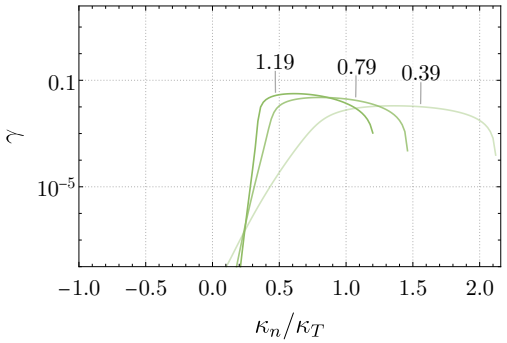

(b) $p = -1$

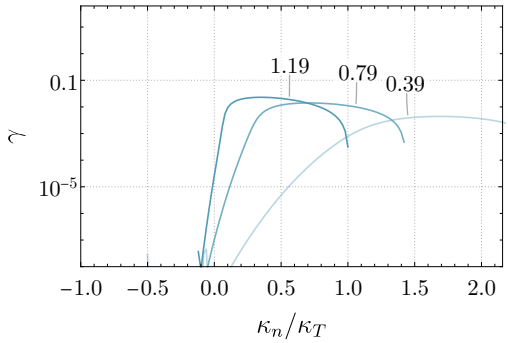

(c) $p = 1$

Figure 4.16: Growth rate of the cyclotron instability for different resonances p at fixed temperature gradient (indicated by labels) as a function of the density gradient

very lengthy expressions, which have been performed with Wolfram Mathematica [Wolfram Research, 2021]. The expression for the stability limit of the temperature gradient κ_T will not be stated here explicitly, however its properties are discussed. Similar to the density threshold before, figure 4.17 shows the stability threshold for the temperature gradient $\kappa_T(k_\perp, \kappa_n)$ alongside the growth rate.

The derived stability condition for the temperature gradient traces out a lower limit of the instability region. The plots for $p = 0$ show that an increase in the density gradient also increases the temperature gradient required for the destabilization.
The results show that the solution with positive $p > 0$ is destabilized, when the gradient is selected large enough, however the threshold increases when a present density gradient is present. A significant growth in the IBWs for the solutions with $p < 0$ is observed, even for small gradients $\kappa_T \sim 0.2$. An increase in the density gradient lowers the stability threshold for the temperature gradient. The results in the first row (with $\kappa_n = 0$) show that a pure temperature gradient can be sufficient to induce the cyclotron instability. Furthermore, one recognizes that instability resides in two separate regions, one for low $k_\perp$ and large gradients, and another for smaller gradients at larger $k_\perp$. The wavenumber tested in the discussion in figure 4.14 has been $k_\perp = \frac{3}{2}$ which is in between the two regions which explains that no instability

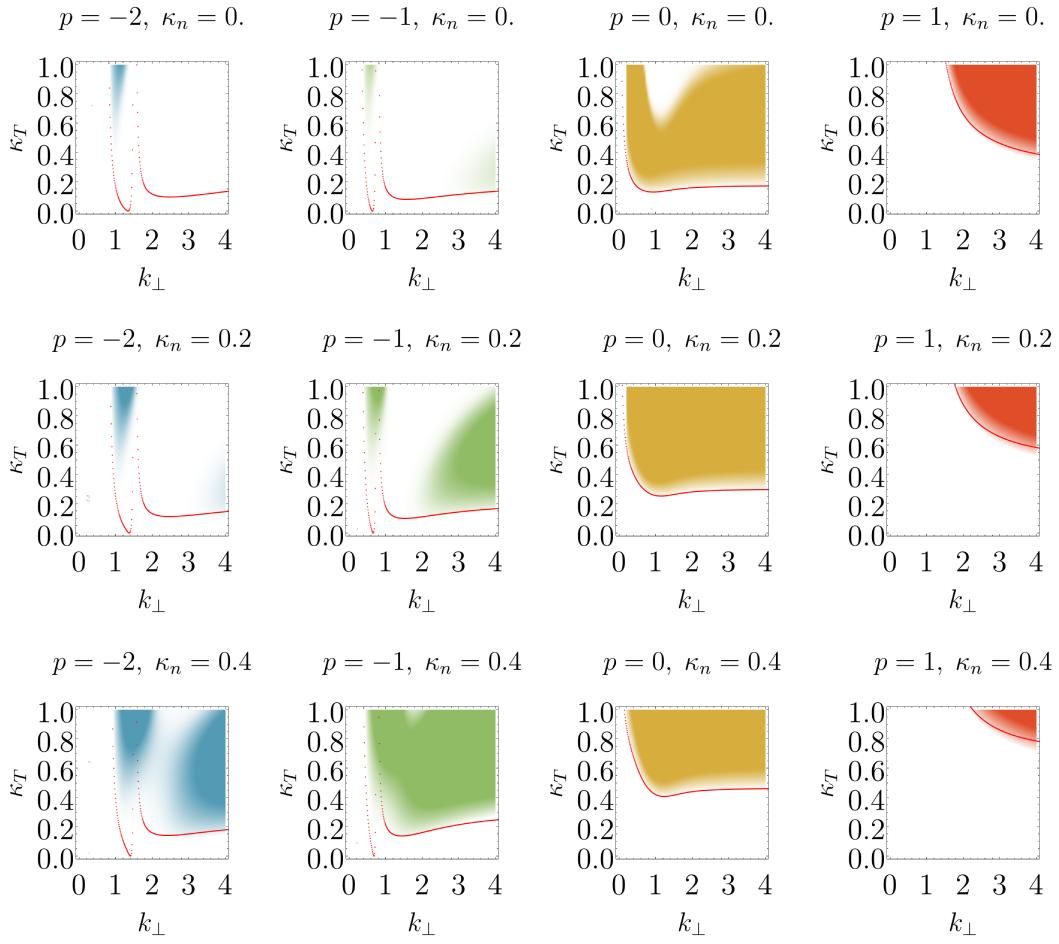

Figure 4.17: Stability criterion of the cyclotron instability for the temperature gradient $\kappa_T(k_\perp, \kappa_n)$ (red line) in comparison to the growth rate determined from the dispersion relation $\chi(\omega, k_\perp)$ for different density gradients (rows) and harmonics p (columns and colors)

is found in the first row of figure 4.14.
A qualitative difference exists between the threshold of the density and the temperature gradient. In in case of the density gradient, the instability has an infinitesimal growth rate $\operatorname{Im}\omega \gtrsim 0$ and increases exponentially an increase in the density gradient, whereas for the temperature gradient the growth rate is negative and has a clear threshold where the system becomes unstable. The difference is explained by the different behavior of the source term

$$\nabla_{\boldsymbol{v}} S^{\kappa_n} = \hat{\boldsymbol{z}} \times \frac{\nabla n}{n} S^\circ, \tag{4.3.10}$$

$$\nabla_{\boldsymbol{v}} S^{\kappa_T} = \hat{\boldsymbol{z}} \times \frac{\nabla T}{T} \left(\frac{v^2}{2} - \frac{3}{2} \right) S^\circ. \tag{4.3.11}$$

Compared to the source of the density gradient, which is a strictly monotonous decreasing function, the temperature gradient has a change in the sign at $v_\perp = \sqrt{2}$ which can lead to instabilities (compare to the discussion of the Penrose criterion in section 2.3.2).

4.3.2 Simulation cyclotron instability

Dispersion relation

After studying the stability of the IBWs, and gaining an understanding of the cyclotron instability, I have simulated the cyclotron instability with the BSL6D code [Kormann et al., 2019]. The knowledge gained from the analytical studies has been used to select a set of parameters for which the IBWs are linearly unstable. By choosing a sufficiently large density gradient parallel to the temperature gradient, the ion temperature mode is suppressed and the cyclotron instability is the only instability. The source term has been added to the code that introduces a density gradient in local treatment in addition to the temperature gradient already used for the simulation of the ion temperature gradient instability 3.1. The full gradient source term reads

$$\nabla_{\boldsymbol{v}} S = \hat{\boldsymbol{z}} \times \left[\frac{\nabla T}{T} \left(\frac{v^2}{2} - \frac{3}{2} \right) + \frac{\nabla n}{n} \right] S^\circ - \boldsymbol{v} S^\circ. \tag{4.3.12}$$

The parameters for the gradients are

$$\kappa_n = \frac{\partial_x n}{n} = 0.44; \qquad \kappa_T = \frac{\partial_x T}{T} = 0.36. \tag{4.3.13}$$

The focus of the experiment is to study the dependency of the growth rate and the frequency on the wavenumber k_y perpendicular to the gradient. The dispersion relation is determined independently for the various IBWs close to the harmonic p of the Larmor frequency. A resolution in configuration space with $N = 16 \times 256 \times 8$ has been chose chosen for a box with length $L = \pi \times 4\pi \times 80\pi$. The simulation has been performed with a time step of $\Delta t = 0.008$. The full list of parameters can be found in the appendix B.3.2. The dispersion relation is determined by computing the spatial Fourier transform of the electrostatic potential and determining the growth rate and angular frequency of the modes. The results are displayed in figure 4.18. The left plot shows the growth rate Im ω, while the right plot shows the shift of the frequency Re ω of the modes relative to the corresponding harmonic of the Larmor frequency Re $\omega - p$.

The branches of the IBWs at different harmonics p of the Larmor frequencies have similar growth rates. However, the maxima of the growth rates is at higher $k_\perp$ for larger p. Furthermore, the observations from figure 4.17 confirm that instability has two stability regions.

The frequencies of the modes are all shifted slightly to the negative compared to the harmonic of the Larmor frequency (i.e. the absolute value is larger that the

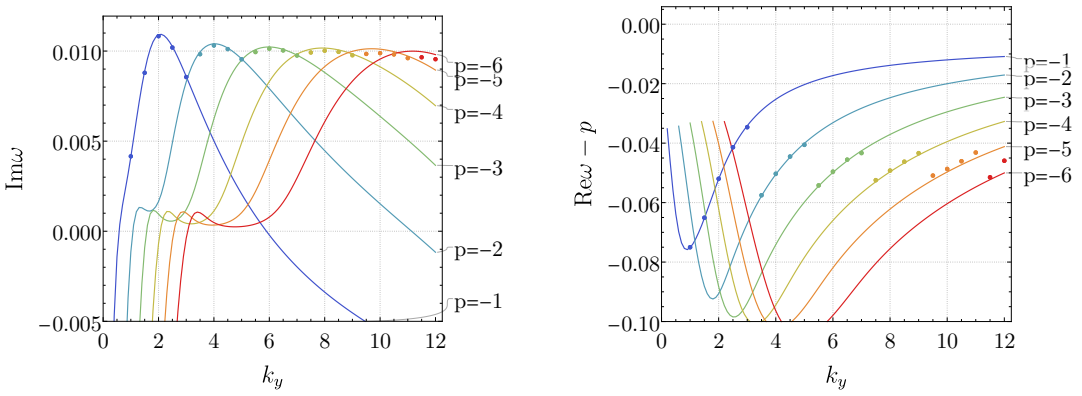

Figure 4.18: Dispersion relation for linearly unstable IBWs: Growth rate (a) and frequency shift Re $\omega - p$ (b) as a function of the perpendicular wavenumber for various p (colors) from BSL6D simulations (dots) and solutions of the analytical dispersion relation 4.3.3 (lines)

harmonic p). The stable IBWs show a similar behavior, where the absolute value of the frequencies are also slightly higher than the harmonic of the Larmor frequency. Overall, a very good agreement between the simulated and analytically computed results can be observed. The data from the simulation originates all from one singular run. Multiple modes with different frequencies for the same wavenumber are difficult to separate, thus, the plot only shows the dominant modes. Thus the simulated results trace out the upper boundary of the combined branches $\max_p \mathrm{Im}\ \omega$. The frequencies at larger wave number deviate from the analytical results. Part of the mismatch is the damping rate caused by the interpolation (compare section 2.6.3) which has already been discussed in the example of the ITG instability (section 3.1). However, the numerical diffusion leads to a lowering of the growth rate, whereas here, a divination of the frequency is seen while the growth rate stays accurate. An assumption is, that shift is caused by a lack of resolution in velocity space. Section 2.4 has shown that the IBW with $\omega \sim n$ corresponds to nth Fourier mode of the velocity angle of the distribution function, when written in gyrocenter coordinates. Together, with added complexity from the gyrotransformation to particle coordinates, the velocity distribution for the higher IBWs very fine structures. Figure 4.19(a) illustrates a velocity distribution in v_x-v_y-plane for a mode with $\omega \sim 6$ and $k_\perp = 12$. As a comparison, figure 4.19(b) shows the same distribution function displayed with the velocity space resolution that has been used in the simulation of the dispersion relation in figure 4.18.

With $N_v = 32 \times 32 \times 32$, only a finite number of cyclotron harmonics can be resolved. Especially, when the structures resides at low $v_\perp$. The fact that these modes can still be reproduced correctly by the code and same growth rates are achieved as is in the analytical dispersion relation is attributed to the very effective treatment of the $\boldsymbol{v} \times \hat{\boldsymbol{z}}$ acceleration term by the rotation velocity grid. In traditional semi-Lagrange

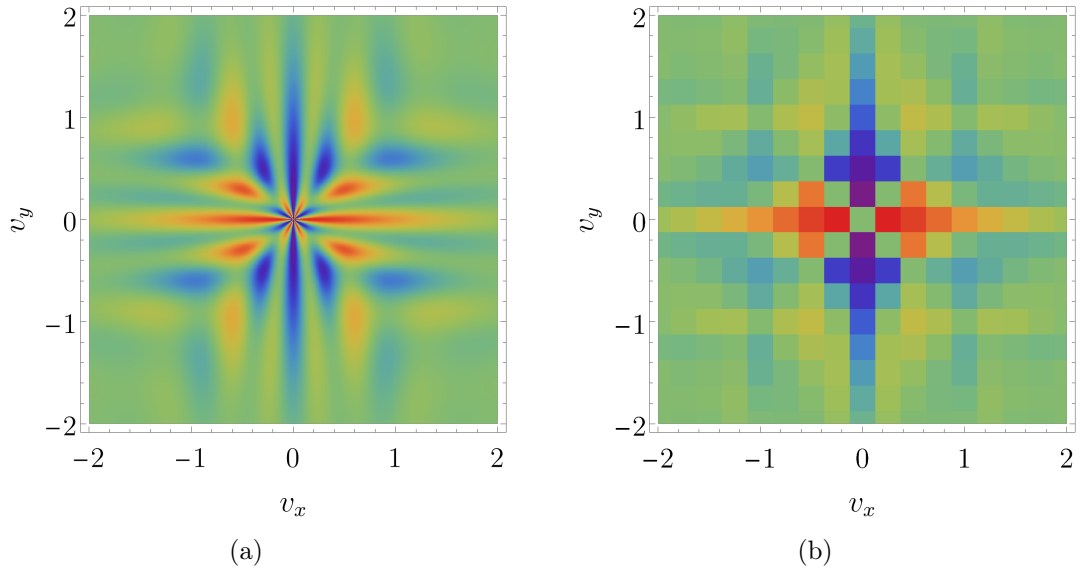

Figure 4.19: Illustration of velocity distribution with mode number $m = 6$ and $k_\perp = 12$ in particle coordinates in the v_x-v_y-plane displayed as analytical function (a) and discrete function (b) with resolution used in the simulation the simulation

methods, the advection along the $\boldsymbol{v} \times \boldsymbol{B}$ part of the characteristic is computed by the same interpolation method as for the electric field which leads to a significantly stronger numerical diffusion in velocity space.
6D kinetic simulations of the cyclotron instability with a temperature gradient have not been shown before. The simulations have confirmed the analytical prediction of the cyclotron instability in for steep temperature and density gradients, and thus, has strengthened the confidence in the existence of unstable ion Bernstein waves. The system that has been studied is a limited physical model, because a slab geometry and adiabatic electrons is assumed. However, the slab ITG instability is a weak instability compared to other ion temperature gradient driven modes. In analogy to the to the ITG instability, one can suspect that cyclotron instabilities are also relevant in scenarios with magnetic field curvature and gradients.

Quasi-linear energy transport of IBWs

The goal of this section is to determine the energy fluxes for the ion Bernstein waves, which have been derived in section 3.2 and compare them to the fluxes in the simulations with the BSL6D code.The energy flux consists of three contributions, the Poynting flux $\boldsymbol{S} = \phi\boldsymbol{\Gamma}$, the $\boldsymbol{E} \times \boldsymbol{B}$-heat flux $\boldsymbol{Q}^{\boldsymbol{E}\times\boldsymbol{B}} = -\nabla\phi \times \boldsymbol{B}\epsilon$ and the stress tensor induced energy flux $\boldsymbol{Q}^{\boldsymbol{\Pi}} = -(\boldsymbol{\Pi} \cdot \nabla\phi) \times \boldsymbol{B}$. The stress tensor energy flux and the Poynting flux cancel in the gyrokinetic limit because the $\boldsymbol{E} \times \boldsymbol{B}$ heat flux is the only energy flux present in a gyrokinetic system. Simulations with the BSL6D code have verified that the two contributions cancel (compare in figure 3.2).
The expression which has been derived in section 3.2 can be used without modifi-

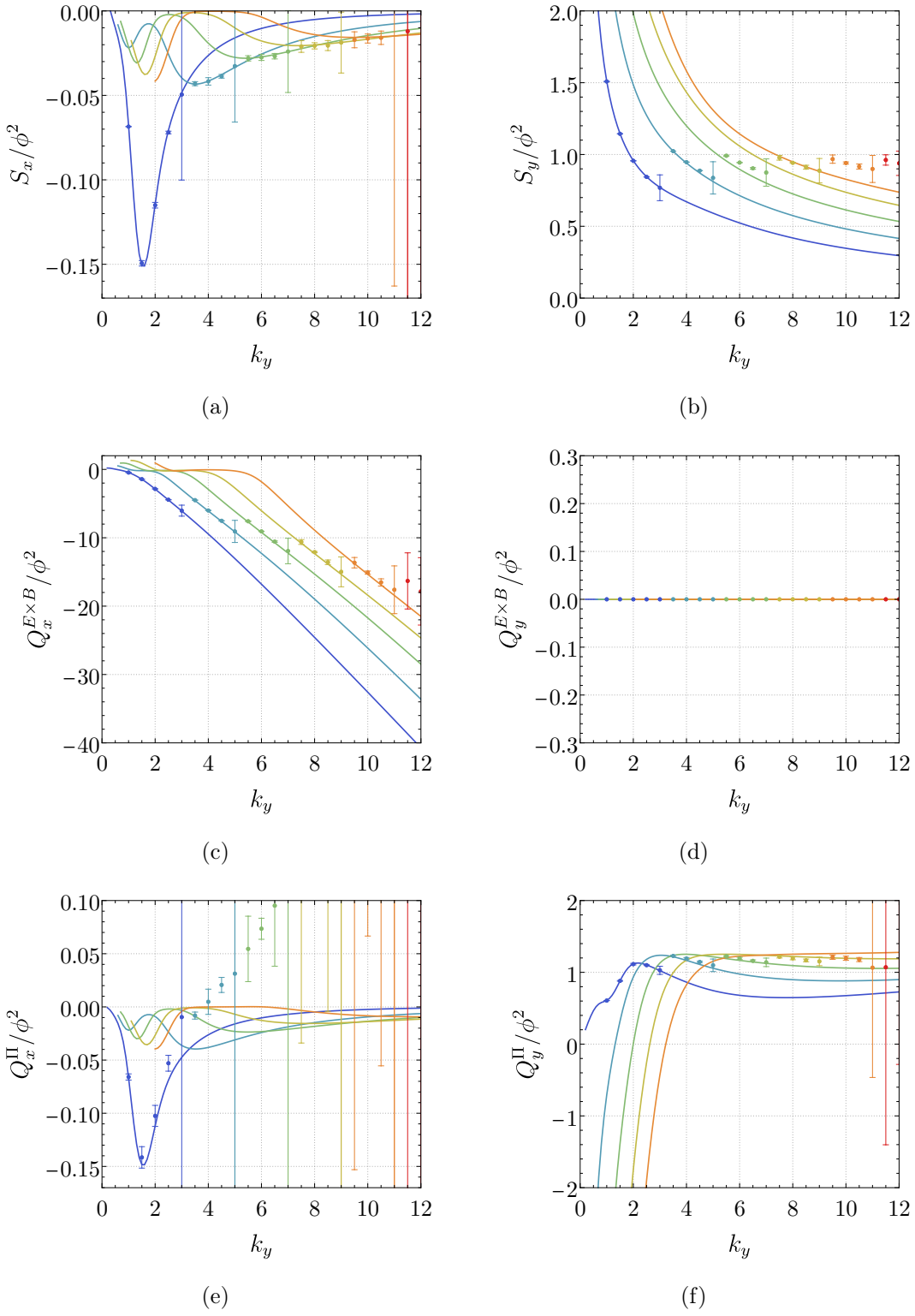

Figure 4.20: Quasi-linear energy fluxes $\boldsymbol{S}$ (a,d), $\boldsymbol{Q}^{\boldsymbol{E}\times\boldsymbol{B}}$ (b,e) and $\boldsymbol{Q}^{\Pi}$ (c,f) for unstable ion Bernstein waves. The analytical results (lines) have been computed with the expression which have been derived in section 3.2. The simulated data (points) has been averaged and the standard deviation is given by the errorbars (color indicate different frequencies, compare 4.18) .

cation for the computation of the IBW fluxes. The energy flux has been computed for every harmonic p individually and the results have been displayed in figure 4.20 for the two directions perpendicular to the magnetic field.
The first notable observation is, that the values for the energy fluxes parallel to the gradients have different orders of magnitude. The $\boldsymbol{E} \times \boldsymbol{B}$ heat flux is $\sim 100\times$ larger than the other two contributions. Furthermore, in the case of non-gyrokinetic modes, the Poynting flux S_x (a) and stress tensor induced energy flux $Q_x^{\mathfrak{ß}}$ (c) have the same absolute value in the direction of the gradient. In section 3.2, a intuitive explanation is given, why the energy flux in the magnetic field (the Poynting flux) is expected to balance the energy flux induced by the stress tensor. The energy flux dominated by the $\boldsymbol{E} \times \boldsymbol{B}$ heat flux in x-direction. The $\boldsymbol{E} \times \boldsymbol{B}$ heat flux is zero in y-direction for modes with $k_x = 0$. The Poynting flux and the stress induced energy flux show are similar in magnitude but show quite different behavior, especial in the limit of small wave numbers. The physical interpretation of this result is still under investigation.
The energy fluxes have been determined from simulations with the BSL6D code. Various diagnostics ($\epsilon = \int \frac{v^2}{2} f \mathrm{d}^3 v$, $\mathbf{\Gamma} = \int \boldsymbol{v} f \mathrm{d}^3 v$ and $\mathbf{\Pi} = \int \boldsymbol{v}\boldsymbol{v} f \mathrm{d}^3 v$) have been implemented in the code, from which the different contributions to the total energy flux can be computed. The parameter for the simulation of the energy fluxes are the same as for the computation of the distribution function in section 4.3.2. However, for these simulations, the nonlinearity has to be activated to correctly reproduce the higher moments of the distribution function. The full set of parameters can be found in the appendix under B.3.2.
The energy flux contribution have been Fourier transformed and the modes normalized to the square of electrostatic potential and have been averaged over a time period of $T = 400$. The mean values and the standard deviation are displayed as the points and error bars in figure 4.20. The color of the points is given by the frequency of the mode according to the same color scale as the harmonic p of the lines. The fluctuations over time of the energy fluxes varies between the different modes. Especially for higher wavenumbers, the values for the energy fluxes are difficult to determine because of large noise levels. Figure 4.18 shows that for some wavenumbers in the simulation, two branches of the dispersion relation intersect (i.e. $k_y = 3, 5, 7$). At these points, two neighboring IBWs have the same growth rate. The values of the energy fluxes oscillate strongly over time because of the superposition of the two neighboring modes. This is shown in the graphs in figure 4.20 by the larger error bars at these wave numbers. In summary, the overall agreement between the energy fluxes from the simulation and analytical results computed from the expressions in section 3.2 are in very good agreement. Especially for the $\boldsymbol{E} \times \boldsymbol{B}$ heat flux, all the analytical energy flux lays within the errorbars of the simulated results. The results for the energy flux caused by the momentum flux tensor parallel to the gradient (4.20(c)) fluctuate too strongly to be useful. The Poynting flux S_y is overestimated by a few percent but still follows the overall trend of the analytical calculation.

For a comparison between the energy transport caused by ITG modes and the IBWs,

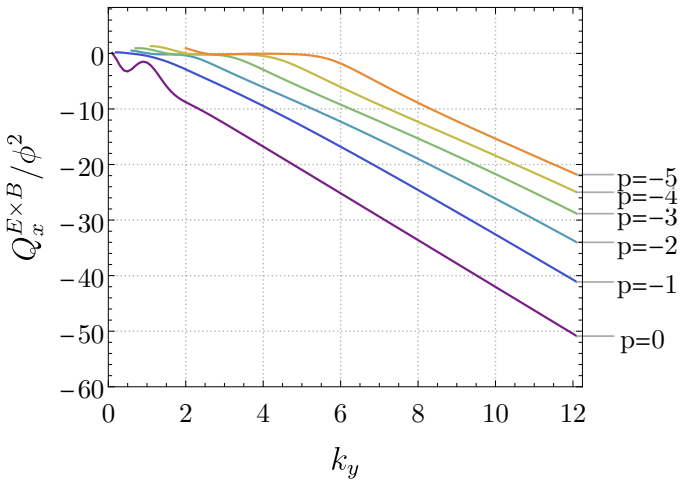

Figure 4.21: Comparison of the $\boldsymbol{E} \times \boldsymbol{B}$ heat flux $\boldsymbol{Q}_x^{\boldsymbol{E}\times\boldsymbol{B}}$ for the different harmonics p in the direction of the gradient

the $\boldsymbol{E} \times \boldsymbol{B}$ heat flux is discussed, because it is the the dominant contribution to the energy transport in the direction of the gradient. The fluxes for various harmonics have been displayed in figure 4.21. The discussion focuses on the harmonics with negative p as the studies in section 4.3.1 have shown that modes with $p < 0$ are most relevant for the cyclotron instability. The plots show that in the limit of large k_y the heat flux is proportional to the wavenumber k_y. For a given wave number the energy transport induced by modes with lower frequencies is larger compared to modes with larger frequencies. However, the discussion of the dispersion relation of the unstable IBWs (compare figure4.18) has shown, that the modes with larger mode number reside at larger wave numbers, as their peak growth rate is at higher $k_\perp$. In the example shown in figure 4.18(b), the majority of the transport is carried by the mode with $p = -6$. The comparison suggests that in scenarios where the ITG modes and IBWs have similar fluctuation level, that the Bernstein waves have a significant contribution to the energy flux in the system.

4.3.3 Nonlinear saturation of the cyclotron instability

Section 4.3.2 and 4.3.2 focused on the linear instability of the cyclotron instability. However, the BSL6D is capable of simulating of the cyclotron instability until the non-linearity becomes relevant and the system starts to saturate. A domain with $N = 64 \times 64 \times 16$ and $L = 4\pi \times 4\pi \times 80\pi$ have been used for the simulation of the nonlinear saturation. The other parameters are the same as in the simulation in section 4.3.2. The full set of parameters can be found in the appendix B.3.3.
The root mean square (RMS) of the electrostatic potential is plotted in figure 4.22(a). After an initialization phase ($t < 500$), the unstable modes grow exponentially ($500 < t < 1500$). When the perturbation becomes large enough ($t \sim 1500$), the nonlinear term becomes relevant and the perturbation saturates. The RMS of the electrostatic potential levels out at RMS(ϕ) ~ 0.02.

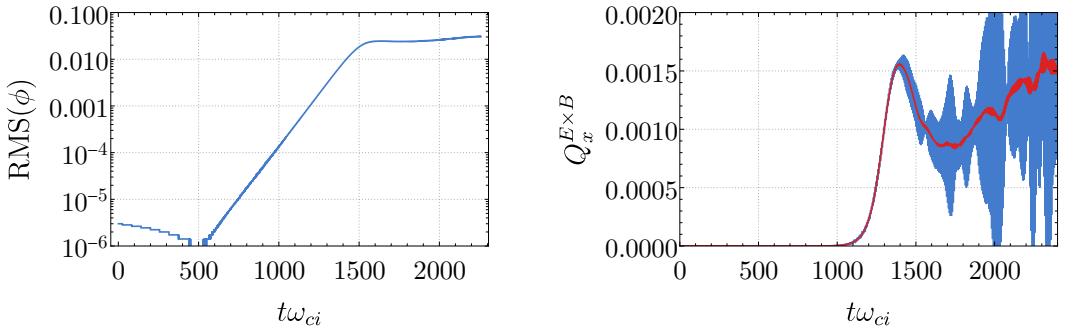

Figure 4.22: Root mean square of the electrostatic potential in nonlinear simulation of cyclotron instability (a) and $\boldsymbol{E}\times\boldsymbol{B}$ heat flux $Q_x^{\boldsymbol{E}\times\boldsymbol{Q}}$ (moving average with period of $t = 6$ is overlaid in red)

In addition to the electrostatic potential, the $\boldsymbol{E}\times\boldsymbol{B}$ heat flux in the opposing direction of the gradient in figure 4.22(b). The simulation shows nonlinear energy transport in the direction of the gradient. The energy flux is highly intermittent. Hence, a moving average with a window of $T = 6$ has been computed, and overlaid the result in red. The averaging period is close to the Larmor period and thus, removes the majority of the high frequency oscillations. The significance of the energy flux is difficult to evaluate. The energy flux is proportional to the square mean of the electrostatic potential amplitude. The ratio between the two quantities is displayed in figure 4.23. The ratio saturates a $Q^{\boldsymbol{E}\times\boldsymbol{B}}/\phi^2 \sim 1$, which is a factor four larger that the ratio between energy flux and square mean which has been in the turbulent energy transport in the ITG simulations in figure 3.4. IBWs produces four times the amount of energy transport compared to the ITG modes, when the electrostatic potential amplitude is the same.
Figure 4.24 shows snapshots of the electrostatic potential for different times t. The simulation is initialized with a white noise, at $t = 0$, one can already recognize the developing mode structure of the cyclotron instability. At the end of the linear phase ($t = 1500$), the plot (b) shows that the mode $\boldsymbol{k} = \left(0, 2, \frac{1}{40}\right)$ has the largest growth rate. The last snapshot ($t = 2500$) shows the fully developed ion Bernstein wave turbulence.
The simulations presented in this work are the first time 6D kinetic simulations of ion temperature gradient drives modes have been performed with of gradients of this steepness. Without having another simulation tool at hand which allows us to compare the nonlinear results with, makes a quantitative verify the simulation results. A comparison with a nonlinear 6D particle in cell Vlasov code based on the GEMPIC framework [Kraus et al., 2016] is planned for future work.

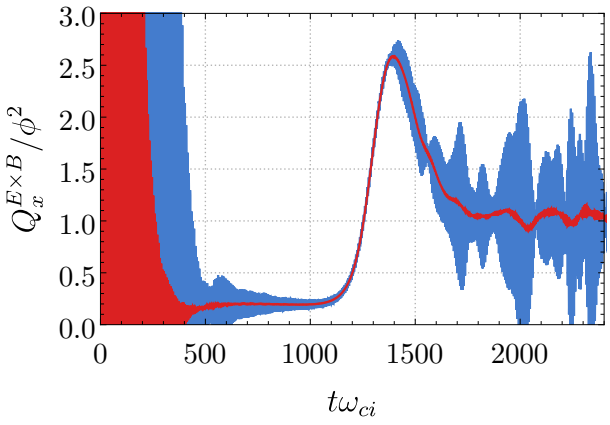

Figure 4.23: Ratio of $\boldsymbol{E}\times\boldsymbol{B}$ heat flux $Q_x^{\boldsymbol{E}\times\boldsymbol{Q}}$ and RMS(Œ)^2 in nonlinear simulation of cyclotron instability (moving average with a window of $T = 6$ is overlaid in red)

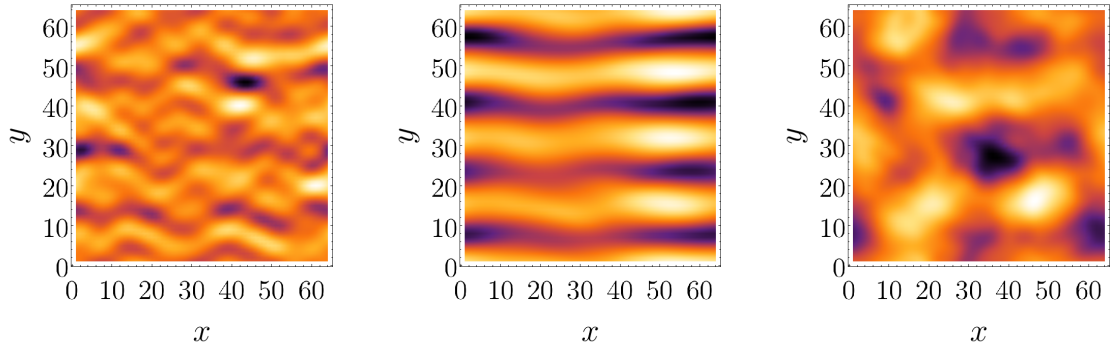

(a) $t = 500$ (b) $t = 1500$ (c) $t = 2500$

Figure 4.24: Snapshots of the electrostatic potential in nonlinear simulation of cyclotron instability at $t\omega_c i = 500$(a), 1500(b), 2500(c)

4.4 Summary

The first section focuses on the verification of our simulation code with the dispersion relation of the stable ion Bernstein waves. The existence of these waves is known since their their first description in 1958 [Bernstein, 1958]. The simulations which have been performed in this section have demonstrated the capability of the BSL6D code of simulating waves with frequencies beyond the gyrokinetic regime.
In this work, the term 'cyclotron instability' is used for unstable ion Bernstein waves independent of the driving mechanism for the instability. The ITG simulations which have been used for the verification of or code in the gyrokinetic regime have shown the presence of fast oscillating modes in the nonlinear phase. Section 3.3 discusses that the temperature gradient source used for the simulations can cause local regions with negative phase space densities. Section 4.2.1 shows that these negative phase space densities can lead to the instability of IBWs. The fact that the neg-

ative phase space densities in the simulations with local gradients gives a possible explanation for the high frequency waves that have been witnessed in the nonlinear ITG simulations with the BSL6d code and by others in literature [Sturdevant et al., 2016]. In the case of the ITG instability, the fluctuations become large and the requirements for local treatment of the gradients has limited validity and the that 6D kinetic simulation results have to be carefully evaluated. A possible improvement of the simulations is the nonlinear treatment of the temperature gradient. The effects of switching from a local representation to a nonlinear treatment are discussed in chapter 5.

After I have demonstrated that the ion Bernstein wave can be destabilized by negative phase space densities, the investigation has shifted to other scenarios in which the cyclotron instability occurs. Very few studies have been performed on the instability of ion Bernstein waves. Examples can be found, where a ring perturbation has been used to destabilize the modes [Yoon et al., 2014, Noreen et al., 2019]. In the section 4.2.2, the same ansatz has been chosen as in the mentioned publications. A stability criterion for cyclotron instability has been derived. In section 4.2.2, as well as in both papers, the source term has been considered to be a ring $\boldsymbol{k} \cdot \nabla_{\boldsymbol{v}} S = \gamma k_\perp \delta(v_\perp - \tilde{v}_\perp) f_M(v_\perp, v_z) + \boldsymbol{k} \cdot \nabla_{\boldsymbol{v}} f_M$ in velocity space. This is a simplification of the system. The velocity gradient of a distribution function cannot be an isotropic function.

Hence, a dispersion relation for a more realistic source has been derived in section 4.2.3. All gyrokinetic distribution functions are isotropic with respect to the velocity angle when the distribution function is expressed in gyrocenter coordinates. The velocity gradient of an isotropic distribution function has the mode number $m = 1$. In section 4.2.3, a dispersion relation has been derived for the δ-ring distribution function $S^\circ = \gamma f_M(\tilde{v}_\perp, v_z)\delta(v_\perp - \tilde{v}_\perp)$. Introducing the source $\boldsymbol{k} \cdot \nabla_{\boldsymbol{v}} S^\circ$ into the dispersion relation leads to a lower instability threshold compared to the case in section 4.2.2, where the velocity gradient of the background has been assumed to be isotropic.

The derivation of the dispersion relation is based on deriving the linear response for a given background distribution. An advantage of using a δ-function is that the derived dispersion relation can be used as a Green's function to compute the dispersion relation for an arbitrary isotropic background distribution function. I have shown this property for the example of a Gaussian ring distribution.

The derivation performed in the chapter assumes that the background distribution is homogeneous in the position space. The framework can be extended by including the influence of a finite wavenumber of the background distribution. With a finite wavenumber of the background distribution function, the gyrotransformation can not be neglected which makes the calculation significantly more complex.

A different path has been chosen for the continuation of this work. The influence of temperature and density gradients on the stability of the ion Bernstein waves has been studied. I have derived a stability criterion for both the density and temperature gradient and have showed that the IBWs can be destabilized with sufficiently steep temperature and density gradients.

The cyclotron instability have caused significant growth rates which can exceed the growth rate of the ITG instability. In particular, the discussion in section 4.3 has shown, that an density gradient parallel to the temperature gradient can favor the cyclotron instability over the ITG instability.
The result that the IBWs are destabilized for $\eta \sim 1$ makes the cyclotron instability an interesting instability for the plasma edge scenario, especially in the H-mode, where steep temperature and density gradients coincide. Apart from analytical consideration, simulations of the cyclotron instability with the BSL6D code have been performed. The simulations have verified the analytically derived dispersion relation as well as the predicted energy fluxes in the linear regime.
The agreement between the analytical and simulated results in the linear regime provide confidence that the BSL6D code correctly describes turbulence in magnetically confined plasmas with steep gradients. Section 4.3.3 shows an example of a turbulence simulation, in which the cyclotron instability is the driving mechanism. The ratio of the energy flux in the direction of the gradient and the square mean of the electrostatic potential $Q_x^{\boldsymbol{E}\times\boldsymbol{B}}/\phi^2 \sim 1$ shows that the IBW turbulence produce a significant energy transport.

Chapter 5

Simulations with nonlinear treatment of gradients

The tests in section 3.3 showed that a local treatment of the temperature gradient can cause significant issues in 6D kinetic simulations. The source term which introduces the gradient into the system does not preserve the positivity of the distribution function. Local negative phase space densities can be caused, which lead to the excitation of high frequency ion Bernstein waves (compare section 4.2.1). This section moves away from the local treatment and move towards a nonlinear treatment of the gradients in our simulation code. The initial condition in the simulation is chose such that the distribution function can have a density and temperature profile

$$f_0(\boldsymbol{r},\boldsymbol{v}) = \frac{n(\boldsymbol{r}-\boldsymbol{\rho})}{(2\pi T(\boldsymbol{R}))^{\frac{3}{2}}} e^{-\frac{v^2}{2T(\boldsymbol{r}-\boldsymbol{\rho})}}. \tag{5.0.1}$$

The background profiles $n(\boldsymbol{r}-\boldsymbol{\rho})$ and $T(\boldsymbol{r}-\boldsymbol{\rho})$ are defined in gyrocenter coordinates $\boldsymbol{R} = \boldsymbol{r} - \boldsymbol{\rho}$ ($\boldsymbol{\rho}$ is Larmor radius vector) to achieve a background which does not oscillate with the Larmor frequency. To avoid the complexity of finding an adequate treatment of the boundary condition, the profiles are set up periodically by using a sine-profile in x-direction

$$n(\boldsymbol{r},\boldsymbol{v}) = 1 + \kappa_n \sin\Big(k_0\left(x - \frac{q}{B}v_y\right)\Big), \tag{5.0.2}$$

$$T(\boldsymbol{r},\boldsymbol{v}) = 1 + \kappa_T \sin\Big(k_0\left(x - \frac{q}{B}v_y\right)\Big). \tag{5.0.3}$$

The background density gradient should not generate an electric field. Thus, all modes with wave numbers parallel to the gradient are removed from the electrostatic potential by subtracting the average over the $y-z$-plane

$$\phi = n - \langle n\rangle_{y,z} = n - \frac{1}{L_y L_z}\int n \mathrm{d}y\mathrm{d}z. \tag{5.0.4}$$

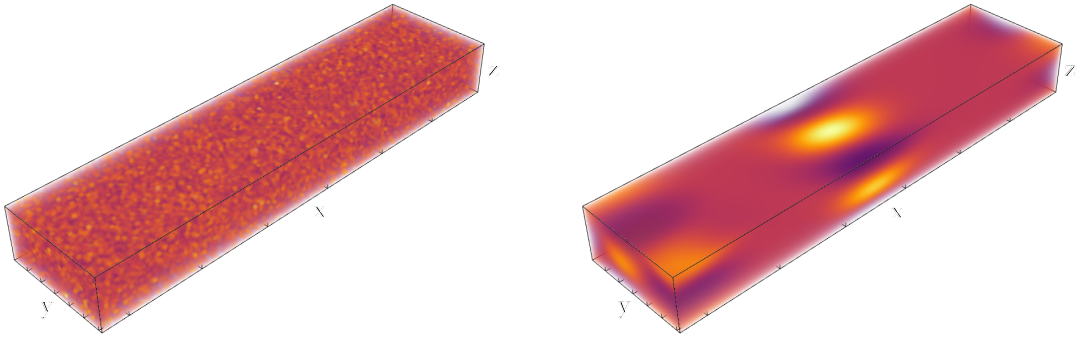

(a) t = 0

(b) t = 3500

(c) t = 7000

(d) t = 14000

Figure 5.1: Snapshots of electrostatic potential in simulation of an unstable ITG modes with nonlinear treatment of temperature gradient different points in time

5.1 Ion temperature gradient instability

In this first section, the linearly unstable ITG modes caused by the nonlinear temperature gradient is compared with the results from our analytical calculation with a local temperature gradient in chapter 3. When choosing parameters for the background profile, one has to pay attention that the wave length of the unstable mode $\lambda_{\mathrm{ITG}} = \frac{2\pi}{k_y}$ is shorter than the typical gradient length of the profile $1/L_T \sim \partial_x \ln T(x)$. For the first simulation, the parameters $\kappa_n = 0$, $\kappa_T = 0.5$ and $k_0 = 0.2$ were chosen, resulting in a temperature gradient $\max_{x\in[0,L_x]} \frac{\partial_x T(x)}{T(x)} = 0.115$, where L_x is the box length in x-direction. The simulation was performed on a box with of length $L = 10\pi \times \frac{5}{2}\pi \times 240\pi$ (the full set of parameters can be found in the simulation index in the appendix B.4). In figure 5.1 snapshots of the electrostatic potential are displayed for different points in time. The potential is initialized with a small white noise perturbation (figure 5.1(a)). After a short period a clear mode structure arises. Two waves with opposing phase velocities can be seen on the two opposite gradients of the background profile. The box length is chosen such that the fastest growing mode with wavenumber $k_y = 0.8$, $k_z = \frac{1}{120}$ fits exactly into the box. The phase velocity of the wave is in the direction of the diamagnetic drift

$$u_{\mathrm{dia}} = -\frac{\nabla(nT) \times \hat{\boldsymbol{z}}}{n}. \tag{5.1.1}$$

After the linear phase, the perturbation starts to saturate (figure 5.1(c)) and finally results in saturated turbulence (figure 5.1(d)). The gradient is comparable to the nonlinear simulation performed in section 3.1. However, in comparison to the test with local treatment of the gradient, no high-frequency waves are excited in the nonlinear phase and the distribution function is not locally negative.

5.1.1 Growth rate and frequency

For a more quantitative analysis of the mode behavior, the growth rate and the frequency of the excited waves are analyzed. The snapshots in figure 5.1 show that the modes have a finite wavenumber in the x-direction. Before the results from the code can be compared to the dispersion relation derived in section 3.1

$$0 = \left[\omega - k_y \frac{\nabla T}{T}\partial_\xi\right] \frac{1}{|k_z|}\sqrt{\frac{\xi}{2}} \sum_{p\in\mathbb{Z}} Z\left(\frac{\omega + p}{|k_z|}\sqrt{\frac{\xi}{2}}\right) \Gamma_p\left(\frac{k_\perp^2}{\xi}\right) - 2, \tag{5.1.2}$$

the wavenumber parallel to the gradient is determined. In fig. 5.2(a), a cross-section of the dominant mode is displayed. For this purpose, the electrostatic potential is Fourier transformed in y and z direction and the profile of the dominate mode $\phi(x, k_y = \frac{8}{10}, k_z = \frac{1}{120})$ is extra extracted. The profile shows two peaks located at the maxima of the normalized gradient $\frac{\partial x T(x)}{T(x)}$. To determine the wavenumber, a sine wave is fitted to the data, within the full width half maximum (FWHM) of the profile

which results ins a wavenumber $k_x \approx 0.44$. To be able to compare the nonlinear gradient with the analytical calculation, the mean of the gradient is computed across the mode profile. $\frac{\partial x T(x)}{T(x)} = \frac{\kappa_T k_0 \cos(k_0 x)}{1+\kappa \sin(k_0 x)}$ has its maximum at $x_{\max} = \frac{\pi \pm \operatorname{asin}(\kappa)}{k_0}$, where κ_T is the amplitude of the temperature profile (compare equation (5.0.3)). The effective gradient which has been used for the analytical calculations is given by

$$\kappa_T^{\text{eff}} = \frac{k_0}{\pi} \int_{x_{\max}-\frac{\pi}{2k_0}}^{x_{\max}+\frac{\pi}{2k_0}} \frac{\kappa_T k_0 \cos(k_0 x)}{1+\kappa \sin(k_0 x)} \mathrm{d}x. \tag{5.1.3}$$

After the wavenumber and the effective gradient are determined, the solution of the dispersion relation can be determined from the analytical dispersion relation in equation 5.1.2. The expected complex frequency for the fastest growing mode is

$$\omega = 0.01850 + 0.00420i. \tag{5.1.4}$$

Figure 5.2(b) shows the root-mean-square (RMS) of the electrostatic potential in

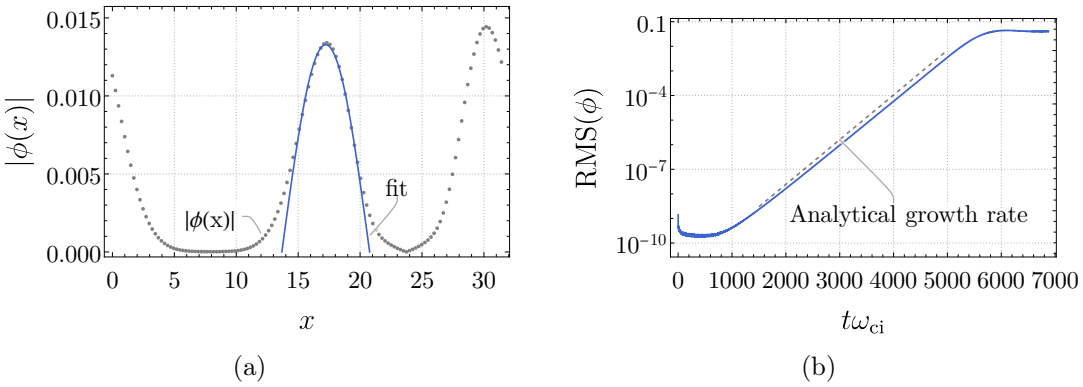

Figure 5.2: Fit of sine-wave (blue) to x-profile of one mode within the FWHM (gray) (a) and root mean square of electrostatic potential compared to expected growth rate (b)

a logarithmic scale (blue) alongside the expected linear growth rate as dashed gray line. The result shows that the analytically predicted growth rate is sightly larger compared to the expected value. The growth rate and frequency for the simulation are extracted from the Fourier transformed electrostatic potential $\phi(\boldsymbol{k}, t)$, resulting in

$$\omega_{\text{BSL}} = 0.01809 + 0.00409i. \tag{5.1.5}$$

The growth rate and frequency have an error of $\sim 2\%$ compared to the analytically calculated values.

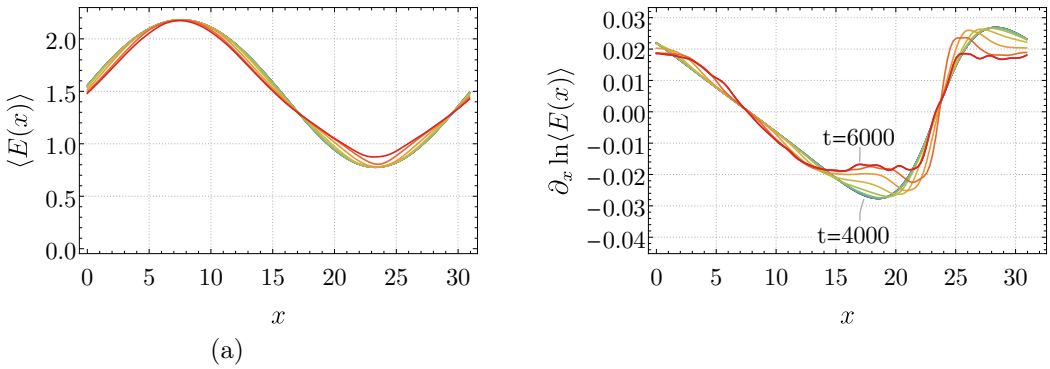

(a)

Figure 5.3: Energy density profile $\langle E(x)\rangle$ (a) and gradient profile $\partial_x \ln\langle E(x)\rangle$ (b) for different times between $T = 4000$ (blue) and $T = 6000$ (red)

5.1.2 Energy transport

In this section, I investigate the change in the background gradient due to the energy transport of ITG modes. The discussion in section 3.2 has revealed that the change in the kinetic energy and the electrostatic potential is given by

$$\partial_t E = \partial_t \epsilon + \phi \partial_t n = -\nabla \cdot (\boldsymbol{Q} + \boldsymbol{S}), \tag{5.1.6}$$

where on the left-hand-side $\partial_t \epsilon$ denotes the change in the local kinetic energy density and $\phi \partial_t n$ rate of change of the energy contained in the adiabatic electrons. The right-hand-side is divergence of the kinetic energy flux $\boldsymbol{Q} = \int \frac{v^2}{2} \boldsymbol{v} f \mathrm{d}^3 v$ and the Poynting flux $\boldsymbol{S} = \phi \int \boldsymbol{v} f \mathrm{d}^3 v$. The contributions to the energy flux are computed in section 3.2. In this example the fluxes are not computed directly, however, the energy flux is deduced from the rate of change of the energy profile

$$\langle E(x)\rangle = \frac{1}{L_y L_z} \int_0^{L_y} \int_0^{L_z} \left(\epsilon + \frac{\phi^2}{2}\right) \mathrm{d}y \mathrm{d}z. \tag{5.1.7}$$

In figure 5.3(a), multiple background profiles at equally spaced points in time between $t = 4000$ (blue) till $t = 6000$ (red) are displayed. The profile is reduced with time, which is better visible when plotting the temperature gradient (compare figure 5.3(b)), where a clear flattening of the gradient is observable.
The temperature profile is introduced into the system in gyrocenter coordinates $\boldsymbol{R} = \boldsymbol{r} - \boldsymbol{\rho}$, and thus the distribution function is a solution to the stationary Vlasov equation

$$\boldsymbol{v} \cdot \nabla f + \boldsymbol{v} \times \boldsymbol{B} \cdot \nabla_{\boldsymbol{v}} = 0. \tag{5.1.8}$$

However, numerically these two terms do not cancel perfectly, resulting in a spurious time dependency of the background distribution function, which manifests itself in small oscillation of the background profile with the Larmor frequency. Thus, the

change in the temperature profile is only visible in a later stage of the simulation where the fluctuations are large enough that the induced transport exceeds the oscillation of the background. The sum of the energy fluxes is calculated by computing the time derivative of the energy profile $\langle E(x)\rangle(t,x)$ and determining the integral

$$\zeta(x) = (Q_x + S_x) = -\int_0^x \partial_t \langle E(x)\rangle(x')\mathrm{d}x'. \tag{5.1.9}$$

The considerations of the quasi-linear fluxes in section 3.2 showed, that the fluxes are quadratic order the fluctuating quantities. Therefore, figure 5.4 displays the resulting flux normalized to the square of the electrostatic potential $\frac{(\boldsymbol{Q}(t,x)+\boldsymbol{S}(t,x))}{\bar{\phi}(t,x)^2}$ for different times between $t = 3500$ (blue) and $t = 530$ (red), where

$$\bar{\phi}(x) = \left(\frac{1}{L_y L_z}\int_0^{L_y}\int_0^{L_z} \phi(x,y,z)^2 \mathrm{d}z\mathrm{d}y\right)^{\frac{1}{2}}. \tag{5.1.10}$$

The x-profile of the energy flux resembles the electrostatic potential. Figure 5.4 shows the time evolution of the energy flux at its maximum. While the change in the energy profile is dominated spurious oscillation of the background distribution for $t < 4800$, the energy flux becomes large enough towards the end of the linear phase. The resulting ratio between the energy flux and the square of the electrostatic potential is $\max_{x\in[0,L_x]}(\zeta/\bar{\phi}^2) \sim 0.7$, where $\max_x f(x)$ gives the maximum value of a function $f(x)$ in the domain between 0 and the length of the domain in x-direction L_x. The $\boldsymbol{E}\times\boldsymbol{B}$ heat flux can be computed with the the method described in section 3.2 for an ITG mode with $k_y = 0.8$ and $k_x = 0.44$ and is expected to be $Q_x^{\boldsymbol{E}\times\boldsymbol{B}}/\mathrm{RMS}(\phi)^2 \approx 0.99$ (compare figure 3.2(a)). The deviation is $\sim 30\%$.

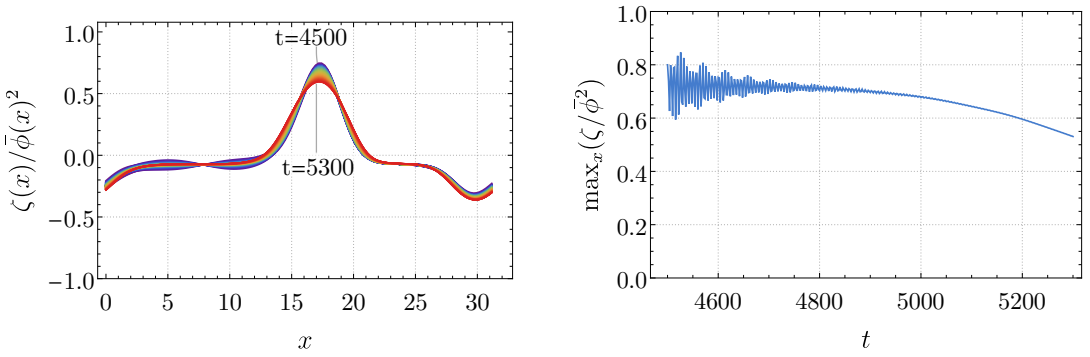

(a) (b)

Figure 5.4: Profile of energy flux in direction of gradient for different times (a) and time evolution of normalized maximum energy flux (b)

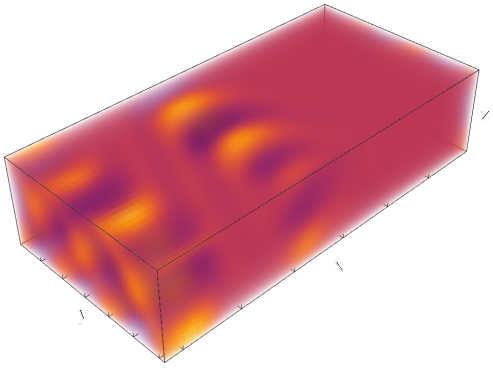

Figure 5.5: Snapshot of electrostatic potential in linear phase of cyclotron instability simulation with real gradient

5.2 Cyclotron instability

5.2.1 Dispersion relation

I have showed in section 4.3 that the ion Bernstein waves can be driven unstable by a temperature and density gradient. Henceforth, the same should be reproducible with nonlinear gradients. For this purpose, a simulation has been performed with similar gradients compared to section 4.3.2, however, with a nonlinear treatment of the gradients. In order to achieve the higher gradients necessary for the excitation of IBWs, either the amplitude or the wavenumber k_0 of the background perturbation κ_T can be increased as the gradient is $\propto \kappa_T k_0$.
The amplitudes of the temperature and density profiles have been chosen to be $\kappa_T = 0.36$ and $\kappa_n = 0.44$ respectively. The wavenumber of the background profile is $k_0 = \frac{8}{10}$. The full set of all parameters can be found again in the simulation index in the appendix B.4.1. The profiles for the simulation are set in gyrocenter coordinates. As a result, the profiles in particle coordinates are not necessarily the same. In the temperature profile used for the ITG simulation in section 5.1 the difference is negligible because the deviation is $O(k_0^2)$ and the background has a small wavenumber $k_0^2 \ll 1$. In the analytical calculation of the ansatz for the background distribution is set in gyrocenter coordinates. However, when the local limit is taken $k_0 \to 0$ the distribution function in particle and gyrocenter coordinates is identical. This difference has be taken into account when the simulations are compared to experimental data.
The simulation shows a lot of similarities with the ITG simulation in section 5.1. A snapshot of the electrostatic potential in the linear phase is shown in figure 5.5. Two waves are propagating in opposite direction on the two opposing gradients. The direction of propagation is in the direction of the diamagnetic velocity. I have fitted

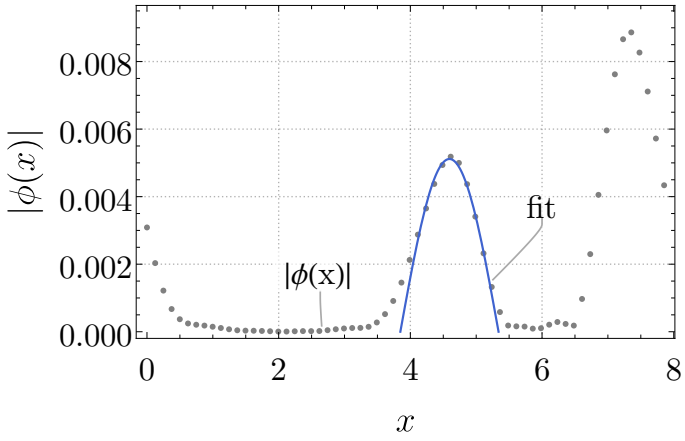

Figure 5.6: Fit of sin-wave (blue) to the x-profile of the electrostatic potential (gray) to determine wavenumber k_x parallel to the gradient

a sine-wave to the FWHM of one of the modes envelopes to determine to dominate wavenumber parallel to the gradient (compare figure 5.6), resulting in $k_x \approx 2.1$. The electrostatic potential is Fourier transformed and the growth rate and frequency is determined for the three wavenumbers y-direction $k_y = 2, 4, 6$ and $k_z = \frac{1}{40}$. The simulated growth rate (bullets) is shown in figure 5.7(a) is plotted in comparison the analytically predicted dispersion relation (colored lines). The analytical results suggest that the dominant mode is the one with the highest wavenumber resolved by the grid. However, the snapshot of the electrostatic potential in figure 5.5 suggests that the dominant mode has $k_y = 6$ which is confirmed by the underestimated growth rate for the $p = -4$ IBW with $k_y = 8$ (compare figure 5.7(a)). As laid out in section 2.6.3, larger wave numbers are subject to a higher numerical diffusion by the dispersion relation Furthermore, I have derived a method to compute the numerical

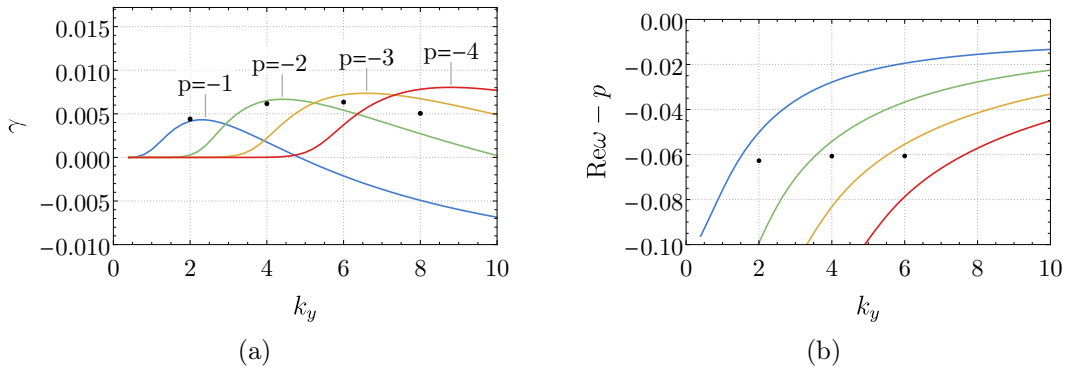

Figure 5.7: Comparison of growth rate (a) and frequency (b) of unstable IBWs between analytical solutions (lines) and simulated results (dots)

diffusion coefficient for a given discretization in section 2.6.3 which can be used to compute expected growth rate in a numerical experiment by adding the numerical

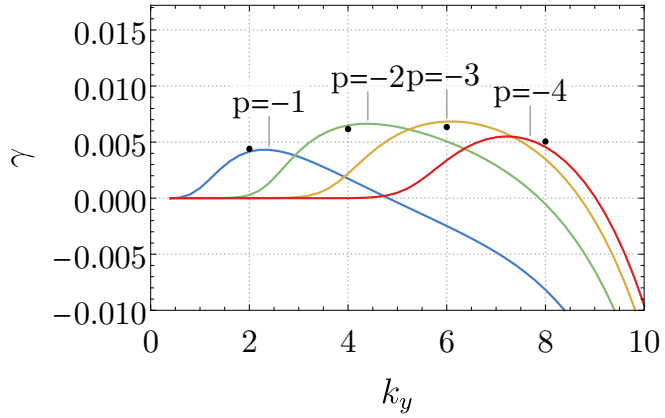

Figure 5.8: Growth rate of cyclotron instability for various harmonics with correction of numerical error from interpolation

diffusion coefficient to the growth rate determined from the distribution function. In figure 5.8, adapted growth rate is shown along with our simulated results. When the numerical diffusion is taken into account, the analytical results correctly predict that the third harmonic is the dominant mode and the growth rate of the $p = -4$ IBW agrees very well with the result from the simulation. To be able to reproduce the correct growth rate for more Fourier modes, a larger resolution for the y-direction would need to be chosen.
The comparison for the frequencies is shown in figure 5.7(b). The results for the complex frequency from the simulation summarized in table 5.1. The simulated growth rates deviate $\sim 5 - 10\%$ from the predicted results. The frequencies show a deviation of $\sim 1\%$. However, when the small shift compared to the harmonic of the Larmor frequency is considered the errors are $\sim 10\%$. The results are not tested for numerical convergence, as increasing the resolution would drastically increase the computational cost. Overall, the results show a very good agreement with the linear theory.

Table 5.1: Comparison of complex frequency between analytical dispersion relation and simulated results

k_y	ω_{ana}	ω_{BSL6D}
2	$-1.051 + 0.0042i$	$-1.063 + 0.0044i$
4	$-2.055 + 0.0065i$	$-2.061 + 0.0062i$
6	$-3.056 + 0.0072i$	$-3.061 + 0.0063i$
8	$-4.058 + 0.0078i$	$\omega' + 0.0051i$

5.2.2 Energy transport

In a second test, I have computed the energy flux induced by the excited modes and comparing it to the $\boldsymbol{E} \times \boldsymbol{B}$ energy flux shown in section 4.3.2. The derivation

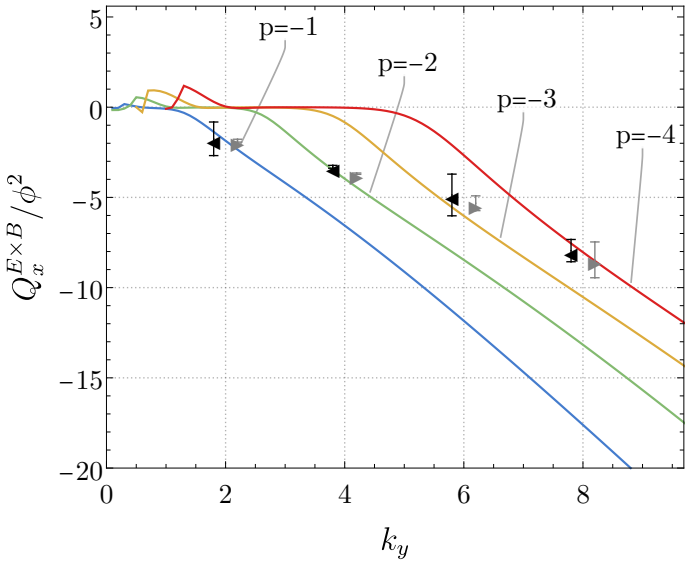

Figure 5.9: Results for time averaged $\boldsymbol{E}\times\boldsymbol{B}$ heat flux of kinetic simulation in figure 5.6 with left mode (◀) at $x = 4.79$ or the right mode (▶) at $x = 7.24$ in comparison with the analytically derived energy fluxes form, including standard deviation as error bars. The points are slightly shifted left and right for better readability 3.2 .

of the various contributions to the energy transport is shown in section 3.2. The discussion in section 4.3.2 has revealed that the energy transport in the direction of the gradient is dominated by the $\boldsymbol{E}\times\boldsymbol{B}$ heat flux, which is given by

$$\boldsymbol{Q}_{\perp}^{E\times B} = -\nabla\phi\times\hat{\boldsymbol{z}}\epsilon. \tag{5.2.1}$$

Instead of deducing the energy transport from the rate of change of the temperature profile (compare section 5.1.2), I have directly computed the heat flux. The electrostatic potential and the energy density $\epsilon = \int \frac{v^2}{2} f \mathrm{d}^3 v$ are computed in the simulation. The modes of interest ($k_z = \frac{1}{40}$ and $k_y = 2, 4, 6, 8$) are extracted by Fourier transforming the two quantities. The energy flux on the two gradients of the background temperature profile have opposite signs. Figure 5.9, displays the ratio between the $\boldsymbol{E}\times\boldsymbol{B}$ heat flux and the square of the electrostatic potential. The markers indicate whether the flux is measured on the left mode (◀) at $x = 4.79$ or the right mode (▶) at $x = 7.24$ in figure 5.6.

These results confirm again, that the majority of the energy flux is induced by the modes with large p. Combined with the fact that peak growth rate increases for higher harmonics p demonstrates the relevance of the IBW in the energy transport. The simulated heat fluxes agree very well with the analytically computed results.
The simulations of the nonlinear saturation, which has been simulated with local gradients in section 4.3.3, is a work in progress. The main limiting factor is the computational cost. In order to correctly simulate turbulence in the system, an increase in resolution is necessary which in consequence require larger computational

cost. These simulations, requiring days on hundreds of CPUs, already scrape the limit of what is currently available.

5.3 Summary

The focus of this chapter is to move from a local gradient set-up to a nonlinear treatment of the density and temperature gradient. The gradients are introduced in the system by initializing the distribution function with a profile in x direction. No further sources are required throughout the simulation. In order to maintain the periodic boundary conditions, a symmetric profile with two opposing gradients is used. This increases the computational cost of the simulation because a larger domain is necessary, but it removes the complications of describing the boundary conditions. After the electrostatic potential is modified such that the contribution from the background is removed, a first test for an ITG simulation could be performed.
The simulation reproduce the correct growth rate that has been determined from the dispersion relation. The code has proved to be capable of simulating the instability far into the nonlinear regime. In contrast to the simulations with a local treatment of the gradients, the simulations with nonlinear gradients does not show negative phase space densities and now high frequency waves are excited during the saturation phase.
In case of nonlinear simulations of the temperature gradient, the transport of the excited modes slowly deteriorate the initial profile over time. The rate at which the profile is reduced, gives insights about the energy flux in the system. The energy flux based on this rate is computed and I have demonstrated that it agrees well with the results from quasi-linear theory (compare 3.2).
In addition to the ITG test, a simulation of a cyclotron instability with the nonlinear gradient has been shown. The resulting growth rates are in good agreement with the expected growth rate from the linear theory with a deviation of $5 - 10\%$. The function used for the background temperature profile was a sin-wave. It would be interesting to see whether the agreement improves when a function which has a constant gradient over a larger width (e.g. the flat-top profile [Görler, 2010]).
Furthermore, the results suggest that local treatment of the gradients is problematic in 6D kinetic simulations (compare section 4.2.1) because the source term can lead to negative phase space densities which lead to the excitation of spurious high frequency modes. The nonlinear treatment of the gradients solves the issue of negative phase space densities.
Furthermore, we have been able to reproduce the cyclotron instability with the presence of steep gradients, with a nonlinear treatment of the ions. These simulations have further confirmed the linear instability of the ion Bernstein waves and have shown that a significant amount of energy transport is induced by such modes. The result presented in this chapter further strengthen the significance of a 6D kinetic treatment of the plasma edge.

Chapter 6

Conclusions and Outlook

6.1 Scientific highlights

The first part of this work is focused on the verification of our novel 6D kinetic Vlasov code [Kormann et al., 2019]. As an example, simulation of slab ion temperature gradient instabilities 3 has been chosen. The ITG instability has the advantage that it is correctly described by the gyrokinetic model when the limit of small gradients is applied. It has been shown that the code correctly reproduces the analytically derived dispersion relation for a large range of temperature gradients and perpendicular wave numbers. For a more detailed verification, a comprehensive description of the energy fluxes caused by linear modes in the 6D kinetic system has been derived (see section 3.2). The description divides the energy flux into its contributions, the $\boldsymbol{E} \times \boldsymbol{B}$-heat flux, the stress induces heat flux, and the Poynting flux. This detailed description of the energy flux relies on the higher moments of the distribution function that are, in contrast to gyrokinetic models, correctly described by the 6D kinetic model. However, it is expected that the sum of the contributions matches the energy flux in the gyrokinetic model. The analytical calculations, as well as the simulations, have shown that the two contributions of the energy flux that are not covered by gyrokinetic theory cancel exactly in the limit of small gradients.
In addition to the verification of the code in the linear regime, a comparative study to verify the code in the nonlinear phase of ITG simulations has been which has shown that the $\boldsymbol{E} \times \boldsymbol{B}$ heat flux matches between the 6D kinetic simulations and the gyrokinetic code CGYRO (compare section 3.3).
During the verification process, the simulation has revealed the excitation of high-frequency waves (compare figure 3.5) during the nonlinear saturation phase. This phenomenon is accounted for in literature in similar kinetic simulations of ITG instabilities [Sturdevant et al., 2016]. However, an explanation for the occurrence of high-frequency wave in simulations with local gradients has not yet been known. The distribution of the frequencies of the excited modes indicates a relation to ion Bernstein waves due to their clustering close to the harmonics of the Larmor frequency (see figure 3.6). The discrete distribution of the frequencies and the large difference between the ITG frequency compared to the Larmor frequency ($\frac{\omega_{\mathrm{ITG}}}{\omega_{\mathrm{ci}}} \sim 0.1$) sug-

gests the presence of secondary instabilities. The excitation of ion Bernstein waves is scarcely studied in literature. The missing explanation has been the inspiration for the main body of this work.
Section 4.2.1 shown with the help of the Cauchy argument principle that the locally present velocity distribution in the nonlinear ITG simulations can cause a destabilization of the IBWs. This is a significant result because it gives a possible explanation for the high-frequency waves witnessed in 6D kinetic ITG simulations. Furthermore, it provides a first example of a distribution function, which originates in a simulation close to the gyrokinetic limit, causing the excitation of high frequency waves. In addition to the study of the stability properties of the cyclotron instability in the presence of various velocity distributions, the destabilization of the ion Bernstein waves due to temperature and density gradients has been be shown.
Through an extensive study of the properties of the 6D kinetic dispersion relation and the derivation of stability criteria, regimes in which the cyclotron instability occur have been identified (section 4.3). It has been shown that a combination of parallel temperature and density gradients with a ratio $\eta = \frac{\partial_x \ln T}{\partial_x \ln n} \sim 1$ leads to a destabilization of the ion Bernstein waves. The analytically derived frequencies and growth rates have been verified with the help of the BSL6D code (compare figure 4.18).
In addition to showing the existence of the cyclotron instability and analyzing the dispersion relation analytically and numerically over a large range of parameters, the relevance the relevance of the energy transport induced by these unstable modes has been demonstrated (compare section 4.3.2). For a given wavenumber the energy transport induced by modes with larger frequencies $\omega \sim p$ introduce a lower $\boldsymbol{E} \times \boldsymbol{B}$ heat flux. However, the maximum growth rate of the IBWs close to the higher harmonics resides at larger wave numbers. This effect prevails, and the simulations have shown that the majority of the energy transport is caused by the mode associated with the largest harmonic p. Furthermore, a nonlinear simulation of the cyclotron instability have demonstrated that the ion Bernstein wave turbulence causes a significant energy flux (compare section 4.3.3).
In the chapters 3 and 4 a local representation of the temperature gradient is used. In the local limit, it is assumed that the gradient length is much larger than the domain length and the temperature or density are constant across the domain. Chapter 3 has established that the local representation can cause local negative phase space densities, which can cause the excitation of spurious high-frequency modes in the system. This result has revealed the necessity of a nonlinear treatment of the gradients, which means that a temperature and density profile is induced in the system at initialization and the response of the plasma is simulated without any simplification. The simulations in section 5 have confirmed, that the dispersion relation and the energy fluxes predicted from our analytical calculations are correctly reproduced numerically for the ITG and the cyclotron instability, even when the gradients are treated nonlinearly which does not only demonstrate the capabilities of the BSL6D code but also the accuracy of my analytical calculation.
Throughout this work, important insights have been gained into the behavior of ion

Bernstein waves in various scenarios. Especially the demonstration of the cyclotron instability in the presence of steep density and temperature gradients might give an important insight into the plasma behavior in the edge region of a fusion device. These insights coupled with a numerical tool which allows the simulation of microinstabilities without any limitations on the gradient steepness or fluctuation amplitude (section 5) is a notable achievement and opens the door for a wide range of future investigations.

6.2 Discussion

The results in this work are summarized at the end of each chapter and a brief highlight of scientific results is given in section 6.1. This section highlights the more remarkable results and discuss their relevance and limitations.

Excitation of high-frequency waves in ITG simulations with local gradients Section 3.3 shows that the nonlinear saturation of an ion temperature gradient simulation can lead to the excitation of high frequency waves when the gradients are treated in a local limit. It is possible that the nonlinear interaction between low-frequency waves leads to a continuous excitation of waves with increasing frequencies. In this process two ITG modes with frequencies ω_1 and ω_2 can couple and cause a mode with the frequency $\omega = \omega_1 + \omega_2$, what causes that the energy is continuously transported up in the frequency spectrum and a homogeneous distribution of energy across the frequency spectrum is expected. However, figure 3.6 shows that the high-frequency waves are excited in frequency bands close to the harmonics of the Larmor frequency, while close to no high-frequency waves are excited in the gaps between the harmonics. This observation suggests that a secondary instability exists that causes the excitation of waves with certain frequencies, in the presence of a primary distribution function.
The question has to be raised, whether the high-frequency waves in our simulations are of physical nature. In case these waves are nonphysical, they can either be caused by errors in the model or in the discretization of the system. In the beginning of this project, a lot of efforts have been spent on ensuring that the latter is not responsible for the occurrence of the fast oscillations. Among others, different discretization of the velocity space have been tested and simulations at varying resolutions have been performed.
After having confirmed with an acceptable level of certainty that the waves are not excited by an error in the discretization, the properties of the excited modes and the surrounding conditions have been investigated. The investigations have found that the local treatment of the temperature gradient can cause local negative phase space densities (compare figure 3.8). A negative density in phase space has an infinite amount of free energy. Nonetheless, it is not clear whether a mechanism exists that can transfer the energy into an electrostatic wave and thus, whether the negative phase space density can be responsible for the secondary instability.

The following chapter shows that the negative phase space densities in fact destabilize the ion Bernstein waves and cause significant growth rates (compare section 4.3).
Furthermore, it is shown in chapter 5 that a similar simulation of the ion temperature gradient instability does not lead to the excitation of high-frequency waves in the nonlinear phase, when a nonlinear temperature gradient is used. These two points suggest that the waves witnessed in the simulations with local gradient are a result from the treatment of the gradient. This implies that these local limits, which are commonly used in gyrokinetic simulations can cause significant problems in 6D kinetic simulations.
However, while the excitation of the ion Bernstein waves might be unphysical, the simulations with local gradients still hold merit. They have provided a fist example that the ion Bernstein waves can be unstable in certain scenarios. The study of the stability of ion Bernstein waves in the presence of temperature and density gradients (section 4.2.3) has shown that in scenarios with steep gradients cyclotron instability exists. I have showcased exampled where the growth rate of ITG and IBW modes are comparable and the IBWs play a significant role in the resulting turbulence and energy transport. I have been able to verify the existence of the cyclotron instability with simulations with local, as well as nonlinear treatment of the gradients.

Comparison of steep gradients to experimental values Comparing the gradient lengths used in our simulations with experimental data from H-mode discharge gives instructive insights in the relevance of the cyclotron instability in the plasma edge.
The characteristic length of the temperature gradient $L_T = 1/\partial_x(\ln T(x))$ in the simulation of the cyclotron instability (section 5.2) is $L_T =\sim 5.3$, which is given in units of the Larmor radius. For a comparison with the experiment, a typical H-mode discharge of ASDEX-Upgrade has been used, which has magnetic field of $\sim$ 3T. Using the data from shot #20431 [Told et al., 2008], the Larmor radius in the edge is $\rho \sim 0.002$m. Using the Larmor radius, the characteristic gradient length of our simulations can be computed in meter, resulting in $L_T = 0.01$m. Comparing this to values presented in literature e.g. $L_T \sim 0.01$m [Wolfrum et al., 2007] shows that the gradients used in our simulations are well in the range as the experimentally observed gradients.
Another relevant quantity when discussing the relevance of an instability is the ratio between the density and temperature gradient $\eta = \frac{\partial_x \ln T}{\partial_x \ln T}$. In the H-mode this ratio is typically $\eta = 0.6 - 1.2$ [Wolfrum et al., 2007] which is large enough to suppress the gyrokinetic ion temperature gradient mode. However, it is shown that a gradient ratio $\eta \sim 1$ favors the cyclotron instability.

Necessity of parallel wave number for cyclotron instability Section 4.2.1 discusses that it is expected that the ion cyclotron instability is independent of the parallel wavenumber because of the high frequency and the low parallel wave number. Parallel transit time of the ion sound wave is $\frac{1}{k_z v_{\mathrm{th}}}$ which is much larger

than the period of the cyclotron oscillation $\frac{2\pi}{\omega_c}$. However, in the discussion about the cyclotron instability in the presence of ion temperature and density gradients, the parallel wave number has a significant impact on the instability, which is evident when investigating the structure of the dispersion relation (equation 4.3.3). The argument of the plasma dispersion function $Z(x)$ of every term in the infinite sum depends only on the shift between the frequency ω and the harmonic of the Larmor frequency p. For this reason the dependence of the cyclotron instability is the same as for the ITG instability.

6.3 Outlook

This work can be seen as a stepping stone toward a better understanding of the role of high-frequency waves in the steep gradient regime. Showing the existence and instability of ion Bernstein waves has proved the relevance of a 6D kinetic treatment of the plasma edge. Nonetheless, for realistic scenarios further work has to be done. Our efforts on extending the capabilities of our simulation tool are twofold. On the one hand, an extension of the physical model and work towards a more realistic description of the plasma is ongoing. On the other hand, modern software development tools are used to allow the code to utilize the achievements of recent computing technologies.

Extension of physical model The major effort in extending the physical model focuses on the description of the electrons in the plasma. In the current model, it is assumed that the electrons can react instantly to the dynamic of the ions. In this limit the mass ratio between the ions and electrons is assumed to be infinite. Even mass-less electrons are bound to the magnetic field lines, due to the Lorentz force. A model which accounts for the restricted motion in the perpendicular direction and only allows a parallel adiabatic reaction is derived. This modification will introduce stronger radial electric fields and zonal flows into the system. The addition of a more complex electron model leads to the presence of plasma waves in the system, which have a very large frequency $\omega_p \gg \omega_c$ and can cause major numerical challenges. An intelligent treatment of the electrons is necessary to eliminate the plasma wave from the system. In the long run, it is planned to extend the code to a full drift kinetic description of the electrons.
In addition to a more complex electron model, a more complete description of the electromagnetic fields will be necessary for a realistic description of the plasma edge. The model should be extended to allow for magnetic field fluctuations and the resulting non-linear effects on the plasma.

Porting to GPU infrastructure The simulations performed in this work scrape on the limit of what is currently capable with modern HPC systems. For more detailed simulations, even with the current model, a drastic increase in computational power is necessary. The currently used version of the Vlasov solver is implemented

to run in parallel on large CPU-HPC systems and the largest simulations take days on several hundred CPUs. In order to utilize the developments in modern HPC technology, namely the integration of GPUs in supercomputers, efforts by our group have been undertaken to redevelop our code [Schild et al., 2023]. The use of the performance portability tool Kokkos [Trott et al., 2022] allows the code to be executed on a wide variety of hardware architectures.
The use of GPUs drastically increases the performance on a single computing node as the memory bandwidth increases by a factor of ~ 15 compared to the top tier CPUs on the market (comparison between NVIDIA A100 GPU and Intel Xeon Gold CPU). Still, the size of simulations and the extremely expensive scaling of six dimensional simulations (N^6, where N is the number of grid points in one dimension) requires a distribution of memory on multiple computing units. This introduces an immense bottleneck as the communication between two computing nodes is orders of magnitude slower compared to the memory access. Finding intelligent solutions that reduce the amount of data sent and received between nodes is one of the major challenges for high-dimensional simulation codes.

Bibliography

[Bandaru et al., 2019] Bandaru, V., Hoelzl, M., Artola, F. J., Papp, G., and Huijsmans, G. T. A. (2019). Simulating the nonlinear interaction of relativistic electrons and tokamak plasma instabilities: Implementation and validation of a fluid model. *Physical Review E*, 99(6).

[Bateman et al., 1998] Bateman, G., Kritz, A. H., Kinsey, J. E., Redd, A. J., and Weiland, J. (1998). Predicting temperature and density profiles in tokamaks. *Physics of Plasmas*, 5(5):1793–1799.

[Bernstein, 1958] Bernstein, I. B. (1958). Waves in a plasma in a magnetic field. *Phys. Rev.*, 109:10–21.

[Biskamp, 1997] Biskamp, D. (1997). *Nonlinear magnetohydrodynamics*. Number 1. Cambridge University Press.

[Braginskii, 1965] Braginskii, S. I. (1965). Transport processes in a plasma. *Reviews of Plasma Physics*, 1:205.

[Brambilla, 1998] Brambilla, M. (1998). *Kinetic theory of plasma waves: homogeneous plasmas*. Number 96. Oxford University Press.

[Burrell et al., 1995] Burrell, K., Doyle, E., Gohil, P., Groebner, R., Kim, J., La Haye, R., Lao, L., Moyer, R., Osborne, T., Peebles, W., et al. (1995). Erratum:"role of the radial electric field in the transition from l (low) mode to h (high) mode to vh (very high) mode in the diii-d tokamak"[phys. plasmas 1, 1536 (1994)]. *Physics of Plasmas*, 2(4):1358–1358.

[Candy et al., 2016] Candy, J., Belli, E., and Bravenec, R. (2016). A high-accuracy eulerian gyrokinetic solver for collisional plasmas. *Journal of Computational Physics*, 324:73–93.

[Candy and Waltz, 2003] Candy, J. and Waltz, R. (2003). An eulerian gyrokinetic-maxwell solver. *Journal of Computational Physics*, 186(2):545–581.

[Cathey et al., 2021] Cathey, A., Hoelzl, M., Futatani, S., Lang, P. T., Lackner, K., Huijsmans, G. T. A., Pamela, S. J. P., and Günter, S. (2021). Comparing spontaneous and pellet-triggered elms via non-linear extended mhd simulations. *Plasma Physics and Controlled Fusion*, 63(7):075016.

[Charney et al., 1950] Charney, J. G., Fjörtoft, R., and Neumann, J. (1950). Numerical integration of the barotropic vorticity equation. *Tellus*, 2(4):237–254.

[Chen, 1984] Chen, F. F. (1984). *Introduction to plasma physics and controlled fusion*, volume 1. Springer.

[Cheng and Knorr, 1976] Cheng, C.-Z. and Knorr, G. (1976). The integration of the vlasov equation in configuration space. *Journal of Computational Physics*, 22(3):330–351.

[Coulaud et al., 1999] Coulaud, O., Sonnendrücker, E., Dillon, E., Bertrand, P., and Ghizzo, A. (1999). Parallelization of semi-lagrangian vlasov codes. *Journal of plasma physics*, 61(3):435–448.

[Craddock et al., 1994] Craddock, G. G., Diamond, P. H., Ono, M., and Biglari, H. (1994). Theory of ion bernstein wave induced shear suppression of turbulence. *Physics of Plasmas*, 1(6):1944–1952.

[Crouseilles et al., 2009] Crouseilles, N., Latu, G., and Sonnendrücker, E. (2009). A parallel vlasov solver based on local cubic spline interpolation on patches. *Journal of Computational Physics*, 228(5):1429–1446.

[Debye and Hückel, 1923] Debye, P. and Hückel, E. (1923). Zur theorie der elektrolyte. i. gefrierpunktserniedrigung und verwandte erscheinungen. *Physikalische Zeitschrift*, 24(185):305.

[Deng et al., 2016] Deng, Z., Waltz, R., and Wang, X. (2016). Cyclokinetic models and simulations for high-frequency turbulence in fusion plasmas. *Frontiers of Physics*, 11:1–34.

[Dubin et al., 1983] Dubin, D. H. E., Krommes, J. A., Oberman, C., and Lee, W. W. (1983). Nonlinear gyrokinetic equations. *The Physics of Fluids*, 26(12):3524–3535.

[Einstein et al., 1915] Einstein, A. et al. (1915). Investigations on the theory of the brownian movement.

[Gary and Sanderson, 1979] Gary, S. P. and Sanderson, J. J. (1979). Electrostatic temperature gradient drift instabilities. *Physics of Fluids*, 22(8):1500.

[Ghahramany et al., 2011] Ghahramany, N., Gharaati, S., and Ghanaatian, M. (2011). New approach to nuclear binding energy in integrated nuclear model. *Physics of Particles and Nuclei Letters*, 8:97–106.

[Görler, 2010] Görler, T. (2010). *Multiscale effects in plasma microturbulence*. PhD thesis, Universität Ulm.

[Green, 1828] Green, G. (1828). *An Essay on the Application of mathematical Analysis to the theories of Electricity and Magnetism*. Nottingham.

[Hatzky et al., 2002] Hatzky, R., Tran, T. M., Könies, A., Kleiber, R., and Allfrey, S. J. (2002). Energy conservation in a nonlinear gyrokinetic particle-in-cell code for ion-temperature-gradient-driven modes in θ-pinch geometry. *Physics of Plasmas*, 9(3):898–912.

[Hazeltine and Waelbroeck, 2018] Hazeltine, R. D. and Waelbroeck, F. L. (2018). *The Framework of Plasma Physics*. CRC Press.

[Jenko, 2000] Jenko, F. (2000). Massively parallel vlasov simulation of electromagnetic drift-wave turbulence. *Computer physics communications*, 125(1-3):196–209.

[Kormann et al., 2019] Kormann, K., Reuter, K., and Rampp, M. (2019). A massively parallel semi-lagrangian solver for the six-dimensional vlasov–poisson equation. *The International Journal of High Performance Computing Applications*.

[Kotschenreuther et al., 1995] Kotschenreuther, M., Rewoldt, G., and Tang, W. (1995). Comparison of initial value and eigenvalue codes for kinetic toroidal plasma instabilities. *Computer Physics Communications*, 88(2):128–140.

[Kraus et al., 2016] Kraus, M., Kormann, K., Morrison, P. J., and Sonnendrücker, E. (2016). Gempic: Geometric electromagnetic particle-in-cell methods. cite arxiv:1609.03053Comment: 57 Pages.

[Krönig, 1856] Krönig, A. K. (1856). *Grundzüge einer theorie der gase*. AW Hayn.

[Landau, 1936] Landau, L. (1936). Kinetic equation for the case of coulomb interaction, phys. zs. *Sov. Union*, 10(154-164):24.

[Landau and Lifshitz, 1980] Landau, L. and Lifshitz, E. (1980). Statistical physics - Course of theoretical physics - Volume 5. *Publisher: Butterworth-Heinemann*, 3.

[Lawson, 1957] Lawson, J. D. (1957). Some criteria for a power producing thermonuclear reactor. *Proceedings of the physical society. Section B*, 70(1):6.

[Littlejohn, 1981] Littlejohn, R. G. (1981). Hamiltonian formulation of guiding center motion. *Physics of Fluids*, 24(9):1730.

[Mace, 2003] Mace, R. (2003). A gordeyev integral for electrostatic waves in a magnetized plasma with a kappa velocity distribution. *Physics of Plasmas*, 10(6):2181–2193.

[McLachlan and Quispel, 2002] McLachlan, R. I. and Quispel, G. R. W. (2002). Splitting methods. *Acta Numerica*, 11:341–434.

[Michels et al., 2022] Michels, D., Ulbl, P., Zholobenko, W., Body, T., Stegmeir, A., Eich, T., Griener, M., Conway, G. D., and Jenko, F. (2022). Full-f electromagnetic gyrokinetic turbulence simulations of the edge and scrape-off layer of asdex upgrade with gene-x. *Physics of Plasmas*, 29(3):032307.

[Miecnikowski et al., 2018] Miecnikowski, M. T., Sturdevant, B. J., Chen, Y., and Parker, S. E. (2018). Nonlinear saturation of the slab itg instability and zonal flow generation with fully kinetic ions. *Physics of Plasmas*, 25(5):055901.

[Mlynek et al., 2011] Mlynek, A., Reich, M., Giannone, L., Treutterer, W., Behler, K., Blank, H., Buhler, A., Cole, R., Eixenberger, H., Fischer, R., et al. (2011). Real-time feedback control of the plasma density profile on asdex upgrade. *Nuclear Fusion*, 51(4):043002.

[Noreen et al., 2019] Noreen, N., Riaz, F., Malik, S., and Zaheer, S. (2019). Ion bernstein mode instability with ring velocity distribution function. *Progress of Theoretical and Experimental Physics*, 2019(5).

[NRL, 2018] NRL (2018). Nrl plasma formulary. https://www.nrl.navy.mil/ppd/content/nrl-plasma-formulary.

[Ono et al., 1988] Ono, M., Beiersdorfer, P., Bell, R., Bernabei, S., Cavallo, A., Chmyga, A., Cohen, S., Colestock, P., Gammel, G., Greene, G., et al. (1988). Effects of high-power ion bernstein waves on a tokamak plasma. *Physical review letters*, 60(4):294.

[Oppenheim et al., 2001] Oppenheim, A. V., Buck, J. R., and Schafer, R. W. (2001). *Discrete-time signal processing. Vol. 2.* Upper Saddle River, NJ: Prentice Hall.

[Pitaevskii and Lifshitz, 1981] Pitaevskii, L. P. and Lifshitz, E. M. (1981). *Physical Kinetics: Volume 10 (Course of Theoretical Physics)*. Butterworth-Heinemann.

[Poppe and Wijers, 1990] Poppe, G. P. M. and Wijers, C. M. J. (1990). More efficient computation of the complex error function. *ACM Trans. Math. Softw.*, 16(1):38–46.

[Raeth et al., 2021] Raeth, M., Hallatschek, K., and Kormann, K. (2021). Full-6d kinetic simulations of magnetically confined plasmas. *DPG Spring Meeting*, Poster.

[Raeth et al., 2023] Raeth, M., Hallatschek, K., and Kormann, K. (2023). Slab itg simulated with 6d fully kinetic semi-lagrangian code. *Physics of Plasmas*, [Manuscript in preparation].

[Raeth et al., 2022] Raeth, M., Hallatschek, K., Kormann, K., and Schild, N. (2022). Excitation of high frequency waves in full-6d kinetic simulations of magnetically confined plasmas. *DPG Spring Meeting*, Presentation.

[Saha, 1921] Saha, M. N. (1921). On a physical theory of stellar spectra. *Proceedings of the Royal Society of London. Series A, Containing Papers of a Mathematical and Physical Character*, 99(697):135–153.

[Schild et al., 2023] Schild, N., Raeth, M., Eibl, S., Hallatschek, K., and Kormann, K. (2023). A performance portable implementation of the semi-lagrangian algorithm in six dimensions. *Computer Physics Communications*.

[Scott, 2006] Scott, B. D. (2006). Computation of turbulence in magnetically confined plasmas. *Plasma physics and controlled fusion*, 48(12B):B277.

[Sonnendrücker et al., 2004] Sonnendrücker, E., Filbet, F., Friedman, A., Oudet, E., and Vay, J.-L. (2004). Vlasov simulations of beams with a moving grid. *Computer Physics Communications*, 164(1–3):390–395.

[Sonnendrücker et al., 1999] Sonnendrücker, E., Roche, J., Bertrand, P., and Ghizzo, A. (1999). The semi-lagrangian method for the numerical resolution of the vlasov equation. *Journal of Computational Physics*, 149(2):201–220.

[Stroth, 2011] Stroth, U. (2011). *Plasmaphysik*. Springer.

[Sturdevant et al., 2017] Sturdevant, B. J., Chen, Y., and Parker, S. E. (2017). Low frequency fully kinetic simulation of the toroidal ion temperature gradient instability. *Physics of Plasmas*, 24(8):081207.

[Sturdevant et al., 2016] Sturdevant, B. J., Parker, S. E., Chen, Y., and Hause, B. B. (2016). An implicit delta f particle-in-cell method with sub-cycling and orbit averaging for lorentz ions. *Journal of Computational Physics*, 316:519–533.

[Sugama and Horton, 1998] Sugama, H. and Horton, W. (1998). Nonlinear electromagnetic gyrokinetic equation for plasmas with large mean flows. *Physics of Plasmas*, 5(7):2560–2573.

[Told et al., 2008] Told, D., Jenko, F., Xanthopoulos, P., Horton, L., Wolfrum, E., and Team, A. U. (2008). Gyrokinetic microinstabilities in asdex upgrade edge plasmas. *Physics of Plasmas*, 15(10):102306.

[Trott et al., 2022] Trott, C. R., Lebrun-Grandié, D., Arndt, D., Ciesko, J., Dang, V., Ellingwood, N., Gayatri, R., Harvey, E., Hollman, D. S., Ibanez, D., Liber, N., Madsen, J., Miles, J., Poliakoff, D., Powell, A., Rajamanickam, S., Simberg, M., Sunderland, D., Turcksin, B., and Wilke, J. (2022). Kokkos 3: Programming model extensions for the exascale era. *IEEE Transactions on Parallel and Distributed Systems*, 33(4):805–817.

[Wagner et al., 1982] Wagner, F., Becker, G., Behringer, K., Campbell, D., Eberhagen, A., Engelhardt, W., Fussmann, G., Gehre, O., Gernhardt, J., Gierke, G. v., Haas, G., Huang, M., Karger, F., Keilhacker, M., Klüber, O., Kornherr, M., Lackner, K., Lisitano, G., Lister, G. G., Mayer, H. M., Meisel, D., Müller, E. R., Murmann, H., Niedermeyer, H., Poschenrieder, W., Rapp, H., Röhr, H., Schneider, F., Siller, G., Speth, E., Stäbler, A., Steuer, K. H., Venus, G., Vollmer,

O., and Yü, Z. (1982). Regime of improved confinement and high beta in neutral-beam-heated divertor discharges of the asdex tokamak. *Physical Review Letters*, 49(19):1408–1412.

[Waring, 1779] Waring, E. (1779). Vii. problems concerning interpolations. *Philosophical transactions of the royal society of London*, (69):59–67.

[Wesson and Campbell, 2011] Wesson, J. and Campbell, D. J. (2011). *Tokamaks*, volume 149. Oxford university press.

[Wolfram Research, 2021] Wolfram Research, I. (2021). Mathematica, Version 13.2. Champaign, IL, 2022.

[Wolfrum et al., 2007] Wolfrum, E., Coster, D., Konz, C., Reich, M., Team, A. U., et al. (2007). Edge ion temperature gradients in h-mode discharges. In *34th EPS Conference on Plasma Physics*. European Physical Society.

[Yoon et al., 2014] Yoon, P. H., Hadi, F., and Qamar, A. (2014). Bernstein instability driven by thermal ring distribution. *Physics of Plasmas*, 21(7):074502.

[Zeiler et al., 1998] Zeiler, A., Biskamp, D., Drake, J., and Rogers, B. (1998). Transition from resistive ballooning to η i driven turbulence in tokamaks. *Physics of Plasmas*, 5(7):2654–2663.

Chapter 7

Acknowledgments

I would like to express my deepest gratitude to my advisor Klaus, for his patience, valuable guidance, and tremendous support throughout my PhD journey and before. His expertise and encouragement have been instrumental in shaping my research and ultimately this work. I am grateful for the countless hours he has spent reviewing my work and providing thoughtful feedback.

Furthermore, I would also like to extend my heartfelt thanks to Eric, the Head of the NMPP, for creating a dynamic and inclusive environment that fostered my growth and allowed me to explore various research areas. In addition, I extend my heartfelt thanks to all my colleagues at NMPP who have made my time here truly memorable. A special thanks goes to all my fellow PhD students, for the great companionship and all the after-work beers, even if they have not always been completely voluntary.

I am deeply grateful to everyone who has contributed to my thesis. I would like to extend a special thanks to Katharina, Nils, and Ali, who have been the strongest contributors to this work. Supporting me in the entire process from insight full discussions.

I wanted to take a moment to express my gratitude to Freddy for the opportunity to contribute to the MensaBot project. Working on this project has been an incredible experience and I have learned so much throughout the entire process. I want to thank you for believing in me and allowing me to be a part of this amazing team. The MensaBot project is without a doubt one of the most impactful software projects that I have ever had the opportunity to work on, and I am truly grateful for the chance to have contributed to it.

Here is a small excerpt from this exceptional work:

```
while true
   sleep(0.4)
   cl = driver.find_elements(by.By.CLASS_NAME, "rcx-message")
   sleep(0.4)

   if !isempty(cl[end].text)
      read_text!(MB, cl[end].text)
   else
      MB.answer = false
      MB.texts = []
   end

   check_poll(MB)

   check_game(MB)

   if MB.answer
      mess = driver.find_element(by.By.NAME, "msg")
      for text in MB.texts
         mess.send_keys(text)
         sleep(0.05)
         mess.send_keys(Keys.Keys.SHIFT, Keys.Keys.ENTER)
      end
      mess.send_keys(Keys.Keys.ENTER)

      MB.texts = []
   end
   sleep(0.1)
end
```

My sincere appreciation goes to the Schruns crew, who provided an extraordinary and encouraging setting for me to complete my thesis. I am deeply grateful for the delicious food and great company that you all provided throughout this final stage.

A huge thank you goes to all my friends in Munich how have to deal with me on a daily basis, Jakob, Jelena, Jonas, Lilya, Marko, Natalia, Rey, Rohan and many more, you are absolutely amazing. You are the main reason for my prevailing sanity. Thank you for all the distractions with drinks, discussion rounds, book clubs, boulder sessions, skiing and camping/kite trips, or the online board game night, throughout the rougher times of the last three years. One simply can not ask for more.

Y Martha, no puedo agradecerte lo suficiente por todo lo que has hecho por mí durante este último año. Tu amor, paciencia y comprensión han sido todo lo que

podría haber pedido. Gracias por entender las largas horas de estudio, las noches sin dormir y los momentos de estrés que he tenido que enfrentar. Tu presencia en mi vida me ha dado la fuerza y la motivación necesarias para seguir adelante. Te amo mucho!

Und das wichtigste zum Schluss. Mama, Papa, Ines vielen Dank für eure Unterstützung über all die Jahre. Ihr seid Inspiration, Freunde, Familie, Unterstützung in schweren Zeiten und so vieles mehr. Mehr kann man sich als Sohn/Bruder nicht wünschen.

Appendix A

Normalization

The quantities in this paper are normalized to typical scales. All lengths are given in units of the Larmor radius $\rho = \frac{\sqrt{mT}}{eB}$ and all velocity in units of the ion thermal velocity $v_{\mathrm{th}} = \sqrt{\frac{T}{m}}$. Thus, the time is given in units of the Larmor frequency $\omega_{\mathrm{c}} = \frac{v_{\mathrm{th}}}{\rho} = \frac{eB}{m}$. Furthermore, all densities are normalized to the background density n_0. In order to transform the equations with normalized quantities back, the following replacements are necessary

$$t \to \frac{1}{\omega_{\mathrm{c}}} t \tag{A.0.1}$$

$$\nabla \to \frac{1}{\rho} \nabla \tag{A.0.2}$$

$$\phi \to \frac{T}{e} \phi \tag{A.0.3}$$

$$n \to n_0 n \tag{A.0.4}$$

$$\boldsymbol{v} \to v_{\mathrm{th}} \boldsymbol{v} \tag{A.0.5}$$

Appendix B

Simulation Index

B.1 Explanation of simulation parameters

sim_params	
final_time	final simulation time
delta_t	time step
test_case	simulation setup
poisson_solve	selection of electrostatic potential solver
non_linear = .true.	
grid_dims	
num_cells_x1	number of grid points in x-direction
num_cells_x2	number of grid points in y-direction
num_cells_x3	number of grid points in z-direction
num_cells_x4	number of grid points in v_x-direction
num_cells_x5	number of grid points in v_y-direction
num_cells_x6	number of grid points in v_z-direction
domain_dims	
v_max	maximum velocity
x1_max	box length in x-direction
x2_max	box length in y-direction
x3_max	box length in z-direction
landau_params	
alpha	initial amplitude of perturbation
kx	wave vector, in case initial perturbation is plane wave

pslab_params	
kappa_ti	temperature gradient
C_Te	electron temperature
b0	background magnetic field strength
kappa_ni	density gradient

advect_params	
bc_type	boundary conditions
stencil	interpolation stencil with for velocity advection
interpolator_type	interpolation stencil type (centered or off-centered)
stencil_x	interpolation stencil width for spacial advection

B.2 Chapter 3

B.2.1 For dispersion relation and energy fluxes

```
sim_params
final_time = 20000
delta_t = 0.025
test_case = "delta"
poisson_solve = .false.
non_linear = .true.

grid_dims
num_cells_x1 = 128
num_cells_x2 = 128
num_cells_x3 = 8
num_cells_x4 = 32
num_cells_x5 = 32
num_cells_x6 = 32

domain_dims
v_max = 4.0
x1_max = 20.943951023931955
x2_max = 20.943951023931955
x3_max = 1507.964473723101

landau_params
alpha = 0.00000001
kx = 0.0 0.8 0.004166666666666667

pslab_params
kappa_ti = 0.05
C_Te = 1.0
b0 = 1.0

advect_params
bc_type = "sll_p_periodic"
stencil = 7
interpolator_type = "centered"
stencil_x = 8
```

B.2.2 For non-linear saturation

```
sim_params
final_time = 20000
delta_t = 0.05
test_case = "delta"
poisson_solve = .false.
non_linear = .true.

grid_dims
num_cells_x1 = 64
num_cells_x2 = 64
num_cells_x3 = 64
num_cells_x4 = 32
num_cells_x5 = 32
num_cells_x6 = 32

domain_dims
v_max = 4.0
x1_max = 20.943951023931955
x2_max = 20.943951023931955
x3_max = 753.9822368615505

landau_params
alpha = 0.0001
kx = 0.0 0.8 0.004166666666666667

pslab_params
kappa_ti = 0.1
C_Te = 1.0
b0 = 1.0

advect_params
bc_type = "sll_p_periodic"
stencil = 7
interpolator_type = "centered"
stencil_x = 8
```

B.3 Chapter 4

B.3.1 Dispersion relation of stable IBWs

```
sim_params
final_time = 8000
delta_t = 0.025
test_case = "delta"
poisson_solve = .false.
non_linear = .true.

grid_dims
num_cells_x1 = 128
num_cells_x2 = 8
num_cells_x3 = 8
num_cells_x4 = 32
num_cells_x5 = 32
num_cells_x6 = 32

domain_dims
v_max = 4.0
x1_max = 20.943951023931955
x2_max = 20.943951023931955
x3_max = 1507.964473723101

landau_params
alpha = 0.0001
kx = 0.0 0.8 0.004166666666666667

pslab_params
kappa_ti = 0.0
C_Te = 1.0
b0 = 1.0

advect_params
bc_type = "sll_p_periodic"
stencil = 7
interpolator_type = "centered"
stencil_x = 8
```

B.3.2 Cyclotron instability with linearised temperature gradient

```
sim_params
final_time = 4500
delta_t = 0.008
test_case = "delta"
ctest = .false.
non_linear = .false.

grid_dims
num_cells_x1 = 16
num_cells_x2 = 256
num_cells_x3 = 8
num_cells_x4 = 32
num_cells_x5 = 32
num_cells_x6 = 32

domain_dims
v_max = 4.0
x1_max = 3.141592653589793
x2_max = 12.566370614359172
x3_max = 251.3274122871834

landau_params
alpha = 0.0000001
kx = 0.0 0.8 0.004166666666666667

pslab_params
kappa_ti = 0.36
C_Te = 1.0
b0 = 1
gradient = 4
kappa_ni = 0.44

advect_params
bc_type = "sll_p_periodic"
stencil = 7
interpolator_type = "centered"
stencil_x = 8
```

B.3.3 Non-linear saturation of cyclotron instability

```
sim_params
final_time = 15000
delta_t = 0.03
test_case = "delta"
poisson_solve = .false.
non_linear = .true.

grid_dims
num_cells_x1 = 64
num_cells_x2 = 64
num_cells_x3 = 16
num_cells_x4 = 32
num_cells_x5 = 32
num_cells_x6 = 16

domain_dims
v_max = 4.0
x1_max = 12.566370614359172
x2_max = 12.566370614359172
x3_max = 251.3274122871834

landau_params
alpha = 0.00001
kx = 0.0 0.8 0.004166666666666667

pslab_params
kappa_ti = 0.36
C_Te = 1.0
b0 = 1
kappa_ni = 0.44

advect_params
bc_type = "sll_p_periodic"
stencil = 7
interpolator_type = "centered"
stencil_x = 8
```

B.4 Chapter 5

ITG with realistic temperature gradient

```
sim_params
final_time = 15000
delta_t = 0.02
test_case = "gradient"
poisson_solve = .false.
non_linear = .true.

grid_dims
num_cells_x1 = 128
num_cells_x2 = 32
num_cells_x3 = 16
num_cells_x4 = 32
num_cells_x5 = 32
num_cells_x6 = 16

domain_dims
v_max = 6.0
x1_max = 31.41592653589793
x2_max = 7.853981633974483
x3_max = 753.9822368615505

landau_params
alpha = 0.0000001
kx = 0.0 0.8 0.004166666666666667

pslab_params
kappa_ti = 0.5
C_Te = 1.0
b0 = 1
gradient = 2

advect_params
bc_type = "sll_p_periodic"
stencil = 7
interpolator_type = "centered"
stencil_x = 8
```

B.4.1 IBW with realistic temperature gradient

```
sim_params
final_time = 15000
delta_t = 0.008
test_case = "gradient"
poisson_solve = .false.
non_linear = .true.

grid_dims
num_cells_x1 = 64
num_cells_x2 = 32
num_cells_x3 = 16
num_cells_x4 = 32
num_cells_x5 = 32
num_cells_x6 = 16

domain_dims
v_max = 4.0
x1_max = 7.853981633974483
x2_max = 3.141592653589793
x3_max = 251.3274122871834

landau_params
alpha = 0.0000001
kx = 0.0 0.8 0.004166666666666667

pslab_params
kappa_ti = 0.36
C_Te = 1.0
b0 = 1
gradient = 2
kappa_ni = 0.44

advect_params
bc_type = "sll_p_periodic"
stencil = 7
interpolator_type = "centered"
stencil_x = 8
```